Modelling of MEMS vibratory gyroscopes utilizing phase detection

by

Antonie Christoffel Dreyer

Thesis presented in partial fulfilment of the requirements for the degree of Master of Science in Mechanical Engineering at the University of Stellenbosch

Department of Mechanical and Mechatronic Engineering,
University of Stellenbosch,
Private Bag X1, 7602 Matieland, South Africa

Supervisors:

Prof. Albert A. Groenwold
Dr. Philip W. Loveday

March 2008

Declaration

I, the undersigned, hereby declare that the work contained in this thesis is my own original work, except when due recognized, and that I have not previously in its entirety or in part submitted it at any university for a degree.

Signature: .....
A.C. Dreyer

Date: .....

Abstract

Modelling of MEMS vibratory gyroscopes utilizing phase detection

A.C. Dreyer

Department of Mechanical and Mechatronic Engineering,
University of Stellenbosch,
Private Bag X1, 7602 Matieland, South Africa

Thesis: MScEng (Mech)

March 2008

This thesis aims to contribute to the modelling and analysis of MEMS gyroscope technologies. Various gyroscope types are studied, and the phase-based vibratory gyroscope is then selected for further investigation.

In the literature, vibratory MEMS gyroscopes are mostly used in a single excitation and amplitude detection mode. However, a dual excitation and phase detection mode has recently been proposed, since phase-based detection, as opposed to amplitude-based detection modes, may be expected to increase measurement accuracy (in turn since improved signal-to-noise ratios may be expected). However, the presented analytical model was relatively crude, and the assumptions made appear unrealistic. Accordingly, in this thesis, an improved analytical model is developed.

To describe the dual excitation and phase detection problem more comprehensively, principles of classical dynamics are used herein to investigate the dual excitation of a two degree of freedom spring-mass-damper system subjected to an applied rotation rate. In doing so, an analytical formulation including mechanical coupling effects is extended into a generalized form, after which the amplitude and phase responses of the mechanically uncoupled system are interpreted. The differences between the amplitude and phase measurement techniques are illustrated.

Finally, the system is modelled numerically, and the scale factor of a hypothetical device based on the phase-based detection method is optimized, subject to constraints on the nonlinearity of the device, using constrained mathematical optimization techniques.

Uittreksel

Modellering van MEMS vibrerende giroskope wat van fase deteksie gebruik maak

("Modelling of MEMS vibratory gyroscopes utilizing phase detection")

A.C. Dreyer

Departement Meganiese en Megatroniese Ingenieurswese
Universiteit van Stellenbosch
Privaatsak X1, 7602 Matieland, Suid Afrika

Tesis: MScIng (Meg)

Maart 2008

Hierdie tesis poog om 'n bydrae te maak tot die modellering en analise van MEMS giroskoop tegnologieë. Verskeie tipes giroskope is bestudeer, waarvan die fase-gebaseerde vibrerende giroskoop gekies word vir verdere ondersoek.

In die literatuur word vibrerende MEMS giroskope meestal gebruik in 'n enkel opwekking en amplitude deteksie metode. 'n Dubelle opwekking en fase deteksie metode is onlangs voorgestel, aangesien daar verwag word dat fase-gebaseerde deteksie hoër akkuraatheid tot gevolg kan hê (as gevolg van 'n verbeterde sein tot geraas verhouding). Die huidige voorgestelde analitiese model is egter onvoldoende en van die aannames lyk onrealisties. Gevolglik is 'n verbeterde analitiese model in hierdie tesis ontwikkel.

Om die dubbele opwekking en fase deteksie probleem meer volledig te beskryf, is die teorie van klassieke dinamika gebruik om die effek van twee dimensionele opwekking van 'n tweevryheidsgraad veer-massa-demper stelsel onderhewig aan 'n toegepaste rotasiesnelheid te ondersoek. 'n Analitiese formulasie wat meganiese koppelling in ag neem is uitgebrei na 'n algemene vorm, waarna die meganies-ontkoppelde amplitude en fase responsie van die sisteem interpreteer word. Die verskille tussen die amplitude en fase metodes word daarna geïllustreer.

Ten slotte word die sisteem numeries gemodelleer en die skaalfaktor van 'n hipotetiese fase-gebaseerde giroskoop word ge-optimaliseer, in die teenwoordigheid van lineariteitsbeperkinge, deur van begrensde optimeringstegnieke gebruik te maak.

Acknowledgements

Firstly I would like to acknowledge our heavenly Father, the giver of every good and perfect gift. Secondly I want to thank my father for his encouragement in difficult times, as well as my mother and my two brothers, Wynand and Gustav, for their interest in my work. Thirdly I acknowledge all the people who helped contribute to my project; my study leaders Prof. Groenwold and Dr. Loveday, all the people I had discussions with, and Denel and the NRF for their funding.

Contents

List of Illustrations

Figures

Tables

Nomenclature

Variables

A	Substitution coefficient
a	Complex number constituent
a_x	Absolute acceleration in the x directions
a_y	Absolute acceleration in the y directions
B	Substitution coefficient
b	Complex number constituent
C	Substitution coefficient
c	Complex number constituent
c	Damping coefficient
c_i	Inertial coupling coefficient
c_d	Damping coupling coefficient
c_s	Stiffness coupling coefficient
c_j	Individual optimization constraint
D	Substitution coefficient
d	Complex number constituent
F	Force
f	Forcing ratio $\left(f = \frac{Y_s}{X_s}\right)$
j	Complex number operator
K	Constant number
k	Spring coefficient
l	Non-dimensional rotation velocity $\left(\frac{\Omega}{\omega_n}\right)$
lb	Optimization variable lower boundary
M	Magnitude

m	Proof mass
O	Origin
P	Periodic force
Q	Quality factor $\left(Q = \frac{1}{2\zeta}\right)$
r	Non-dimensional excitation frequency $\left(\frac{\omega}{\omega_n}\right)$
SF	Scale factor
s	Laplace variable
t	Time
ub	Optimization variable upper boundary
u_i	Non-dimensional inertial coupling coefficient
u_d	Non-dimensional damping coupling coefficient
u_s	Non-dimensional stiffness coupling coefficient
$X_I Y_I$	Inertial reference frame
X_s	Excitation force amplitude in x
Y_s	Excitation force amplitude in y
X	Complex phasor response solutions for x
Y	Complex phasor response solutions for y
xy	Local reference frame
x	Position relative to the local reference frame
x_{1-4}	State variables
y	Position relative to the local reference frame
β	Phase difference
Δ	Indication of difference
δ	Phase difference nonlinearity
γ	Substitution coefficient
κ	Complex number
Ω	Angular velocity
ω	Excitation frequency
ω_n	Natural frequency $\left(\omega_n = \sqrt{\frac{k}{m}}\right)$

ϕ	Phase angle for x response
θ	Phase angle
φ	Phase angle for y response
ϑ	Optimization variables
ξ	Substitution coefficient
ζ	Damping ratio $\left(\zeta = \frac{c}{2\sqrt{km}}\right)$

Vectors and Tensors

$\vec{a}$	Acceleration vector
$\vec{F}$	Force vector
$\vec{\mathrm{lb}}$	Optimization variable lower boundary vector
$\vec{\Omega}$	Angular velocity vector
$\vec{r}$	Position vector
$\vec{u}$	State matrices and vectors
$\vec{\mathrm{ub}}$	Optimization variable upper boundary vector
$\vec{v}$	Velocity vector
$\vec{\mathrm{x}}$	State variable vector
$\vec{\mathrm{y}}$	State output vector

Subscripts

0	Initial value
A	Particle representing proof mass
A/B	A relative to B
B	Origin of local reference frame xy
I	Inertial
min	Minimum
max	Maximum
n	Natural frequency subscript
x	x direction
1	x direction (in context)

y	y direction
2	y direction (in context)

Chapter

1

Introduction

1.1 Motivation

The first thing that comes to mind when hearing the word “gyroscope”, is usually the concept of some kind of spinning mass. However, gyroscopes have come a long way since the spinning wheel and the study of gyroscopes has been transformed into a complete multi-disciplinary field [1], involving classical mechanics [2], fluid dynamics [3], optics [4], electronics [5] and even quantum physics [6]. The wide range of gyroscope developments can be attributed to the staggering amount of applications where rotational measurement is needed. The need for smaller and lighter gyroscopes has also partly been met by Micro-Electro-Mechanical-Systems (MEMS).

With the advent of micro-machining technology, microsystems and MEMS, a whole new world of possibilities for devices has indeed been opened for exploration. Many sensor and transducer needs can be addressed by MEMS devices and include sub-millimeter sensors for measuring temperature, fluid flow, pressure, gas concentrations, acceleration and of course, rotation rate. Much development is done in the MEMS transducer field and the literature is filled with examples of novel micro-machined gyroscopes that are constantly improved, with good reason. The number of market opportunities are immense, be it through technology push or market pull [7]. The opportunities in the market range from all types of different applications, each having their own need in accuracy, reliability and cost. Various MEMS gyroscope concepts have been reported [8], some to reduce costs [9], and others to increase performance [10; 11; 12; 13; 14; 15; 16; 17]. There is a great need to develop smaller and more accurate inertial navigation systems [18], making many high performance gyroscopes bound to be used in inertial navigation and inertial measurement units (IMU’s) [18].

1.1.1 Inertial navigation

Guidance and navigation has been the main application of early mechanical gyroscopes and north-seeking gyroscopic compasses, since magnetic compasses could not be used in metal hulled ships and visual navigation (i.e. the stars) was not always possible. Gyroscopes are used in inertial navigation systems for very much the same reasons today.

Usually, navigation is done with some contact to a fixed reference frame, but it is not always possible or desired. Inertial navigation is a method of navigating by measuring movement in inertial space, rather than with respect to a visible or tangible reference frame. An object's change of position and rotation is measured in all three directions and if the starting position is known, the object's absolute position and attitude can be calculated [19]. More specifically: *the position of the object in the inertial reference frame will be coupled to a tangible reference frame through specifying a reference starting position and measuring compounded changes thereof* [1].

Direct displacement measurement is generally not possible in inertial space, so acceleration is often measured and integrated twice with respect to time to determine displacement. Rotation on the other hand, can be determined by either measuring angular acceleration and integrating it twice, measuring angular velocity and integrating it once, or directly measuring angular displacement. The result is that IMU's usually have three accelerometers and three gyroscopes to measure movement in all six degrees of freedom.

When using an inertial navigation system (INS), the error of true position will be compounded as time progresses, especially because measurement errors are integrated. It will be necessary to correct the resulting error (or drift) using some correction system. Therefore, modern navigation systems usually use a combination of a Global Positioning System (GPS) together with an INS for increased accuracy and reliability. When the INS is accurate enough, no GPS correction is necessary. The result is that the development of high performance inertial measuring devices is a high priority, especially for military applications.

1.1.2 Military applications

In military applications, autonomous weapon systems which are not prone to outside interference are of great importance [20]. It is ideal to use an inertial navigation system without GPS correction in missiles, unmanned arial vehicles (UAV's) and guided munitions, since devices with autonomous control cannot be jammed. Size and weight are large factors inhibiting performance and large gyroscopes are not ideal, making MEMS IMU's the logical answer for military navigation uses. However, the high need for accuracy in IMU's puts a very high demand on its specifications. MEMS gyroscope designers are striving to develop

gyros with adequate performance [18]. Noise is typically the limiting factor in the small MEMS devices [21].

Not all military applications require the high drift stability of an INS. Some require rapid reaction and high-G capability [22], such as self-guided kinetic energy weapons, gun-launched missile systems [23] and counterforce weapons. Low and medium performance military applications include smart munitions, aircraft and missile autopilots, short time-of-flight tactical missile guidance, fire control systems, radar antenna motion compensation and multiple intelligent small projectiles such as flechettes or even inertial guided "bullets" [24].

1.1.3 Commercial applications

Commercial applications of inertial sensors include hand-held video camera image stabilization, bio-medical motion measurement, toys and games, virtual reality devices, robotics and automation, borehole and oil well drilling, surveying underground pipelines, hand-held navigation equipment and aircraft attitude and flight path control [25]. The automotive industry is probably one of the largest users of MEMS gyroscopes and is growing constantly with the increased safety-consciousness of vehicle manufacturers [25]. The implementations are in airbags, rollover detection, anti-skid systems and navigation when GPS signals are lost [26]. Gyroscopes used in these applications range from extremely cheap and inaccurate MEMS devices to expensive and precise optical gyroscopes, depending on their use.

1.2 Aim and overview

The aim of this thesis is to improve on existing MEMS gyroscope technologies, especially in the drive to use MEMS gyroscopes in military IMU's. In order to try to improve on the existing gyroscope technologies, a broad overview of existing devices is needed. Chapter 2 consists of a literature review regarding existing gyroscope technologies, and attractive concepts for improvement are investigated. Regular macroscopic gyroscopes, as well as MEMS gyroscopes are discussed. The phase based vibratory gyroscope concept is then chosen for further analysis.

Chapter 3 presents the analytical formulation of the steady state dynamics of a vibratory gyroscope from first principles. It is shown how traditional amplitude based gyroscopes operate, whereafter the phase-based operation method is introduced and investigated.

Chapter 4 presents a concise verification of the developed analytical model by the state space and time dependent methods. An infrastructure is developed for future time-variant analyses.

Chapter 5 is concerned with optimization of a vibratory gyroscope in the phase based operation method.

Conclusions and recommendations for future work are presented in Chapter 6.

The appendices contain additional information and the source code that was used.

Chapter

2

Current Gyroscope Technology

"Ab actu ad posse valet illatio"
-From the past one can infer the future.

Many researchers and engineers have tried to implement macro-gyroscope concepts in MEMS, some more successful than others. To know what the future possibilities of MEMS gyroscopes are, it is useful to firstly examine where they came from. In this chapter the existing gyroscope technology is presented by looking at the various different types of gyroscopes and miniaturization of the existing gyroscope concepts are explored.

2.1 Gyroscope classification

The wide range of gyroscope types and applications require categorization into different classes. The classification can be made in many ways, namely cost, physics or materials utilized and performance specifications. It is worthwhile to start off with the definition of the main gyroscope performance specifications and the different types corresponding to those ranges.

The most popular classification specification is the bias stability or drift, which is the measurement of gyroscope accuracy over time. The bias stability is the amount of error introduced to the measurement independent of inertial effects, and can be measured when the sensor is static [24]. A simple example would be putting the device on a table and walking away. The amount of rotation it has measured after an hour, is the bias stability in $^\circ$/h. Low bias drift is especially important for inertial navigation and is usually specified with the electronic circuitry included. It may be troublesome to design for a specification like bias drift in one iteration of the design process, especially in MEMS gyroscopes, because the bias drift is dependent on the amount of noise introduced by changes in the properties of structures or electronics due to temperature or ageing.

Figure 2.1 shows the performance ranges of different types of gyroscopes that are currently in use, by mapping the scale factor and bias stability ranges for the main types of gyroscopes. The traditional mechanical gyroscopes are seen to have the highest bias stability performance (i.e. the lowest drift), followed by optical and silicon micro mechanical (MEMS) gyroscopes.

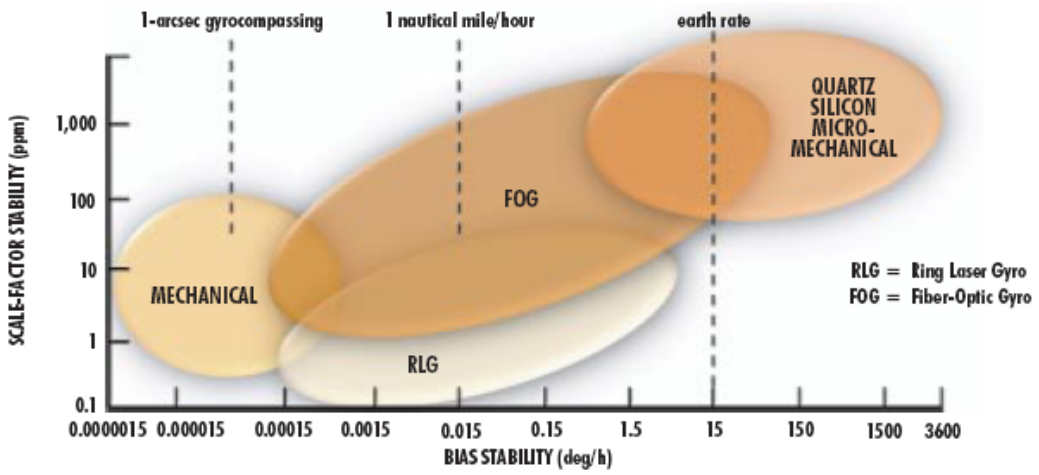

Figure 2.1. Classification of gyroscopes [18]

The scale factor stability is the overall ability of the scale factor of the sensor to maintain accuracy as a function of angular rate, or how well the sensor reproduces the sensed rotation rate [18]. The scale factor error is therefore the deviation of the measured rotation rate from the true rotation rate and is normally given as a percentage at the full scale [21].

The scale factor and bias stability are only two gyroscope specifications, the other main specifications being the following [27; 28]:

- Angle random walk [$^\circ/\sqrt{\text{h}}$] : Noise-manifested non-deterministic behaviour
- Bias stability (drift) [$^\circ$/s,$^\circ$/h]: Error independent of inertial effects
- Scale factor accuracy [%]: Variation of output signal per unit change of input quantity
- Maximum allowable shock [g's]: Robustness and shock resistance
- Full-scale range [$^\circ$/s]: Sensor measurable range
- Bandwidth [Hz]: Sensor useful frequency range
- Sensitivity [V/($^\circ$/s)]: Minimum measurable quantity
- Resolution [deg/s]: Minimum increment of measurement that can be made

Parameter	Rate Grade	Tactical Grade	Inertial Grade
Angle random walk [°/$\sqrt{\text{h}}$]	> 0.5	$0.5 - 0.05$	< 0.001
Bias drift [°/h]	$10 - 1000$	$0.1 - 10$	< 0.01
Scale factor accuracy [%]	$0.1 - 1$	$0.01 - 0.1$	< 0.001
Full-scale range [°/sec]	$50 - 1000$	> 500	> 400
Maximum allowable shock [g's]	10^3	$10^3 - 10^4$	10^3
Bandwidth [Hz]	> 70	~ 100	~ 100

Table 2.1. Main Classes of gyroscopes [28]

The above-mentioned errors are typically temperature dependant and different types of errors are more dominant in different types of gyroscopes. Using these specifications, gyroscopes are divided into three main classes, namely Rate-grade, Tactical-grade and Inertial grade. The performance requirements for the three classes are shown in Table 2.1. With the main gyroscope performance classes and specification ranges specified, the existing gyroscope technologies are now explored.

2.2 Gyroscope technology

2.2.1 Gyroscope origins

Inertial rotation measurement and the birth of the term "gyroscope" can be traced back to Léon Foucault, designer of the Foucault Pendulum. The Foucault Pendulum was first publicly displayed in 1851 to illustrate the earth's rotation. A machine invented in 1817 by Johann Bohnenberger [29] led Foucault to the invention of the spinning wheel gyroscope in 1852. After the invention of the electric motor in the late 1800's, the first commercial gyroscope prototypes were built and started to be used in various applications [1]. Mechanical gyroscopes have successfully been used as rotation meters ever since, and the term "gyroscope" is now synonymous with devices that measure rotation or rotation rate.

2.2.2 Mechanical spinning wheel gyroscopes

The conventional modern spinning wheel gyroscope is the direct descendant of Bohnenberger's machine and Foucault's early gyroscope. The spinning wheel gyroscope can be recognized as a spinning disc mounted within a gimbal system that allows it to move freely with respect to the gimbal structure mounting points. Due to the conservation of angular momentum, the axis of the rotating mass stays fixed in inertial space and acts as a portable attitude and heading reference direction. In the absence of friction and imbalances the spinning disc will keep it's direction indefinitely, although this is not the case with real devices [30].

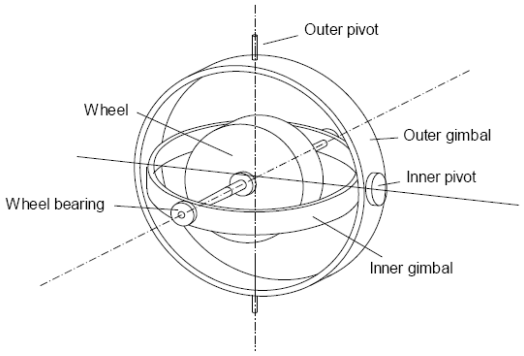

Figure 2.2. Mechanical gimballed gyroscope [29]

Other factors like the constraints of measuring mechanisms and gimbal lock[1] mean that it is not always possible to use the spinning wheel's stationary direction in inertial space to determine rotation. The conservation of angular momentum is still a very useful mechanism of controlling and measuring rotation mechanically. The concept has been improved on by using variations on the basic concept, mostly using the physical effect of gyroscopic precession.

When a spinning wheel is tilted, the gyroscopic effect (or precession) causes motion orthogonal to the sense of the tilt direction. Springs are added to the supporting gimbal structure as in Figure 2.3, and the induced torque is proportional to the applied tilt. The spring tension is then measured and used to obtain the desired angle of rotation. However, the springs limit the gyroscope performance and subsequent gyroscopes, like the rate integrating gyroscope, have been developed to overcome the problem. The rate integrating gyroscope uses a single degree of freedom restraining torque to keep the gyro gimbal at null, eliminating gimbal problems [24]. Other spinning mass gyroscope designs work mostly on similar principles and include the dynamically tuned gyroscope, flex gyroscope, gas bearing and electrostatically suspended spherical gyroscope [1].

The required high spinning speed of the round mass in all the above mentioned devices has several disadvantages, including the necessity of precision machining, long startup times and high cost. However, the spinning mass gyroscope is still one of the highest performing gyroscopes (see Fig. 2.1).

Due to the three-dimensional nature of mechanical gyroscopes, it is extremely difficult to miniaturize the concept to the scale of MEMS. Miniaturization of the spinning wheel is not only impaired by the two-dimensional batch fabricated nature of MEMS devices, but also silicon's bad friction characteristics. Only one case of a spinning wheel MEMS gyroscope has been reported, where a spinning wheel was electrostatically suspended in a MEMS device to measure rotation [32].

[1] Gimbal lock is when gimbals align to remove a degree of freedom from the system.

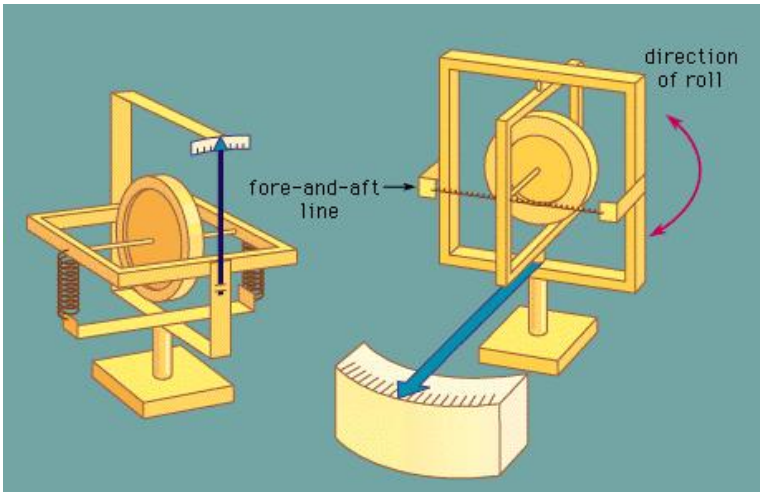

Figure 2.3. Measuring gyroscopic precession [31]

2.2.3 Optical gyroscopes

Optical gyroscopes are well known for their high accuracy and originated in the early 60's when it was demonstrated that rotation velocity can be measured by a change in the path lengths of two counter-propagating beams of light. The optical gyroscope is a well-developed technology and has steadily replaced mechanical gyroscopes as the preferred method to accurately measure rotation since the late 1980's [24]. Optical gyroscopes have since been used in inertial navigation units (INU's) and are widely used in military and civilian aircraft. Two main type of optical gyroscopes are in use, namely the ring-laser gyroscope (RLG) and the fiber-optical gyroscope (FOG).

Ring-laser gyroscope (RLG): The RLG uses the phase shift between two counter-propagating laser beams that are configured in a closed shape (usually a triangle) to measure angular rotation. A laser beam is split into a clockwise and counter-clockwise direction with mirrors to guide the beams. A standing wave pattern is formed (referred to as resonance) and when the device rotates, one of the laser beams travel a further distance than the other. The different path length then generates a phase shift between the two laser beams, which is called the Sagnac effect.

The output of a RLG is the beat frequency of the laser lines circulating in opposite directions, requiring relatively simple electronic signal processing [34]. The laser has to have a high spectral purity and a stable light source, such as a HeNe laser. There are a few variations on the basic concept and a frequency lock-in effect can occur at small rotation rates creating a null-shift, but solutions to the problem have been developed [35].

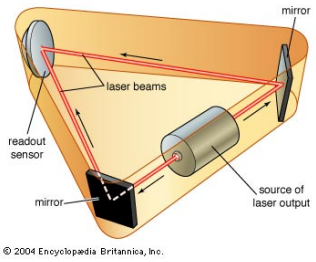

Figure 2.4. Ring laser gyroscope [33]

Fiber-optical gyroscopes (FOG): Fiber-optical gyroscopes also use the Sagnac effect, but with optical fibres as the propagation medium. The main reason for the development of the FOG is to increase the signal generated by the phase shift, by increasing the length of the light beam without making the device any larger. FOG's do not necessarily perform as well as RLG's and demand relatively complicated optical and electronic signal processing to retrieve the phase shift [34], but are still relatively high-performance devices. Furthermore, it is lightweight, relatively small, has limited power consumption, a long projected lifetime and last but not least, has a cheaper price [4]. Different types of fiber-optic gyroscopes exist, namely the interferometric fiber-optical gyroscope (IFOG), the resonant fiber-optical gyroscope (RFOG) and the fiber ring laser gyroscope (FRLG)

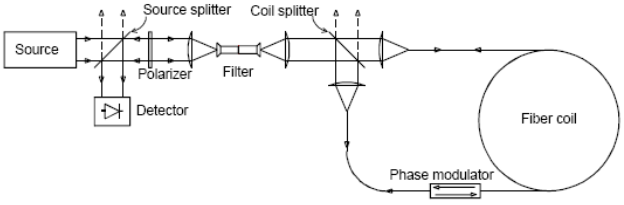

Figure 2.5. Fiber-optical gyroscope [36]

2.2.4 Fluidic gyroscopes

Fluidic gyroscopes can be defined as devices that use fluid interaction to measure angular motion[2]. Although much effort has been made in the development of fluidic gyroscopes, fluid-based gyroscopes have not been implemented as widely as the mechanical and optical types. Fluidic gyroscopes have not yet proved to be suitable for inertial navigation, but are rugged and can be used for stabilisation. The difficulty in achieving adequate stability and resolution in some of these devices is attributed to the influence of temperature changes on fluid properties [1].

[2]In this context, the term "fluidic gyroscope" should not be confused with mechanical gyroscopes which use fluid or gas to suspend a spinning mass, which may sometimes also be referred to by the same term.

Using fluid inertia is probably the most obvious way to measure angular motion with fluids, and three main fluidic devices have been reported in the literature.

Flueric gyroscope: The Flueric gyroscope uses a spherical cavity with a rotating mass or swirl of gas within the cavity. When a rotation is applied to the sensor, the direction of the swirl of gas remains fixed in inertial space due to the inertia of the fluid, and the applied rotation can be detected by monitoring pressure changes inside the cavity using porous cavity walls [1].

Dual-axis rate transducer (DART): The DART is similar to the Flueric gyroscope, but uses paddles inside a mercury filled spinning cavity to measure changes in the movement of the mercury when an external angular velocity is applied.

Magneto-hydrodynamic gyroscope: Another fluid-based device is the Magneto-hydrodynamic angular motion sensor and torque generator [3]. It uses an electromagnetic field applied over a conductive fluid (eg. mercury), which generates electric current when an external rotation is applied. The combination of inertia, the applied magnetic field and conductivity of the fluid then generates electric current due to Faraday's law. The induced electric current can be measured to determine rotation. When an electric current is applied instead of being measured, this type of configuration can also be used to generate torque.

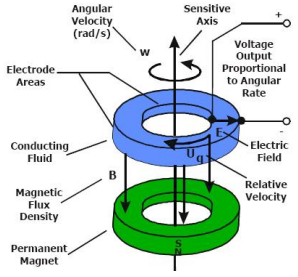

Figure 2.6. Magneto-hydrodynamic sensor [3]

Due to the three-dimensional nature of the fluidic gyroscopes, it will be difficult to miniaturize these devices.

2.2.5 Vibratory gyroscopes

2.2.5.1 The Coriolis effect

Vibratory gyroscopes use vibrations of structures together with the Coriolis effect to measure angular motion in one form or another [11; 37]. The Coriolis effect

was named after Gaspard-Gustave Coriolis who, in 1835, described an acceleration that appears when a body is moving inside a rotating coordinate frame [27]. The Coriolis effect is responsible for many physical phenomena, including the sidewards deflection of artillery projectiles, wind directions and ocean currents, due to the rotation of the earth. The simplest way to illustrate the Coriolis effect is by the sidewards deflection of a particle moving with a certain velocity across the surface of a spinning disc, as depicted in Figure 2.7. When the particle is moving with a linear velocity, it gets deflected to the side. However, when it is vibrated in one direction, a secondary vibration is induced due to the Coriolis effect.

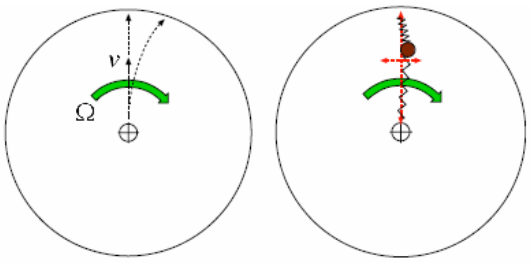

Figure 2.7. Visual explanation of the Coriolis effect [31]

The Coriolis acceleration of a point is mathematically defined as the cross product between the angular velocity of a local reference frame and the linear velocity relative to that frame, and is defined as

$$\bar{a}_c = 2\bar{\omega} \times \bar{v}_{rel}, \tag{2.2.1}$$

where $\bar{\omega}$ and $\bar{v}_{rel}$ are the angular and linear velocities respectively. When the vectors $\bar{\omega}$ and $\bar{v}_{rel}$ are orthogonal to each other, the cross product operator causes the Coriolis acceleration to be orthogonal to both the other terms, with the right-hand rule giving the sense of the acceleration. In vibrating element gyroscopes, the linear velocity of the mass is obtained by an excited vibration, similar to that of Figure 2.7. There are two main types of vibratory gyroscopes found in the literature, namely those that measure angular displacement, and those that measure angular velocity [11].

2.2.5.2 Angular displacement vibratory gyroscopes

Angular displacement gyroscopes are characterized as sensors that are used to measure rotation angles directly. These type of gyroscopes mostly use the same principle of operation as the Foucault pendulum, wherein a mass is periodically actuated in a fixed direction in inertial space. To an observer on a rotating local reference frame, there is a precession of the line of vibration, making it possible to measure angle of rotation directly. The amount of precession observed may depend on the parameters of the system.

The measurement of angular displacement instead of angular velocity eliminates the need for integrating the signal, which is why angular displacement gyroscopes are sometimes referred to as rate integrating gyroscopes [38]. Angular displacement measurement in vibratory devices can be done using vibrating strings, bars, rings, cylinders and hemispheres [37]. Although rings, cylinders and hemispheres are loosely based on the same principle of precession of a vibrating mass, the implementation differs.

Since circular vibratory structures do not vibrate in a line, the relevant circular object is used as a medium on which a standing wave pattern is excited. If a rotation is applied, the excited vibration undergoes a precession in the local coordinate frame. The line of precession is then used to measure the applied rotation (Fig. 2.8). The hemispherical resonating gyroscope (HRG) is of most interest as a macro angular displacement vibratory gyroscope.

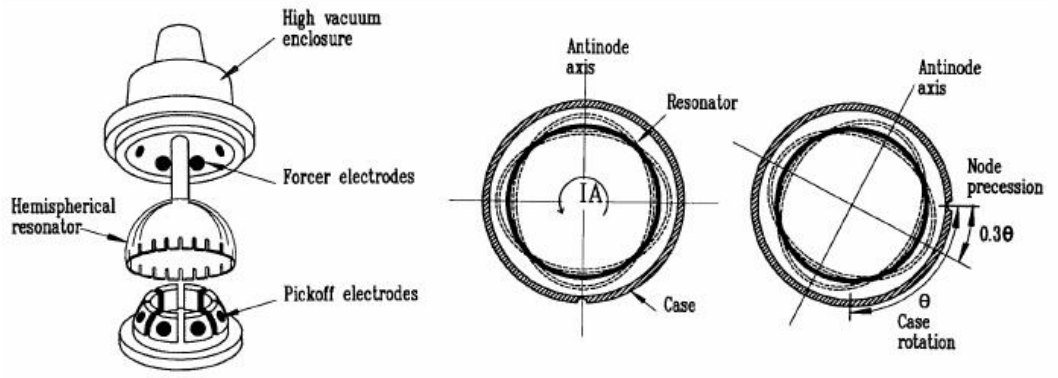

Figure 2.8. Hemispherical Resonator Gyroscope [27]

Hemispherical resonator gyroscope: The HRG, or "wine glass" gyroscope, consists of a hemispherical shell with an electrostatically excited and capacitively sensed vibration. The excitation is controlled by a system which has to compensate for damping and asymmetries in the structure without interfering with the precession of the wave [11], making a good understanding of control theory an important part of the development of this concept.

The HRG is regarded as a very high performance device that can be used for inertial navigation and has even been used in the Cassini spacecraft sent to observe the planet Jupiter [39]. The accuracy of the device is size-dependant and decreasing the size of the sensor will generally decrease its accuracy. A thimble-sized HRG can perform in the 1°/h range [24].

Two main drawbacks of the HRG are the large influence of material imperfections and the difficulty of manufacturing a perfectly axi-symmetric hemisphere.

These factors invariably reduce the sensor performance and can only be minimized with some difficulty and large costs. Subsequently HRG's are very expensive. Unfortunately there is little detail information available on the HRG, probably due to to military secrecy [40], since this device has been listed as a military critical technology due to it's high performance [41].

Take note that the hemisphere is a complicated structure that is not micromachinable with current micro-machining technology, especially not to the accuracy needed. This has resulted in the further development of other configurations like vibrating cylinders and vibrating rings, which may be possible to implement on a MEMS scale when using high aspect-ratio micro manufacturing techniques like lithography electroplating and molding, more commonly known as LIGA [42].

Vibrating rings have also been used to take advantage of the accuracy of the concept and have been implemented with success by companies like BAE systems in their vibrating structure gyroscope (VSG) [22]. Much research has also been done on implementing direct angular measurement in MEMS by a research group in California[3]. Vibratory devices that use the Coriolis effect to measure angular rate and not angular displacement directly, are now discussed.

2.2.5.3 Angular velocity gyroscopes

Angular velocity, or rotation rate gyroscopes, are sensors that measure angular velocity due to the Coriolis effect on a constrained vibrating mass[4]. If the vibrating mass is constrained, there is transfer of energy between the main axes of vibration in the local coordinate frame. Typically, a vibration is excited in a primary axis and with an applied rotation rate, Coriolis vibrations are induced in a secondary orthogonal direction. The amplitude of the secondary Coriolis vibration can then be measured to give an indication of angular velocity. The most popular device of this type is the tuning fork gyroscope.

Tuning fork gyroscope: The tuning fork gyroscope is a very popular concept for a vibrating-element angular rate sensor. Various types of configurations exist, but all work on the same principle of balanced induced Coriolis forces. In order to compensate for linear velocities and accelerations, two symmetric vibrating elements are used in a tuning-fork configuration. The vibrating elements, called tines, are vibrated in phase towards each other. With the application of a rotation rate, a secondary lateral vibration is induced in both tines, as shown in Figure 2.9. The secondary vibration is then sensed by either measuring it directly, typically with piezo-electric elements, or the vibration is transferred to the base of the tuning fork and measured as a periodic torque. The vibration can also be

[3] Mechanical and Aerospace Engineering at the University of California - Irvine.

[4] The terms "rotation rate" and "angular velocity" are used interchangeably throughout this thesis.

transferred to a secondary tuning fork that is only used for sensing. The tuning fork gyroscope has been reported to be very resistant to noise [43].

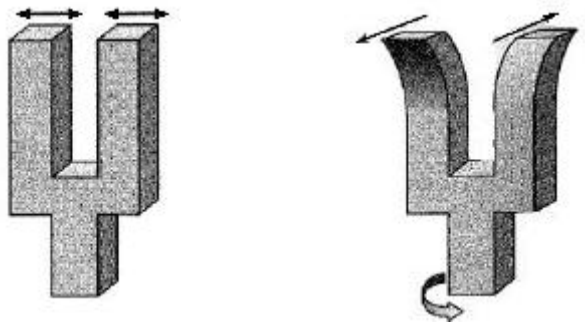

(a) Tine oscillation

(b) Coriolis acceleration

Figure 2.9. The Coriolis effect on a tuning fork [31]

Quapason: The Quapason is a sensor very similar to the tuning fork gyroscope, but instead of having two vibrating tines, it has four that are located on a common base, facing in the same direction. Ceramic piezoelectric elements are used to excite vibrations in the primary mode and detect vibrations in the secondary mode. It is a low-cost robust and reliable device developed by the French company SAGEM, with a performance in the range of 100°/h [44].

Other vibratory gyroscopes: Quite a few other solid-state vibratory gyroscopes that also use induced Coriolis vibrations have been reported, including vibrating beams [45], tubes [46], plates [47] and shear modes of various types [48]. Most of them are piezo-electrically based, are usually susceptible to external noise and not suited for high-performance devices. Piezo-electric surface acoustic wave (SAW) gyroscopes have also been reported [49; 50; 51], but are also not suited for high performance applications [52].

2.2.6 Non-vibratory MEMS gyroscopes

2.2.6.1 Micro-optical gyroscopes

Optical gyroscopes have little or no moving parts, making them an attractive concept to satisfy the need for small, robust and high performance solid state devices [53]. It would especially be advantageous to develop relatively cheap micro-optical gyroscopes. However, the main problem with miniaturizing a ring laser concept is the inherent reduction in the path length [54]. Typical path lengths for accurate optical gyroscopes are about 300mm for a gyroscope with a bias drift of

about 0.001°/h and a path length of 50mm corresponds to about 5°/h [1]. To be able to measure rotation rate accurately enough, micro-optical gyroscopes have to overcome this problem.

A single report of a Micro-Opto-Electro-Mechanical (MOEM) gyroscope which uses a novel way to increase the path length has been reported [55] and is depicted in Figure 2.10, but its feasibility as a highly accurate sensor can be debated. Other MOEM gyroscopes have also been reported, namely using planar waveguides and photonic crystals.

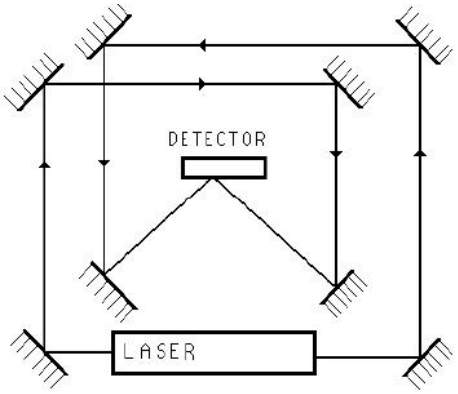

Figure 2.10. Increased Path Length concept [55]

Resonant micro optic gyroscope (RMOG): By etching high quality channels in silicon wafers, it is possible to make a waveguide that guides electromagnetic waves similar to a fibre-optic cable. Using low-loss channels, surface waveguided micro-optical devices on a silicon chip may be feasible [18]. Developments in telecommunications and optical computing are driving the performance of micro-optical components that are needed in an RMOG. Several institutions have been working on the RMOG concept [56] and a 1°/h RMOG with a 20mm diameter cavity has been reported [53].

Photonic crystals: Photonic crystals are nano-structures that contain a set of microcavities which affect the movement of photons through the media in a similar way that semiconductors are a media for electrons to travel through. A new manifestation of the Sagnac effect has been reported on this small scale by studying the crystals under rotation [57]. It was reported that it is possible to design compact gyroscopes using this method.

Both of these concepts are material science and manufacturing process intensive, which limits its exploration as a MEMS gyroscope. However, either one of them may be the future solution of the requirement of small high-performance devices [58].

2.2.6.2 Micro-fluidic gyroscopes

Limited research on micro-fluidic gyroscopes have been reported in the literature, most likely because it can be considered very difficult or impossible to implement inertial sensing of fluid motion in a MEMS device. Micro-fluidic channels are governed by low Reynolds numbers due to their small size and inertial effects are negligible compared to viscous and cohesion forces in such a small environment [59]. Another mechanism is therefore relied on to measure rotation in MEMS fluidic gyroscopes, namely the gas jet.

Gas jet gyroscope: A fluid-based sensor that seems quite feasible as a MEMS device, is the gas jet or gas stream gyroscope. It uses a laminar stream of gas, usually air, forced past heated wire elements at the opposite sides of a flow channel. When rotation takes place, the stream curves and creates a differential change in the cooling of the wires, as depicted in Figure 2.11. The differential change in wire electrical resistance is then used to measure the deflection of airflow[5], and the applied angular velocity can be calculated by using the Coriolis acceleration of the gas jet. Development of single and dual-axis gyroscopes using this concept have been reported [60; 61; 62; 63].

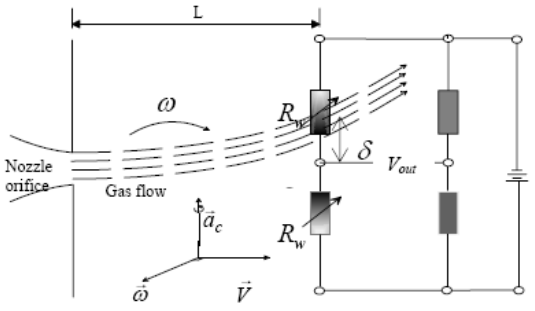

Figure 2.11. Gas stream gyroscope [60]

A big advantage of the gas stream gyroscope is that it can be easily manufactured [62]. When developing a single-axis gyroscope, only four layers of silicon deposition and photo-masking are needed in the microfabrication process. The simplicity of the gyroscope design is partly because it uses a piezoelectric vibrating disc with ejection jets for pumping. It should also have high shock-resistance, since it has no complicated moving structures. Performance of the sensor seems to be quite high, although no bias drift specification is available. The operating bandwith possibilities of this new class of device is also unsure and should be experimentally determined, but it may be insufficient for many applications [63].

[5]The measurement of airflow using a hot-wire has seen widespread success and hot wire anemometry and it is a well-established science.

The expected sensitivity to temperature and other environmental effects need to be reduced in packaging, possibly making enclosures larger than regular MEMS vibrating gyros necessary. It is also necessary to compensate for the sensor temperature sensitivity, but this is the case in most MEMS devices. There is no mention in the literature of commercially available gas jet gyroscopes, although it may only be due to the recentness of development, or the general difficulty of commercializing a MEMS concept [26].

A difficulty that should be considered when investigating micro-fluidic devices containing gas flow is that regular fluid dynamics do not necessarily apply to them. In very small channels the gas cannot be assumed to be a continuum and the regular Navier-Stokes equations begin to break down. The reason is that the molecule mean free path is significant compared to the characteristic dimension of the channel where flow occurs [64]. Therefore it may be necessary to use rarefied gas theory which complicates the design process significantly, especially if no high-end MEMS numerical software packages that simulate these effects are available.

Considering all the above-mentioned aspects, it may be possible that the gas stream gyroscope could possibly fit only a few specific applications, but it may be useful to explore this device in the future.

2.2.7 Vibratory MEMS gyroscopes

Piezoelectric and solid state gyroscopes have mostly started out as macroscopic devices, but have been miniaturized over time, since there is a conceptual compatibility of using a vibrating element to measure rotation rate in a MEMS device. The vibrating structure concept has been applied with great success as a MEMS gyroscope [8; 28]. This has been mainly due the relative ease and low cost of implementing a vibrating mass on 2-dimensional surface with silicon micromachining technology. The majority of MEMS gyroscopes are of the vibrating structure type and MEMS vibratory gyroscopes is classified as a type on its own.

2.2.7.1 Amplitude based MEMS vibratory gyroscopes

Many variations on the vibrating element concept exist and all are driven by either a need for increased accuracy, or decreased cost. However, most MEMS vibratory gyroscopes use the measured amplitude of a Coriolis induced vibration to measure angular velocity, similarly to macro vibratory devices such as the tuning fork gyroscope. Usually a proof mass is periodically excited; when it is subjected to an angular velocity, the device induces a secondary orthogonal vibration due to the Coriolis effect. The amplitude of the secondary vibration is then used to determine the angular velocity. In the following, some of these configurations, together with some factors influencing their design are listed.

MEMS Tuning fork gyroscope (TFG): The MEMS TFG is a micro-mechanical equivalent of the original TFG, but with two silicon micro-machined counter-vibrating proof masses instead of vibrating tines [65; 66; 67]. Variations of the MEMS TFG are shown in Figures 2.12(a) and 2.12(b).

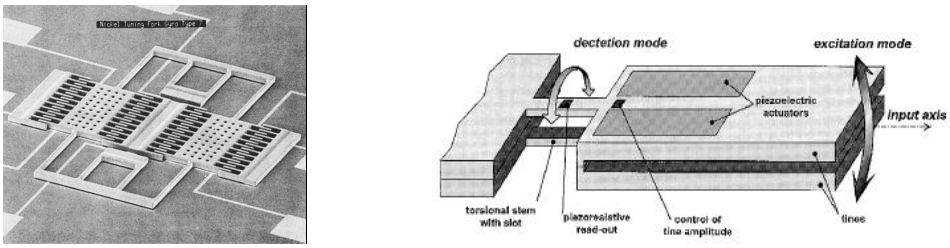

(a) Draper TFG [68] (b) DaimlerChrysler TFG [67]

Figure 2.12. Variations on MEMS Tuning fork Gyroscopes

MEMS proof mass gyroscopes: Most reported MEMS gyroscopes use single vibrating proof masses with in-plane, or in- and out-of-plane movement [8; 69; 70; 71], of which typical examples are depicted in Figure 2.13. Single proof mass vibrations can be used instead of balanced tuning fork vibrations, because linear acceleration signals can usually be filtered from the gyroscope vibration signals, or be compensated for by using the accelerometers in an IMU.

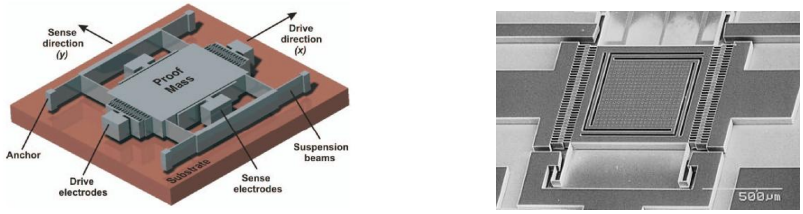

(a) In-plane gyro [11] (b) Out-of-plane gyro [71]

Figure 2.13. Single Proof Mass gyroscopes

Primary and secondary natural frequencies are ideally matched to induce a maximum secondary vibration amplitude, but this is constrained by manufacturing imperfections [14; 28]. The secondary vibration is used in either an open or closed-loop mode, where the sense axis vibration is nulled by a control system to obtain an output signal. In the closed-loop operation mode, the bandwith of the gyro can be increased, but the signal to noise ratio is decreased [37].

Out-of-plane squeeze film damping is larger than in-plane Couette flow damping and may have considerable effects on performance if out-of-plane excitation

is used[6]. However, out-of plane excitation can be larger due to excitation configurations not possible with in-plane excitation. Vacuum packing typically increases gyroscope sensitivity due to less damping, but complicates manufacturing and mode-matching due to narrow resonance spikes. The induced stresses and lifetime of hermitically sealed vacuum packaged devices need to be considered when using vacuum packaging [72; 73; 74].

Uncoupled gyroscopes: The highest performance MEMS gyroscopes seem to be those with uncoupled driving and sensing modes [17; 75; 76], of which some are depicted in Figure 2.14. In decoupling the driving and sensing modes, the cross-coupling effect of manufacturing defects are reduced and higher performances seem possible. One of these decoupling methods consists of a two-dimensional gimballed structure, which uses rotational vibrations instead of translational vibrations [77; 78]. Increased degrees of freedom with multi-proof-mass systems is another approach that gives an averaged effect and decreases the need for fine-tuned resonance. Using non-resonant vibration can also decrease the influence of disturbances [79; 80; 81].

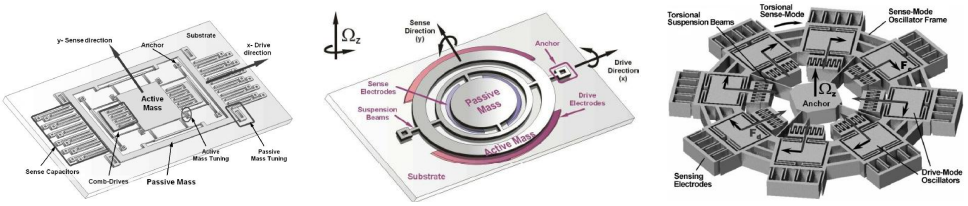

(a) Translational [82] (b) Rotational [82] (c) Multi-DOF [14]

Figure 2.14. Gyroscopes with decoupled Oscillation Modes

Vibrating rings: Vibrating rings are often used to measure rotation rate in MEMS. The concept does not necessarily use the same standing wave pattern as the HRG. In vibrating ring angular rate gyroscopes, a primary vibration mode is excited and a secondary mode is induced by the Coriolis effect under an applied angular velocity. Using a vibrating ring typically decreases the effect of spurious vibrations, increases sensitivity, decreases temperature dependance [12; 83] and compensation for imperfections is possible [12; 84]. A typical MEMS ring gyroscope is depicted in Figure 2.15.

Angular displacement MEMS gyroscopes: Recently, attempts have been made to implement angular displacement gyroscopes in MEMS using different tech-

[6]Squeeze film damping is due to the cushioning effect of thin films underneath MEMS structures, while Couette flow damping is due to viscous shear between sliding parallel plates.

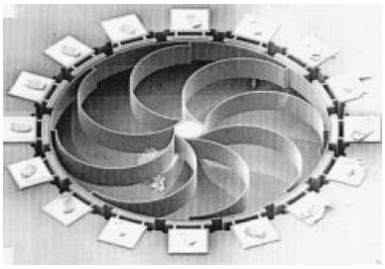

Figure 2.15. Vibrating Ring Gyroscope [12]

niques [10; 85]. However, this is probably best done with a standing wave pattern on a ring or cylinder, as mentioned in Section 2.2.5.2.

Two and three dimensional rotation rate gyroscopes: Vibrating structures that use 3-D vibrations to sense 2-D or 3-D rotation rates have been reported [9; 86; 87], and these devices use the combination of vibrations in all directions to determine rotation rate in more than one dimension, effectively replacing two or three single-axis gyroscopes with one.

2.2.7.2 Phase or frequency based MEMS vibratory gyroscopes

All the above mentioned concepts use the amplitude of vibration as an indication of rotation rate. The amplification of the small Coriolis vibration signal in MEMS gyroscopes make noise a considerable issue. Subsequently, the idea of using non-amplitude based gyroscopes has been suggested. Non-amplitude gyroscopes use changes in natural frequency or induced phase differences of the proof mass vibrations to measure rotation rate. The result is that output signals are frequency or phase modulated and theoretically makes the gyroscope less affected by noise. Therefore, it seems worthwhile to investigate these concepts further.

A single case of a frequency based gyroscope has been reported [88], but three phase operation methods in vibrating MEMS gyroscopes have been described in the literature, namely,

1. using the phase difference between multiple different vibrating elements [89],
2. using a one-dimensionally excited beam mass structure and measuring the phase difference between different signals induced by sensors placed on the beam [90],
3. and using a vibrating beam mass element with two-dimensional excitation [91; 92].

All the reported non-amplitude based gyroscope concepts have illustrated clearly that rotation rate can also be determined by frequency and phase detection methods under certain conditions, which mostly includes the equivalent of some form of dual excitation configuration. Each of the above mentioned concepts included some form of a theoretical explanation. However, a general model which clearly and effectively illustrates the vibration phase dependence on rotation rate could not be found in the recent literature[7].

The vibrating proof mass system used in vibratory gyroscopes is typically modelled by a two degree of freedom (2-DOF) spring mass-damper system, but is usually only studied with one excitation force. To explore the concept of using phase or frequency of vibrations to measure rotation rate further, two dimensional forcing of the 2-DOF spring-mass-damper system should be better understood. The general dynamics of the 2-DOF spring-mass-damper system with dual excitation forces and an applied rotation rate have previously been investigated by Linnett [93], who experimentally confirmed the formulation of vibration response ratios. Nevertheless, his formulation can be further explored to not only include ratios of the primary and secondary vibrations, but also individual responses, to better describe the more recent non-amplitude MEMS gyroscopes.

2.2.7.3 MEMS actuation and sensing

A wide variety of combinations of excitation and sensing mechanisms are used in MEMS and the same is true for their associated manufacturing processes. Each mechanism and manufacturing process has its own compatibility issues, advantages and disadvantages [94]. These are too extensive to go discuss in detail, especially since the design of a physical structure is beyond the scope of this thesis. Only a short summary of each is therefore given.

The sensing and actuation mechanisms mentioned below are used to measure the displacement and provide excitation of the vibrating element by various means. Although some have the ability to provide higher performance than others, their effectiveness are very dependant on how they are implemented.

Capacitive sensing and electrostatic excitation: Capacitive sensing uses the change in capacitance between a vibrating element and sense electrodes to measure displacement and is usually used in conjunction with electrostatic excitation. It can be used in parallel plate out-of-plane form, but then has the disadvantage of squeeze-film damping. A more preferred configuration is that of comb-like structures, which effectively increases the exposed electrical charge area and results in higher sensitivity. Capacitive sensing and electrostatic excitation usually has low temperature dependency, power consumption, manufac-

[7] More on this in section 3.5

turing cost and is preferred method excitation and detection in many commercialized MEMS applications [95].

Optical sensing: Optical sensing of vibration in vibratory MEMS gyroscope have been reported to give an improved performance on capacitive sensing [96; 97], but light-emitters and sensors can put great restrictions on manufacturing capabilities [98].

Piezoresistive measurement: Piezoresistivity occurs when the electrical resistance of a material changes due to an applied mechanical strain. Piezoresistive sensing is widely used as a passive measuring method, has simple readout circuitries and can easily be manufactured by material doping. It has a lower sensitivity than the above-mentioned mechanisms [28] and is more temperature dependent, but is typically cheaper.

Piezoelectric sensors and actuators: Piezoelectric sensors are similar to piezoresistive elements, but are active devices that generate voltage differences with the application of stress, in contrast to passive piezoresistive elements which only has a change in resistance. Piezoelectric materials can also generate displacement with an applied electrical charge, are easily manufactured and have low cost, but require more complicated readout electronics than piezoresistive elements.

Tunneling current: Tunneling current sensors take advantage of the extreme position sensitivity of electron tunneling [99]. It typically uses two conductors very close to each other (a few Angstroms). It is a relatively new concept that is very sensitive, has very low noise and good bandwidth capabilities, but is difficult to manufacture and costly. It has been implemented on accelerometers [28] and gyroscopes [100].

Magnetism: Although magnetism is not a preferred method of sensing due to various reasons, it is used effectively to create electromagnetic excitation when electric current is also applied in the drive modes of certain MEMS devices [13; 22].

Thermal expansion: MEMS Structures can be actuated by the thermal expansion of heated elements, but is typically not used for vibratory MEMS devices or gyroscopes.

Resonant Sensors: A type of sensor that uses the measured quantity to alter the element's natural frequency, is called a resonant sensor. Resonant sensors

should not be confused with sensors that measure some quantity with an amplitude of vibration at resonance. Resonant sensors have been successfully used to measure force, pressure and acceleration. The measured effect will usually alter some measuring element's natural frequency by changing the stiffness, mass or shape of the element. The resonating element can either be directly affected by the measured physical effect, or indirectly by attaching a resonant element to a secondary non-resonant element, such as a semi-static proof mass.

The resonating element can usually be micromachined in various shapes (eg. beams, shells and tuning forks) using a range of single crystal materials. These type of sensors have the advantage of a accuracy of up to ten times that of piezoresistive and capacitive sensors and a higher resolution, but the fabrication can be more complex and the requirement for packaging more demanding [94; 101]. The following advantages have been attributed to the resonant sensor concept: increased noise-resistance, sensitivity only to the natural frequency difference (insensitivity to other effects), as well as simplified signal electronics.

2.3 Summary

A wide variety of gyroscope types and their possible implementation in MEMS devices have been presented. The micro gas jet gyroscope and the micro-optical gyroscopes seem attractive concepts, but may prove difficult to investigate further with the available infrastructure. The vibratory MEMS gyroscopes seem to be of most interest in the literature and much effort is directed in improving these type of devices. Various MEMS vibration excitation and detection techniques also exist. Therefore, the most appealing concept for further exploration in this thesis, is that of phase or frequency based vibratory MEMS gyroscopes. The mathematical model is presented in the next chapter.

Chapter

3

Mathematical Model

With the choice of studying a phase or frequency based gyroscope made, an analytical model describing the vibratory system used to measure the applied rotation rate is needed. Usually the proof mass dynamics of a vibrating element amplitude-based gyroscope is modelled with spring-mass-damper system excited in one degree of freedom. However, in order to explore the frequency or phase of vibrations as a measure of rotation rate, a model of a two dimensionally excited two degree of freedom (2-DOF) spring-mass-damper with an applied rotation rate is needed.

The vibratory gyroscope model is presented as a point mass in space, fixed in a 2-DOF spring-mass-damper system. The equations of motion of the forced system subjected to an angular velocity are derived from first principles and a closed form solution of the steady state vibration is obtained by starting off in much the same way as Linnett [93]. The formulation of Linnett, which consists of vibration response ratios, is expanded into a generalized form that describes the motions of both degrees of freedom individually.

The general, dual excitation analytical model is then simplified to a symmetrical system and is applied to MEMS vibratory gyroscopes to illustrate the differences between one-dimensionally excited amplitude and two-dimensionally excited phase based operation methods. It is also shown that simplifications on the general dually excited 2-DOF model reduce to models used in the literature. Thereafter, the phase-based operation method is explored. Some advantages and disadvantages of the dual excitation and phase detection mode versus single excitation and amplitude detection are also explored and explained using the extended model.

3.1 Equations of motion

Consider a moving particle A, which represents the proof mass of a vibrating element gyroscope as shown in Figure 3.1(a). The particle is constrained to in-plane motion in a rotating local Cartesian reference frame xy, within an inertial reference frame $X_I Y_I$. The axis of rotation is normal to the plane[1], as illustrated in Figure 3.1(b).

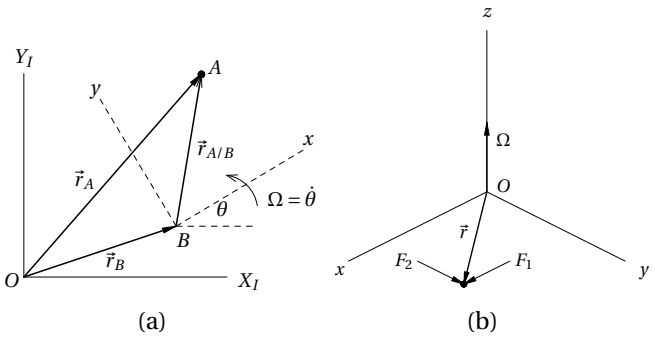

Figure 3.1. Moving particle in rotating frame

The position of the particle in the inertial frame is described by the vector $\vec{r}_A$, where

$$\vec{r}_A = \vec{r}_B + \vec{r}_{A/B}, \tag{3.1.1}$$

and the angular velocity of the rotating plane is $\vec{\Omega}$. The absolute velocity of the particle can be shown to be [103]

$$\vec{v}_A = \vec{v}_B + \vec{\Omega} \times \vec{r}_{A/B} + \vec{v}_{A/B}, \tag{3.1.2}$$

where $\vec{v}_{A/B}$ is the velocity of the particle A relative to the local xy axes. Differentiating (3.1.2) with respect to time gives the absolute acceleration of the particle in the inertial reference frame [59]

$$\vec{a}_A = \vec{a}_B + \vec{a}_{A/B} + \dot{\vec{\Omega}} \times \vec{r}_{A/B} + \vec{\Omega} \times (\vec{\Omega} \times \vec{r}_{A/B}) + 2\vec{\Omega} \times \vec{v}_{A/B}, \tag{3.1.3}$$

where $\vec{a}_{A/B}$ is the particle acceleration relative to the xy axes, $\vec{r} = \{x, y, 0\}$ and $\vec{\Omega} = \{0, 0, \Omega\}$. The absolute acceleration vector terms are obtained by expanding the cross products and a non-accelerating reference frame is assumed, making $\vec{a}_B = 0$, and (3.1.3) becomes

$$\vec{a}_A = \{\ddot{x}, \ddot{y}, 0\} + \{-y\dot{\Omega}, x\dot{\Omega}, 0\} + \{-x\Omega^2, -y\Omega^2, 0\} + \{-2\Omega\dot{y}, 2\Omega\dot{x}, 0\}. \tag{3.1.4}$$

[1] If angular velocity cross-sensitivities are of interest, see[102] for a study when the axis of rotation is not normal to the plane of motion.

The x and y acceleration components are then obtained as

$$\begin{aligned} a_x &= \ddot{x} - y\dot{\Omega} - x\Omega^2 - 2\Omega\dot{y}, \\ a_y &= \ddot{y} + x\dot{\Omega} - y\Omega^2 + 2\Omega\dot{x}. \end{aligned} \tag{3.1.5}$$

The 2-DOF spring-mass-damper arrangement that is typically used to model the proof mass of the vibrating gyroscope is depicted in Figure 3.2.

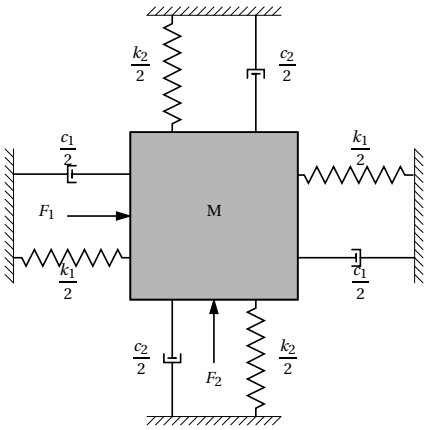

Figure 3.2. 2-DOF spring-mass-damper system

The proof mass vibration is excited by the harmonically applied forces $F_1 = P_1 e^{j\omega t}$ and $F_2 = P_2 e^{j\omega t}$. Newton's second law ($\vec{F} = m\vec{a}$) applies to absolute accelerations and can be used to link accelerations a_x and a_y in (3.1.5) to the applied forces F_1 and F_2. In assuming small displacements relative to spring lengths with no cross coupling, the force balance equation of the spring-mass-damper system together with Newton II then gives

$$\begin{aligned} P_1 e^{j\omega t} - k_1 x - c_1 \dot{x} &= m(\ddot{x} - y\dot{\Omega} - x\Omega^2 - 2\Omega\dot{y}), \\ P_2 e^{j\omega t} - k_2 y - c_2 \dot{y} &= m(\ddot{y} + x\dot{\Omega} - y\Omega^2 + 2\Omega\dot{x}). \end{aligned} \tag{3.1.6}$$

The natural frequencies of the non-rotating system are defined as $\omega_{n1} = \sqrt{\frac{k_1}{m}}$, $\omega_{n2} = \sqrt{\frac{k_2}{m}}$, and the damping ratios are $\zeta_1 = \frac{c_1}{2\sqrt{k_1 m}}$, $\zeta_2 = \frac{c_2}{2\sqrt{k_2 m}}$, while the excitation force amplitudes are $X_s = \frac{P_1}{k_1}$, $Y_s = \frac{P_2}{k_2}$.
Using the above mentioned expressions give the equations of motion

$$\begin{aligned} \ddot{x} + 2\zeta_1\omega_{n1}\dot{x} + (\omega_{n1}^2 - \Omega^2)x - 2\Omega\dot{y} &= \omega_{n1}^2 X_s e^{j\omega t}, \\ \ddot{y} + 2\zeta_2\omega_{n2}\dot{y} + (\omega_{n2}^2 - \Omega^2)y + 2\Omega\dot{x} &= \omega_{n2}^2 Y_s e^{j\omega t}. \end{aligned} \tag{3.1.7}$$

Note that the angular acceleration term $\dot{\Omega}$ has been neglected from (3.1.13), since it is usually small relative to the other terms in (3.1.3) (e.g. see [59]). Although

it can be a little difficult to confirm this conclusion through inspection, it may be motivated by the following reasoning: if the above-mentioned equations are non-dimensionalized by dividing both equations with ω_{n1}^2 and ω_{n2}^2 respectively, it would follow that $\frac{\dot{\Omega}}{\omega_n^2}$ is the dimensionless form of $\dot{\Omega}$. Since the natural frequencies of MEMS devices are in the order of a few kilohertz [59], it will follow that $\dot{\Omega} \ll \omega_n^2$, which confirms the resulting omission of $\dot{\Omega}$ from the ensuing equations. It should also be noted that it will take a harsh inertial environment to cause the angular acceleration term to become important [104].

3.1.1 System natural frequency

Natural frequencies are usually one of the principal attributes of any vibrating system, macroscopic or microscopic. To be able to draw conclusions on using frequency changes as a measure of rotation rate, it is necessary to investigate the influence of the applied rotation velocity on the resonance frequencies of the system. It may also present more insight into regular operation modes, especially since it is customary to excite vibratory MEMS structures at resonance.

The natural frequency of a system is defined as the frequency at which a system oscillates freely after an initial disturbance has been applied to it [105], and is determined analytically by solving the system equations of motion without any applied forces, e.g. by setting the right hand side of (3.1.13) equal to zero, giving

$$\begin{aligned} \ddot{x} + 2\zeta_1\omega_{n1}\dot{x} + (\omega_{n1}^2 - \Omega^2)x - 2\Omega\dot{y} = 0, \\ \ddot{y} + 2\zeta_2\omega_{n2}\dot{y} + (\omega_{n2}^2 - \Omega^2)y + 2\Omega\dot{x} = 0. \end{aligned} \tag{3.1.8}$$

Assuming solutions of the form given in [105] as

$$x(t) = C_1 e^{st}, y(t) = C_2 e^{st}, \tag{3.1.9}$$

and substitution into (3.1.8), gives

$$\begin{aligned} [s^2 + 2\zeta_1\omega_{n1}s + (\omega_{n1}^2 - \Omega^2)]C_1 - 2\Omega s C_2 = 0, \\ [s^2 + 2\zeta_2\omega_{n2}s + (\omega_{n2}^2 - \Omega^2)]C_2 + 2\Omega s C_1 = 0. \end{aligned} \tag{3.1.10}$$

It was previously mentioned that numerous MEMS gyroscopes are designed to have equal natural frequencies in both directions. Damping will also be of the same order in both the x and y directions when similar geometries and configurations are used. In order simplify the solution, equal undamped natural frequencies and damping ratios are assumed (i.e. a symmetrical system), making $\omega_{n1} = \omega_{n2} = \omega_n$ and $\zeta_1 = \zeta_2 = \zeta$.

For (3.1.10) to have non-zero solutions, the constants C_1 and C_2 must not be zero [88; 106]. Hence, the solution is obtained by the following condition:

$$\begin{vmatrix} s^2+2\zeta\omega_n s+(\omega_n^2-\Omega^2) & -2\Omega s \\ 2\Omega s & s^2+2\zeta\omega_n s+(\omega_n^2-\Omega^2) \end{vmatrix} = 0.$$

Hence,

$$[s^2+2\zeta\omega_n s+(\omega_n^2-\Omega^2)]^2 = -[2\Omega s]^2,$$

$$s^2+2\zeta\omega_n s+(\omega_n^2-\Omega^2) = \pm j(2\Omega s),$$

$$s^2+2(\zeta\omega_n \pm j\Omega)s+(\omega_n^2-\Omega^2) = 0,$$

$$s_{1,2} = -(\zeta\omega_n \pm j\Omega) \pm \sqrt{\zeta^2\omega_n^2 \pm 2j\Omega\zeta\omega_n - \omega_n^2}.$$

The undamped natural frequencies for the system are obtained when $\zeta = 0$, giving

$$s_{1,2} = \mp j\Omega \pm \omega_n = \pm j|\omega_n \pm \Omega|,$$

in turn giving the undamped natural frequencies $\omega_{1,2_\Omega}$ due to applied rotation velocity Ω as

$$\omega_{1,2_\Omega} = |\omega_n \pm \Omega|.$$

Calculating the difference between the two natural frequencies gives the useful expression for the differential natural frequency,

$$\Delta\omega_\Omega = \omega_{1_\Omega} - \omega_{2_\Omega} = 2\Omega. \tag{3.1.11}$$

The above mentioned equations show that the rotational velocity of the system directly affects the damped and undamped natural frequencies of the 2-DOF system. This implies that it is possible to design a resonant sensor that determines some input rotational velocity directly, by measuring the difference between the x and y system resonance frequencies. In implementing such a concept, a two-dimensional resonator may be used.

An inherent disadvantage of designing a gyroscope that uses direct changes in resonance frequency (i.e. a direct frequency output gyroscope), is the small scale factor of the sensor resulting from (3.1.11), which will only be $\frac{1}{360}\frac{Hz}{°/s}$ (0.0028 Hz per degree per second). This is quite small compared to other sensors that use changes in resonance frequency, which have scale factors in the order of tens and hundreds of hertz per measurand [101].

The small scale factor implies a small change of natural frequency relative to the magnitude of the frequency. The operating frequency of MEMS devices are usually in the order of a few kilohertz, but the induced change in resonance frequency is only a few hertz. Consider a resonator operating at 1kHz: to induce a 1% (10Hz) difference of the operating frequency, an angular velocity of $1800°/s$ needs to be applied.

The small influence of the rotation velocity is only relative, since the resolution and accuracy of the device is dependent on the frequency measuring electronics resolution and accuracy. Usually frequency based devices have an accuracy in the order of 500ppm (parts per million) [101], which will theoretically make a resonance frequency-based gyroscope accurate to $0.09^\circ/s$. To measure the small frequency changes accurately may also necessitate many oscillation cycles, which means that only low bandwidths can be achieved. These factors possibly make a frequency-based gyroscope suitable for stabilization and some commercial uses, but not for high-end military applications and inertial navigation.

One author has described the theory of using a resonating element as a direct frequency output gyroscope [88]. He has shown that the method has an inherent disadvantage, being that there exists a frequency lock-in effect between the x and y vibrations which is highly affected by the amount of electromechanical coupling in the system. The electromechanical coupling is in turn dependant on the mechanical system and the driving electronics of the resonator element. The lock-in effect is especially problematic at low angular velocities and low frequency differences. When lock-in occurs, the device conveys zero rotation velocity. The system also has non-linear behaviour in some operating ranges, making a play-off between non-linearities and the lock-in effect necessary [88]. These factors possibly make further investigation of the use of resonance frequency as a measure of rotation rate, especially from a mechanical vibration analysis point of view, unattractive. For the moment, the vibratory system is further explored.

3.1.2 Harmonic forced response

The response of the forced system is now analytically determined by inclusion of the forcing terms on the right hand side of (3.1.7), making the solution thereof more involved. In determining the system response analytically, techniques to solve coupled equations are required, which means that it may be worthwhile to include extra terms to describe mechanical coupling effects with little extra effort. The addition of extra coupling terms makes the analytical model more general, and the mechanical coupling can be useful to account for future investigations of manufacturing imperfections. Note that the coupling effects will have an effect on the system natural frequencies as well, but is not shown in the previous section to better illustrate the effect of rotation velocity on the system natural frequency. Adding additional inertial, damping and stiffness coupling terms to (3.1.6), as done by Linnett [93], gives

$$\begin{aligned} P_1 e^{j\omega t} - c_1\dot{x} - k_1 x - c_i\ddot{y} - c_d\dot{y} - c_s y &= m(\ddot{x} - y\dot{\Omega} - x\Omega^2 - 2\Omega\dot{y}), \\ P_2 e^{j\omega t} - c_2\dot{y} - k_2 y - c_i\ddot{x} - c_d\dot{x} - c_s x &= m(\ddot{y} + x\dot{\Omega} - y\Omega^2 + 2\Omega\dot{x}), \end{aligned} \tag{3.1.12}$$

where c_i, c_d, c_s denote inertial, damping and stiffness coupling coefficients respectively. The mechanically coupled equations of motion of a two-dimensionally

excited two degree of freedom (2-DOF) spring-mass-damper system subject to a rotation velocity are therefore given as

$$\begin{aligned}\ddot{x}+2\zeta_1\omega_{n1}\dot{x}+(\omega_{n1}^2-\Omega^2)x+u_i\ddot{y}+(\omega_{n1}u_{d1}-2\Omega)\dot{y}+\omega_{n1}^2u_{s1}y=\omega_{n1}^2X_se^{j\omega t},\\ \ddot{y}+2\zeta_2\omega_{n2}\dot{y}+(\omega_{n2}^2-\Omega^2)y+u_i\ddot{x}+(\omega_{n2}u_{d2}+2\Omega)\dot{x}+\omega_{n2}^2u_{s2}x=\omega_{n2}^2Y_se^{j\omega t}.\end{aligned} \tag{3.1.13}$$

Here, $u_i=\frac{c_i}{m}$, $u_d=\frac{c_d}{\omega_n m}$ and $u_s=\frac{c_s}{\omega_n^2 m}$ are the non-dimensional inertial, damping and stiffness coupling coefficients respectively.

The harmonic solution for x and y will be of the form [105]

$$\begin{aligned}x&=\|X\|e^{j(\omega t+\phi)}=\|X\|e^{j\phi}e^{j\omega t}=Xe^{j\omega t},\\ y&=\|Y\|e^{j(\omega t+\varphi)}=\|Y\|e^{j\varphi}e^{j\omega t}=Ye^{j\omega t}.\end{aligned} \tag{3.1.14}$$

Clearly, (3.1.14) shows that X and Y are phasors that contain the amplitude and phase information of the complex harmonic solution. Expressions to obtain the first and second derivatives of displacement are then obtained by

$$\dot{x}=\frac{dx}{dt}=j\omega Xe^{j\omega t},\dot{y}=\frac{dy}{dt}=j\omega Ye^{j\omega t}, \tag{3.1.15}$$

and

$$\ddot{x}=\frac{d^2x}{dt^2}=-\omega^2Xe^{j\omega t},\ddot{y}=\frac{d^2y}{dt^2}=-\omega^2Ye^{j\omega t}, \tag{3.1.16}$$

hence (3.1.13) become

$$\begin{aligned}[-\omega^2+2j\omega\zeta_1\omega_{n1}+\omega_{n1}^2-\Omega^2]X+[-u_i\omega^2+j\omega(\omega_{n1}u_{d1}-2\Omega)+\omega_{n1}^2u_{s1}]Y=\omega_{n1}^2X_s,\\ [-\omega^2+2j\omega\zeta_2\omega_{n2}+\omega_{n2}^2-\Omega^2]Y+[-u_i\omega^2+j\omega(\omega_{n2}u_{d2}+2\Omega)+\omega_{n2}^2u_{s2}]X=\omega_{n2}^2Y_s.\end{aligned} \tag{3.1.17}$$

Non-dimensionalizing the above-mentioned equations and grouping real and imaginary terms, gives the more compact form

$$\begin{aligned}[(1-r_1^2-l_1^2)+j(2\zeta_1r_1)]X+[(u_{s1}-u_ir_1^2)+jr_1(u_{d1}-2l_1)]Y=X_s,\\ [(1-r_2^2-l_2^2)+j(2\zeta_2r_2)]Y+[(u_{s2}-u_ir_2^2)+jr_2(u_{d2}+2l_2)]X=Y_s,\end{aligned} \tag{3.1.18}$$

where $r_1=\dfrac{\omega}{\omega_{n1}}$, $r_2=\dfrac{\omega}{\omega_{n2}}$, $l_1=\dfrac{\Omega}{\omega_{n1}}$, $l_2=\dfrac{\Omega}{\omega_{n2}}$.

Note that (3.1.18) is the same system of equations given by Linnett [93; 106] and basically the same derivation method as Linnett has been followed until now.

From here on a different solution approach to Linnett is taken, whereby extended expressions for X, Y and $\frac{Y}{X}$ are derived to be able to account for the response of

both directions, both individually and combined[2]. To make the algebra a little less tedious, (3.1.18) is made more compact by defining

$$\begin{aligned} A &= (1 - r_1^2 - l_1^2) + j(2\zeta_1 r_1), \\ B &= (u_{s1} - u_i r_1^2) + j r_1 (u_{d1} - 2l_1), \\ C &= (1 - r_2^2 - l_2^2) + j(2\zeta_2 r_2), \\ D &= (u_{s2} - u_i r_2^2) + j r_2 (u_{d2} + 2l_2), \end{aligned} \tag{3.1.19}$$

hence (3.1.18) becomes

$$AX + BY = X_s, \tag{3.1.20}$$

$$CY + DX = Y_s. \tag{3.1.21}$$

Now, from (3.1.21),

$$Y = \frac{Y_s - DX}{C}, \tag{3.1.22}$$

which substituted into (3.1.20) and solving for X, yields

$$X = \frac{CX_s - BY_s}{AC - BD}. \tag{3.1.23}$$

Thereafter substitution of (3.1.23) into (3.1.22) gives

$$Y = \frac{AY_s - DX_s}{AC - BD}. \tag{3.1.24}$$

Then,

$$\frac{Y}{X} = \frac{AY_s - DX_s}{CX_s - BY_s}. \tag{3.1.25}$$

Hence, the expressions for X and Y are obtained as

$$X = \frac{(1 - r_2^2 - l_2^2)X_s - (u_{s1} - u_i r_1^2)Y_s + j[2\zeta_2 r_2 X_s + r_1(u_{d1} - 2l_1)Y_s]}{AC - BD}, \tag{3.1.26}$$

$$Y = \frac{(1 - r_1^2 - l_1^2)Y_s - (u_{s2} - u_i r_2^2)X_s + j[2\zeta_1 r_1 Y_s - r_2(u_{d2} + 2l_2)X_s]}{AC - BD}. \tag{3.1.27}$$

With $AC - BD$ obtained from (3.1.19) and stated as

$$\begin{aligned} AC - BD = {} & [1 - r_1^2 - l_1^2 + 2j\zeta_1 r_1][1 - r_2^2 - l_2^2 + 2j\zeta_2 r_2] \\ & - [u_{s1} - u_i r_1^2 + j r_1(u_{d1} - 2l_1)][u_{s2} - u_i r_2^2 + j r_2(u_{d2} + 2l_2)] \end{aligned}$$

It can be seen that obviously (3.1.26) and (3.1.27) are quite cumbersome, but can be useful when the system response in the presence of coupling effects is desired. Simplifications of these equations give the coupling equations derived by

[2] Linnett only considered simplifications of $\frac{Y}{X}$.

Mochida *et al.* [71]. The quotient is more compact and may be expanded for the sake of clarity[3] as

$$\frac{Y}{X} = \frac{(1-r_1^2-l_1^2)Y_s - (u_{s2}-u_i r_2^2)X_s + j[2\zeta_1 r_1 Y_s - r_2(u_{d2}+2l_2)X_s]}{(1-r_2^2-l_2^2)X_s - (u_{s1}-u_i r_1^2)Y_s + j[2\zeta_2 r_2 X_s + r_1(u_{d1}-2l_1)Y_s]}, \tag{3.1.28}$$

which is of the form $\frac{a+bi}{c+di}$. X and Y can also be written in this form, but for now $\frac{Y}{X}$ will suffice. Since the above mentioned solutions describe the complex motion of X, Y and $\frac{Y}{X}$ with phasors, the magnitude and the phase may now be extracted. These expressions are quite lengthy, but the investigation can be expedited when a complex number κ is introduced, of the form

$$\kappa = \frac{a+bi}{c+di} = \|\kappa\| e^{j\theta}. \tag{3.1.29}$$

It can be shown that (3.1.29) results in [105]

$$\kappa = \frac{(ac+bd)+i(bc-ad)}{c^2+d^2} = \frac{ac+bd}{c^2+d^2} + i\left(\frac{bc-ad}{c^2+d^2}\right). \tag{3.1.30}$$

The magnitude of κ is then given by [107]

$$\|\kappa\| = \sqrt{\left(\frac{ac+bd}{c^2+d^2}\right)^2 + \left(\frac{bc-ad}{c^2+d^2}\right)^2} = \sqrt{\frac{a^2+b^2}{c^2+d^2}}, \tag{3.1.31}$$

whereas the phase θ is

$$\theta = \arg(\kappa) = \arctan\left(\frac{bc-ad}{ac+bd}\right), \tag{3.1.32}$$

which can be simplified using the trigonometric identity [108]

$$\arctan(x) - \arctan(y) = \arctan\left(\frac{x-y}{1+xy}\right). \tag{3.1.33}$$

Hence,

$$\theta = \arg(\kappa) = \arctan\left(\frac{b}{a}\right) - \arctan\left(\frac{d}{c}\right). \tag{3.1.34}$$

The expressions for magnitude (3.1.31) and phase (3.1.34) can also be obtained by the property that the quotient of two complex numbers ($a+bi$ and $c+di$) results in the moduli to be divided and the arguments to be subtracted [107].

[3] The significance of defining the quotient $\frac{Y}{X}$ is to illuminate the determination of phase differences and to facilitate illustration of the solution process.

Using the forms of (3.1.31) and (3.1.34), the magnitude and phase of (3.1.28) are respectively obtained as

$$\left|\frac{Y}{X}\right| = \sqrt{\frac{[(1-r_1^2-l_1^2)Y_s-(u_{s2}-u_i r_2^2)X_s]^2+[2\zeta_1 r_1 Y_s - r_2(u_{d2}+2l_2)X_s]^2}{[(1-r_2^2-l_2^2)X_s-(u_{s1}-u_i r_1^2)Y_s]^2+[2\zeta_2 r_2 X_s + r_1(u_{d1}-2l_1)Y_s]^2}}, \tag{3.1.35}$$

and

$$\arg\left(\frac{Y}{X}\right) = \varphi - \phi = \arctan\left(\frac{2\zeta_1 r_1 Y_s - r_2(u_{d2}+2l_2)X_s}{(1-r_1^2-l_1^2)Y_s-(u_{s2}-u_i r_2^2)X_s}\right) - \arctan\left(\frac{2\zeta_2 r_2 X_s + r_1(u_{d1}-2l_1)Y_s}{(1-r_2^2-l_2^2)X_s-(u_{s1}-u_i r_1^2)Y_s}\right). \tag{3.1.36}$$

The same technique can be applied to obtain the individual X and Y amplitude and phase responses from (3.1.26) and (3.1.27), but is not done at present for the mechanically coupled case. Another form of the above-mentioned equations was used by Linnett to investigate the use of the system as a macro-mechanical vibratory angular velocity sensor [93]. He used a macro-mechanical experimental setup to confirm the theory for the one-dimensional excitation case. He mentioned that a practical instrument should be smaller and lighter, and this is indeed the case with MEMS. Linnett also mentioned that it would be possible to use the phase angle to measure small rates of turn, possibly making the measurement less dependent on the signal to noise ratio.

Note that if the driving forces in (3.1.36) are equal (i.e. $X_s = Y_s$), the phase difference between the mechanically coupled vibrations becomes invariant to the driving force, giving

$$\arg\left(\frac{Y}{X}\right) = \varphi - \phi = \arctan\left(\frac{2\zeta_1 r_1 - r_2(u_{d2}+2l_2)}{(1-r_1^2-l_1^2)-(u_{s2}-u_i r_2^2)}\right) - \arctan\left(\frac{2\zeta_2 r_2 + r_1(u_{d1}-2l_1)}{(1-r_2^2-l_2^2)-(u_{s1}-u_i r_1^2)}\right), \tag{3.1.37}$$

which however, is still a function of coupling effects. Although the coupled equations of motion (3.1.13) may be useful in sensitivity analyses, they are too involved to allow an "intuitive feel" for the system. Simplifications are beneficial to improve insight into the system response and the mechanically uncoupled system response is used hereafter.

3.2 Mechanically uncoupled asymmetrical system

Asymmetrical structures are common in MEMS gyroscopes and are typically those that use in-plane excitation and out-of-plane detection [28], but many in-plane (z-axis) asymmetrical gyroscopes also exist [8]. In a system where no mechanical coupling occurs, c_i, c_d, c_s and u_i, u_d, u_s equal zero, and the equations of motion again simplify to

$$\begin{aligned} \ddot{x} + 2\zeta_1\omega_{n1}\dot{x} + (\omega_{n1}^2 - \Omega^2)x - 2\Omega\dot{y} &= \omega_{n1}^2 X_s e^{j\omega t}, \\ \ddot{y} + 2\zeta_2\omega_{n2}\dot{y} + (\omega_{n2}^2 - \Omega^2)y + 2\Omega\dot{x} &= \omega_{n2}^2 Y_s e^{j\omega t}. \end{aligned} \tag{3.2.1}$$

This is a more digestible form than (3.1.13) and is common in vibrating MEMS gyroscope papers, but usually in more simplified forms. Usually, only one excitation force is studied (making $Y_s = 0$) and the Ω^2 term is also generally neglected[4]. Although the system is mechanically uncoupled, i.e. there are no stiffness imperfections or mass eccentricities present, the equations of motion (3.2.1) are still a mathematically coupled system. To be more precise, it is a system of linear second order differential equations coupled in the first derivative of x and y. The reason being that the Coriolis acceleration, just like damping, is directly linked to the velocities $\dot{x}$ and $\dot{y}$, with $-2\Omega\dot{y}$ and $2\Omega\dot{x}$ being the Coriolis acceleration terms in the x and y directions. The applied angular velocity therefore acts as a coupled damping term that transfers energy between the x and y axes. Furthermore, the centripetal acceleration term Ω^2 is subtracted from ω_n^2, a spring stiffness term, which suggests that the angular velocity influences the system stiffness and resonance frequency, a conclusion confirmed in Section 3.1.1. The non-dimensionalized form (3.1.18) is now simplified to

$$\begin{aligned} [(1 - r_1^2 - l_1^2) + j(2\zeta_1 r_1)]X - j[2r_1 l_1]Y &= X_s, \\ [(1 - r_2^2 - l_2^2) + j(2\zeta_2 r_2)]Y + j[2r_2 l_2]X &= Y_s, \end{aligned} \tag{3.2.2}$$

and the individual responses become

$$\begin{aligned} X &= \frac{(1 - r_2^2 - l_2^2)X_s + 2j[\zeta_2 r_2 X_s + r_1 l_1 Y_s]}{\xi + \gamma j}, \\ Y &= \frac{(1 - r_1^2 - l_1^2)Y_s + 2j[\zeta_1 r_1 Y_s - r_2 l_2 X_s]}{\xi + \gamma j}. \end{aligned} \tag{3.2.3}$$

with

$$\xi = (1 - r_1^2 - l_1^2)(1 - r_2^2 - l_2^2) - 4r_1 r_2(\zeta_1\zeta_2 + l_1 l_2),$$

and

$$\gamma = 2[\zeta_1 r_1(1 - r_2^2 - l_2^2) + \zeta_2 r_2(1 - r_1^2 - l_1^2)].$$

[4] In this thesis, the Ω^2 term is not neglected

Using the form of (3.1.31), the magnitudes are obtained as

$$\begin{aligned} \|X\| &= \sqrt{\frac{[(1-r_2^2-l_2^2)X_s]^2+4[\zeta_2 r_2 X_s + r_1 l_1 Y_s]^2}{\xi^2+\gamma^2}}, \\ \|Y\| &= \sqrt{\frac{[(1-r_1^2-l_1^2)Y_s]^2+4[\zeta_1 r_1 Y_s - r_2 l_2 X_s]^2}{\xi^2+\gamma^2}}, \end{aligned} \tag{3.2.4}$$

and the form (3.1.34) give the phases as

$$\begin{aligned} \arg(X) = \phi &= \arctan\left(\frac{2[\zeta_2 r_2 X_s + r_1 l_1 Y_s]}{(1-r_2^2-l_2^2)X_s}\right) - \arctan\left(\frac{\gamma}{\xi}\right), \\ \arg(Y) = \varphi &= \arctan\left(\frac{2[\zeta_1 r_1 Y_s - r_2 l_2 X_s]}{(1-r_1^2-l_1^2)Y_s}\right) - \arctan\left(\frac{\gamma}{\xi}\right). \end{aligned} \tag{3.2.5}$$

The phase difference between the induced vibrations are

$$\Delta\phi = \varphi - \phi = \arctan\left(\frac{2[\zeta_1 r_1 Y_s - r_2 l_2 X_s]}{(1-r_1^2-l_1^2)Y_s}\right) - \arctan\left(\frac{2[\zeta_2 r_2 X_s + r_1 l_1 Y_s]}{(1-r_2^2-l_2^2)X_s}\right). \tag{3.2.6}$$

Note that, for equal driving forces, $X_s = Y_s$, the phase difference $\Delta\phi$ and indeed the individual phases (ϕ and φ) become invariant with respect to the driving forces. The significance of unequal driving forces is discussed later on.

The asymmetrical equations of motion and the resulting responses have many variables and are difficult to visualize, despite being more comprehensible than the mechanically coupled equations. Making the system symmetrical with equal properties in the x and y directions is a welcome simplification and allows for improved visualization of the system response.

3.3 Symmetrical system

Numerous MEMS gyroscopes are designed to be symmetrical [75; 109; 110; 111]. When symmetry is assumed, it follows that $k_1 = k_2$, $c_1 = c_2$, $\omega_{n1} = \omega_{n2}$, $\zeta_1 = \zeta_2$, thereby making $r_1 = r_2 = r$ and $l_1 = l_2 = l$, giving the response

$$\begin{aligned} X &= \frac{(1-r^2-l^2)X_s + 2jr[\zeta X_s + l Y_s]}{(1-r^2-l^2)^2 - 4r^2(\zeta^2+l^2) + 4j\zeta r(1-r^2-l^2)}, \\ Y &= \frac{(1-r^2-l^2)Y_s + 2jr[\zeta Y_s - l X_s]}{(1-r^2-l^2)^2 - 4r^2(\zeta^2+l^2) + 4j\zeta r(1-r^2-l^2)}. \end{aligned} \tag{3.3.1}$$

Again, using the form of (3.1.31), the magnitudes of the responses are obtained as

$$\begin{aligned}\|X\| &= \sqrt{\frac{[(1-r^2-l^2)X_s]^2+4r^2[\zeta X_s+lY_s]^2}{[(1-r^2-l^2)^2-4r^2(\zeta^2+l^2)]^2+16r^2[\zeta(1-r^2-l^2)]^2}},\\ \|Y\| &= \sqrt{\frac{[(1-r^2-l^2)Y_s]^2+4r^2[\zeta Y_s-lX_s]^2}{[(1-r^2-l^2)^2-4r^2(\zeta^2+l^2)]^2+16r^2[\zeta(1-r^2-l^2)]^2}},\end{aligned} \tag{3.3.2}$$

and from (3.1.34), the phases are

$$\begin{aligned}\arg(X) = \phi &= \arctan\left(\frac{2r[\zeta X_s+lY_s]}{(1-r^2-l^2)X_s}\right)-\arctan\left(\frac{4\zeta r(1-r^2-l^2)}{(1-r^2-l^2)^2-4r^2(\zeta^2+l^2)}\right),\\ \arg(Y) = \varphi &= \arctan\left(\frac{2r[\zeta Y_s-lX_s]}{(1-r^2-l^2)Y_s}\right)-\arctan\left(\frac{4\zeta r(1-r^2-l^2)}{(1-r^2-l^2)^2-4r^2(\zeta^2+l^2)}\right).\end{aligned} \tag{3.3.3}$$

The phase difference between X and Y is then

$$\Delta\phi = \varphi-\phi = \arctan\left(\frac{2[\zeta r Y_s-rlX_s]}{(1-r^2-l^2)Y_s}\right)-\arctan\left(\frac{2[\zeta r X_s+rlY_s]}{(1-r^2-l^2)X_s}\right). \tag{3.3.4}$$

Again using the trigonometric identity

$$\arctan\left(\frac{x-y}{1+xy}\right) = \arctan(x)-\arctan(y), \tag{3.3.5}$$

(3.3.4) simplifies to

$$\Delta\phi = \arctan\left(\frac{-2rl(1-r^2-l^2)(X_s^2+Y_s^2)}{X_sY_s(1-r^2-l^2)^2+4r^2(\zeta X_s+lY_s)(\zeta Y_s-lX_s)}\right). \tag{3.3.6}$$

Now that the expressions for the amplitude and phase response have been derived, they can be examined. The symmetrical case is primarily investigated.

3.4 Symmetrical system response

The different angular velocity sensing modes are explored, using the previously stated system response expressions. The commonly used vibration amplitude measurement scheme to measure rotation velocity is stated first, whereafter the phase measurement scheme is introduced. A ζ-value of 0.05 is used for illustration, as it corresponds to a Q-value of ten (using $\zeta = \frac{1}{2Q}$), which is well within the expected range of commercial MEMS comb-drive devices such as accelerometers and gyroscopes [59].

3.4.1 One-dimensional excitation

If a driving force of constant amplitude and phase is applied in the x-direction with no excitation in the y-direction ($Y_s = 0$), the amplitude response (3.3.2) becomes

$$\begin{aligned} \|X\| &= X_s \sqrt{\frac{(1-r^2-l^2)^2+4r^2\zeta^2}{[(1-r^2-l^2)^2-4r^2(\zeta^2+l^2)]^2+16r^2[\zeta(1-r^2-l^2)]^2}}, \\ \|Y\| &= X_s|l| \sqrt{\frac{4r^2}{[(1-r^2-l^2)^2-4r^2(\zeta^2+l^2)]^2+16r^2[\zeta(1-r^2-l^2)]^2}}. \end{aligned} \tag{3.4.1}$$

Consider the amplitude response of $\|X\|$ and $\|Y\|$. Both are directly proportional to the forcing size X_s and for comparable values of r and l in the order of unity the response is difficult to visualize through inspection. However, with closer examination of $\|Y\|$, it is seen that small values of l makes the denominator of $\|Y\|$ a negligible function of l, effectively making $\|Y\|$ a linear function of rotation rate l. The amplitude responses for $\|X\|$ and $\|Y\|$ with a forcing amplitude of $X_s = 1$ are depicted in Figures 3.3 and 3.4 for larger and smaller ranges of l respectively. The amplitude does not seem to be a very useful measure of rotation rate over a large range rotation rates $-0.5 < l < 0.5$ (Figure 3.3). However, Figure 3.4 shows that the amplitude is indeed a useful measure of rotation rate over a smaller range of l. This need not disqualify the one-dimensional excitation operation mode as a measurement of rotation rate, since $l = 0.5$ may correspond to a very large Ω, if the natural frequency ω_n is large (recall that $l = \frac{\Omega}{\omega_n}$).

Note that Figures 3.3 and 3.4 also show the change of the system resonance frequency, which is visible in Figure 3.3, but not Figure 3.4. The change of resonance frequency is therefore only visible at larger rotation rates and visually confirms the predictions made in the system natural frequency analysis (Section 3.1.1).

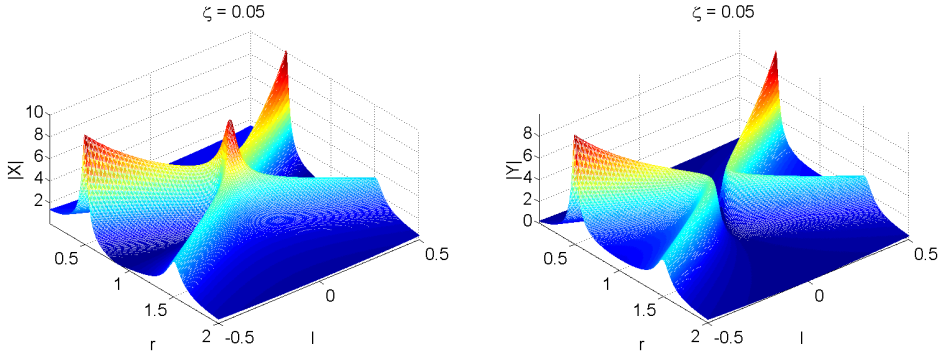

(a) $\|X\|$ (b) $\|Y\|$

Figure 3.3. General amplitude response for $X_s = 1$, $Y_s = 0$ and $\zeta = 0.05$

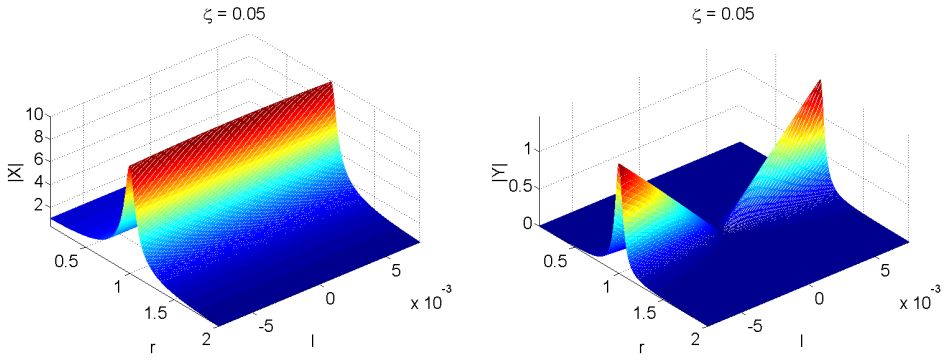

(a) $\|X\|$ (b) $\|Y\|$

Figure 3.4. Small rotation rate amplitude response for $X_s = 1$, $Y_s = 0$ and $\zeta = 0.05$

Using $X_s = 1$ and $Y_s = 0$ in (3.3.3), the phases are obtained as

$$\begin{aligned}\phi &= \arg(X) = \arctan\left(\frac{2r\zeta}{1-r^2-l^2}\right) - \arctan\left(\frac{4\zeta r(1-r^2-l^2)}{(1-r^2-l^2)^2-4r^2(\zeta^2+l^2)}\right),\\ \varphi &= \arg(Y) = \pm\frac{\pi}{2} - \arctan\left(\frac{4\zeta r(1-r^2-l^2)}{(1-r^2-l^2)^2-4r^2(\zeta^2+l^2)}\right),\end{aligned} \tag{3.4.2}$$

which are depicted in Figure 3.5 for $-0.5 < l < 0.5$. The phase response has many discontinuities[5], which directly arise from the properties of the arctan function. The quirks of using arctan are given in Appendix A. The presence of the various discontinuities make conclusions about the influence of rotation rate on the phase of the vibrations difficult, especially since the phases are not unwrapped[6]. Unwrapping the phases can be cumbersome, so instead the difference between the phases are taken to eliminate most of the discontinuities. This has the additional advantage of referencing the phases of both directions relative to each other.

The phase difference is given by

$$\Delta\phi = \varphi - \phi = \pm\frac{\pi}{2} - \arctan\left(\frac{2\zeta r}{1-r^2-l^2}\right), \tag{3.4.3}$$

and is depicted in Figures 3.7(a) and 3.7(b) for large and small rotation rates. The phase difference between the x and y vibrations is seen to not be a useful function of angular velocity l and cannot be used as a measure of rotation velocity in this operation mode. However, the phase difference has a jump of π when the rotation direction changes, effectively inverting the signal.

[5]The serrated edges at the discontinuities are only due to limitations of meshed plotting.

[6]Unwrapping is where multiples of 2π are added or subtracted in order to eliminate discontinuities due to full circle phase jumps [112].

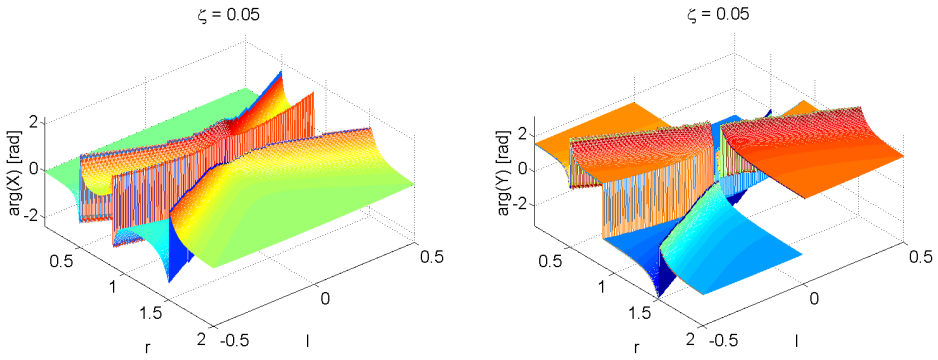

(a) $\arg(X) = \phi$ (b) $\arg(Y) = \varphi$

Figure 3.5. General phase response for $X_s = 1$, $Y_s = 0$ and $\zeta = 0.05$

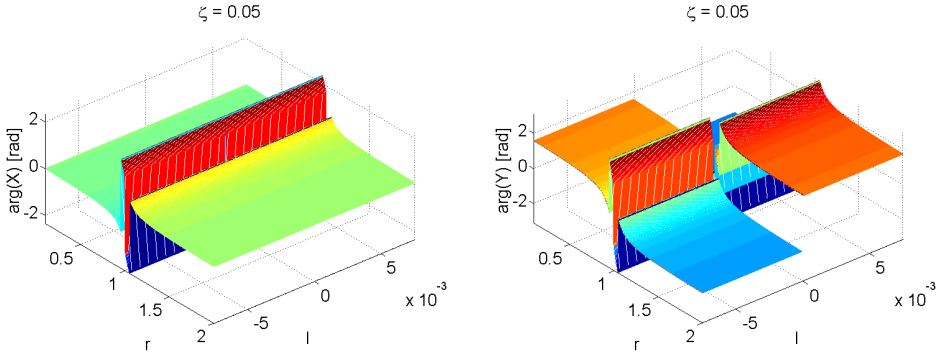

(a) $\arg(X) = \phi$ (b) $\arg(Y) = \varphi$

Figure 3.6. Small rotation rate phase response for $X_s = 1$, $Y_s = 0$ and $\zeta = 0.05$

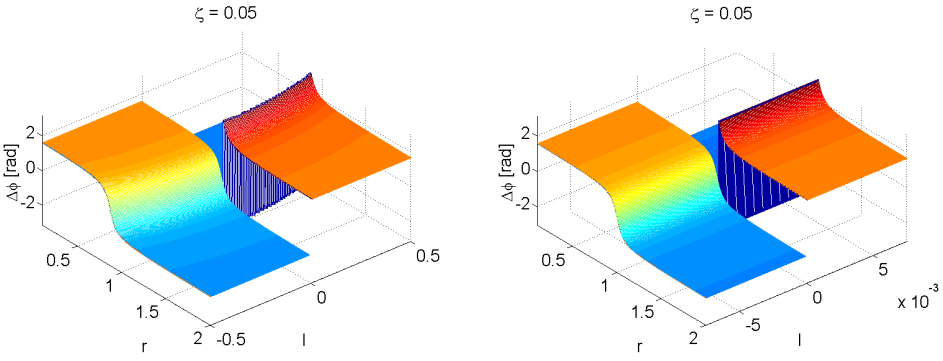

(a) $\Delta\phi$ (b) $\Delta\phi$ Small rotation rate

Figure 3.7. Phase difference $\Delta\phi$ for $X_s = 1$, $Y_s = 0$ and $\zeta = 0.05$

The above mentioned statements illustrate why harmonically exciting a primary vibration and measuring a secondary vibration amplitude can be used to mea-

sure rotation rate. This is however only possible at relatively small rotation rates (normalized with the natural frequency of the system). The phase only provides an indication of the direction of the applied rotation rate.

3.4.2 One-dimensional excitation and amplitude detection

In order to more effectively use amplitudes to measure rotation rate, the primary vibration needs to be controlled [113; 114]. Controlling the X vibration and measuring the Coriolis-induced Y vibration is a well known amplitude detection operation mode, and the method is modelled by applying a variable driving force in the x-direction to obtain a constant amplitude and phase for the driving vibration. Therefore, an analytical approach for controlling the primary vibration is obtained by setting the X response equal to some constant K, i.e.

$$X = K, \tag{3.4.4}$$

thereby reducing (3.1.23) to

$$X_s = \frac{K(AC - BD) + BY_s}{C}. \tag{3.4.5}$$

The driving force is then

$$X_s = \frac{K[(1-r^2-l^2)^2 - 4r^2(\zeta^2+l^2)] + jr[4\zeta(1-r^2-l^2)K - 2lY_s]}{(1-r^2-l^2) + j2\zeta r}, \tag{3.4.6}$$

with the amplitudes and phases respectively being

$$\|X_s\| = \sqrt{\frac{K[(1-r^2-l^2)^2 - 4r^2(\zeta^2+l^2)]^2 + r^2[4\zeta(1-r^2-l^2)K - 2lY_s]^2}{(1-r^2-l^2)^2 + 4\zeta^2 r^2}}, \tag{3.4.7}$$

and

$$\arg(X_s) = \arctan\left(\frac{4\zeta r(1-r^2-l^2)K - 2rlY_s}{K[(1-r^2-l^2)^2 - 4r^2(\zeta^2+l^2)]}\right) - \arctan\left(\frac{2\zeta r}{1-r^2-l^2}\right). \tag{3.4.8}$$

If expression (3.4.6) is investigated, it is observed that the driving force X_s is a function of rotation velocity l. Since l is the quantity being measured, predicting the driving force in a real device can be difficult, and is only done here analytically for illustrative purposes. In a real device it is necessary to have some control loop that controls the vibration amplitude, which is done in most MEMS gyroscopes. The x and y directions are then used as the driving and sensing directions respectively. Many amplitude based MEMS gyroscopes are based on this operation principle.

Therefore, if a force with above mentioned amplitude and phase is applied in the x-direction, the resulting system vibration response is given by

$$\begin{aligned} X &= K, \\ Y &= \frac{-2jrlK}{(1-r^2-l^2)+2j\zeta r}, \end{aligned} \tag{3.4.9}$$

giving the vibration amplitudes

$$\begin{aligned} \|X\| &= K, \\ \|Y\| &= \frac{2K\|rl\|}{\sqrt{(1-r^2-l^2)^2+4\zeta^2 r^2}}, \end{aligned} \tag{3.4.10}$$

and the phases

$$\begin{aligned} \phi &= \arg(X) = 0, \\ \varphi = \arg(Y) &= \pm\frac{\pi}{2} - \arctan\left(\frac{2\zeta r}{1-r^2-l^2}\right), \end{aligned} \tag{3.4.11}$$

where $\arg(Y)$ is observed to be the same as the phase difference $\Delta\phi$ in the uncontrolled vibration case (3.4.3).

In (3.4.10) the amplitude of vibration for the secondary direction is seen to be proportional to the primary vibration amplitude K, and rotation rate l when $1-r^2-l^2=0$. The amplitude of the Coriolis-induced secondary vibration is therefore linearly dependent on the input angular velocity l, for large and small rotation rates, making this operation mode an ideal indication of angular velocity.

The system vibration amplitude is depicted in Figure 3.8 with $X = K = 1$. The response shows a difference between the amplitude response of the system when the primary vibration amplitude is controlled, as opposed to when it is not controlled. The system has effectively been reduced to a single degree of freedom system [59]. The highest $\|Y\|$ values now occur at the new system y-direction resonance frequency, which will be close to $1-r^2-l^2=0$. Therefore the resonance frequency changes with rotation rate nonlinearly, but is only of real interest if r and l are in the order of unity. In comparing the controlled y-response depicted in Figure 3.8(b) and the uncontrolled y-response at smaller rotation rates Figure 3.4(b), both methods yield more or less the same visual result, but with different values. These differences will not be quantified here.

In the single excitation and amplitude detection mode, with controlled or uncontrolled primary vibrations, the excitation should be close to resonance, and high Q-factors (low ζ-values) should be present to obtain large enough vibrations to measure, especially at very small rotation rates. The primary excitation is usually done by exciting the proof mass into resonance by some electronic oscillation circuit designed for the purpose. Electrical equivalent circuits is typically drawn

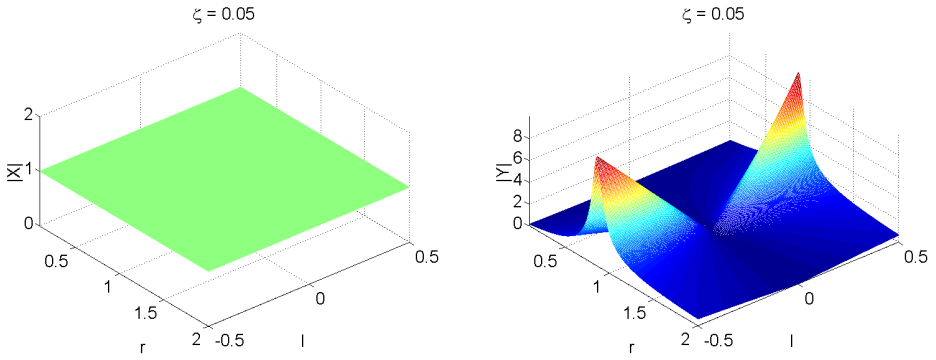

(a) $\|X\|$ (b) $\|Y\|$

Figure 3.8. Amplitude response for $X = K = 1$, $Y_s = 0$ and $\zeta = 0.05$, obtained by varying X_s.

up for the mechanical elements [59], and the applied force will not necessarily feature directly in the formulation. In MEMS the Coriolis-induced vibrations can be relatively small, even at larger rotation rates, and can easily be influenced by the driving vibration in the presence of coupling imperfections [8].

The influence of damping on the vibration amplitude of a spring-mass-damper system is usually very significant at or near resonance [105]. High Q-factors make the amplitudes of vibration spike and makes precise frequency control necessary, a problem common in MEMS gyroscope literature. Unmatched natural frequencies will change the scale factor and linearity of the response.

Various other effects have negative influences on amplitude detection gyroscopes performance. Some are easier to overcome than other [23]. The result is that, although the responses obtained are useful for illustration of the amplitude operation method, it is not necessarily sufficient for real devices. Using the coupled and asymmetrical formulations stated earlier can be useful for a first order study of the influence of mechanical imperfections on the amplitude detection modes, but is beyond the scope of this thesis.

3.4.3 Closed loop amplitude detection

A third operation mode is when a closed loop configuration is used, whereby the Coriolis induced vibration in the y-direction is nulled ($Y = 0$) by adapting Y_s using control electronics [28]. This is not a very interesting case from a mechanical dynamics point of view, since the excitation amplitude is then constant and there is no sensing vibration. There is however a sensing signal. This operation mode increases the bandwidth of the gyroscope, but decreases the signal to noise ratio, as mentioned in Section 2.2.7.1.

3.5 Dual excitation and phase detection

The phase-based operation mode is of most interest in this thesis. In the phase detection mode, both directions are driven into vibration by harmonic driving forces and the vibration phase changes are used as a measure of rotation velocity.

The concept was described by Yang *et. al* [91] in 2002, who used a vibrating beam-mass structure which induced a secondary vibration by a parasitic component of the primary vibration. It was observed that, due to an applied angular velocity, the Coriolis acceleration changed the phase of the secondary vibration. The experimentally measured phase change was larger than the theoretically expected values and Yang *et. al* mentioned that further investigation was needed. They proposed that the error may have been caused by the instability of the parasitic driving component.

Another reason for the phase underestimation, less obvious and not mentioned by Yang *et. al*, may be that more attention should be given to the effect of the additional driving force in the theoretical prediction. The model that has been developed here describes the equations of motion and the system response of the two-dimensionally excited 2-DOF system more comprehensively, and is now used to explore the phase-based operation method.

3.5.1 Equal excitation forces

When both directions are excited with a periodic force, X_s and Y_s have a finite, constant value. For simplicity, take $X_s = Y_s = 1$. The vibration amplitudes follow from the general system amplitude response (3.3.2), and are given as

$$\begin{aligned} \|X\| &= \sqrt{\frac{(1-r^2-l^2)^2+4r^2(\zeta+l)^2}{[(1-r^2-l^2)^2-4r^2(\zeta^2+l^2)]^2+16r^2[\zeta(1-r^2-l^2)]^2}}, \\ \|Y\| &= \sqrt{\frac{(1-r^2-l^2)^2+4r^2(\zeta-l)^2}{[(1-r^2-l^2)^2-4r^2(\zeta^2+l^2)]^2+16r^2[\zeta(1-r^2-l^2)]^2}}, \end{aligned} \tag{3.5.1}$$

and are depicted in Figure 3.9. The amplitudes of vibration can be seen to be similar to that of the one-dimensionally forced uncontrolled vibration case (Fig. 3.3), although both vibration amplitudes are now a weak function of rotation rate.

Using (3.3.3) and $X_s = Y_s = 1$, the phases are depicted in Figure 3.11, and given as

$$\begin{aligned} \arg(X) = \phi &= \arctan\left(\frac{2r(\zeta+l)}{1-r^2-l^2}\right) - \arctan\left(\frac{4\zeta r(1-r^2-l^2)}{(1-r^2-l^2)^2-4r^2(\zeta^2+l^2)}\right), \\ \arg(Y) = \varphi &= \arctan\left(\frac{2r(\zeta-l)}{1-r^2-l^2}\right) - \arctan\left(\frac{4\zeta r(1-r^2-l^2)}{(1-r^2-l^2)^2-4r^2(\zeta^2+l^2)}\right). \end{aligned} \tag{3.5.2}$$

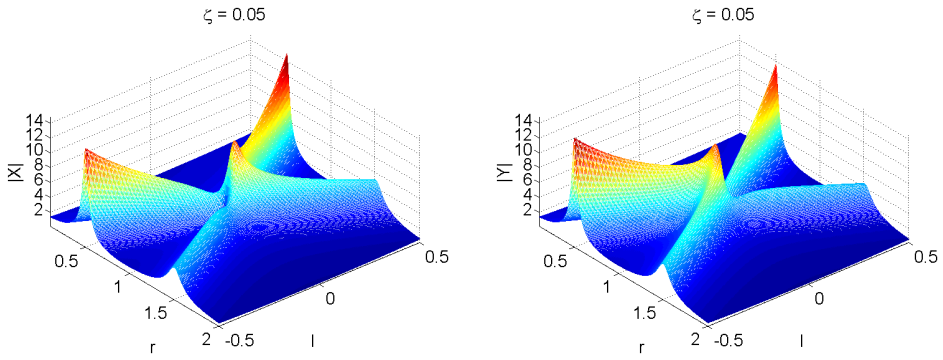

(a) $\|X\|$ (b) $\|Y\|$

Figure 3.9. Amplitude response for $X_s = 1$, $Y_s = 1$ and $\zeta = 0.05$

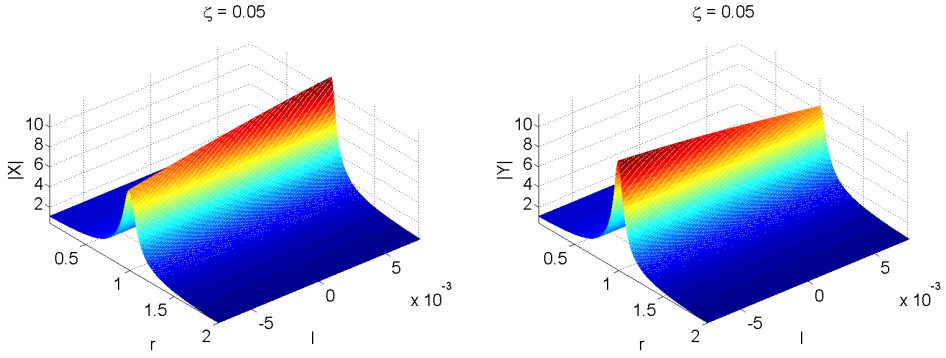

(a) $\|X\|$ (b) $\|Y\|$

Figure 3.10. Small rotation rate amplitude response for $X_s = 1$, $Y_s = 1$ and $\zeta = 0.05$

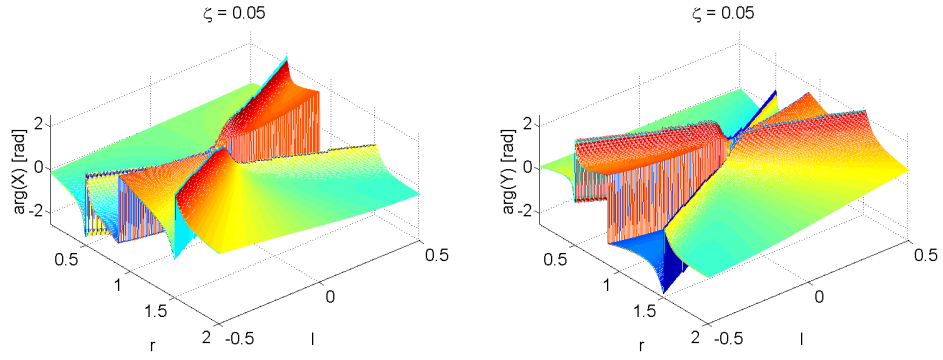

(a) $\arg(X) = \phi$ (b) $\arg(Y) = \varphi$

Figure 3.11. Phase response for $X_s = 1$, $Y_s = 1$ and $\zeta = 0.05$

The phase difference shown in Figure 3.12 is obtained from (3.3.6) and is given as

$$\Delta\phi = \varphi - \phi = \arctan\left(\frac{-4rl(1-r^2-l^2)}{(1-r^2-l^2)^2 + 4r^2[\zeta^2 - l^2]}\right). \tag{3.5.3}$$

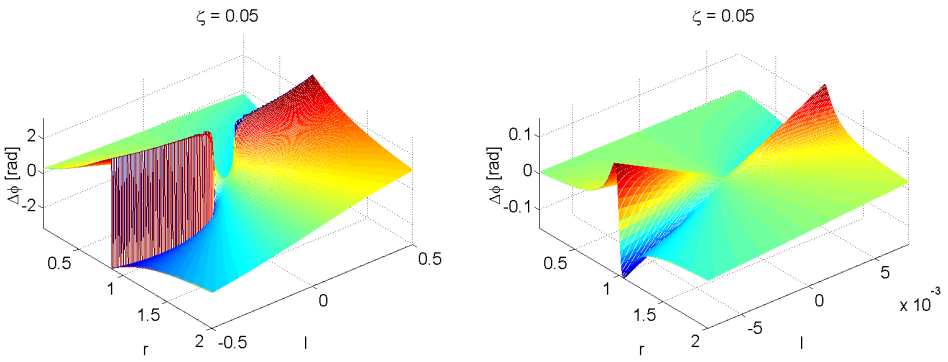

(a) $\Delta\phi$ (b) $\Delta\phi$ for small rotation rates

Figure 3.12. Phase difference $\Delta\phi$ for $X_s = 1$, $Y_s = 1$ and $\zeta = 0.05$

From (3.5.3) and Figure 3.12 it is observed that the phase difference $\Delta\phi$ is now a function of the input angular velocity l, the driving frequency r and damping ratio ζ. The response has mostly a smooth slope with respect to l, making the phase difference an indication of rotation rate, even though no vibrations are controlled. The phase difference does not have the same discontinuity at $l = 0$ as with the amplitude detection method, but it does have other jump discontinuities that are dependant on l, r and ζ.

Just like the one dimensional excitation case, the phase difference is used instead of the individual phases to clear the obstacle of excessive phase jump discontinuities. The phase difference formulation effectively cancels out the wrap-around phase segments and nullifies the need for phase unwrapping. It has, however, the effect of doubling the phase jumps that occur in the same direction. In defining the phase difference, an additional advantage may be that no additional signal is needed, since the phases are referenced with respect to each other (as mentioned before).

An interesting observation is that the phase difference in the dual forcing symmetrical configuration (3.5.3) corresponds closely to the symmetric phase difference defined by John *et. al* [90] with the exception of a few terms, although he used a vibrating beam mass structure with two strategically located piezoresistive sensing elements. John derived his equations specifically for his beam with a mass at the end of it, but did not consider a general model as done here. He used one-dimensional excitation and derived the expressions for induced phase differences between sensor signals due to induced stresses.

A notion worth mentioning, is that his method of phase difference detection of sensor stress due to one-dimensional forcing and applied angular rate is equivalent to dual forcing in a transformed local coordinate frame, thereby explaining the similarities to this model. However, the formulation presented in this thesis describes the general case of a 2-DOF system and is independent of the beam-mass structure, beam stresses and sensor positions, and can be used to describe

other configurations as well.

Note that if both directions are excited into resonance, there will occur a frequency lock-in effect that depends on the amount of electromechanical coupling in the system which can be modelled by coupled Van der Pol oscillators [88]. Since the derived model is ideal and purely mechanical with no nonlinear coupling, it does not predict this resonance excitation lock-in effect. If frequency lock-in occurs, the phase relationship may be destroyed. These effects need further investigation if resonance excitation is to be used. Therefore, if the phase detection method is used, both directions may need to be excited harmonically by sinusoidal applied forces and not by oscillator resonance excitation, except if it is well understood and the lock-in effect is overcome.

3.5.2 Unequal excitation forces

The phase dependence of a symmetrical system with equal excitation forces has been illustrated in Section 3.5.1, but a few interesting observations can be made when using unequal excitation forces. In investigating unequal excitation forces, different values of X_s and Y_s are used, making it useful to introduce a forcing ratio f, which is defined as

$$f = \frac{Y_s}{X_s}, \tag{3.5.4}$$

or $Y_s = fX_s$. Using the forcing ratio f with the general symmetrical system response given in (3.3.2), the magnitudes are now obtained as

$$\begin{aligned} \|X\| &= X_s \sqrt{\frac{(1-r^2-l^2)^2 + 4r^2(\zeta + lf)^2}{[(1-r^2-l^2)^2 - 4r^2(\zeta^2+l^2)]^2 + 16r^2[\zeta(1-r^2-l^2)]^2}}, \\ \|Y\| &= X_s \sqrt{\frac{(1-r^2-l^2)^2 f^2 + 4r^2(\zeta f - l)^2}{[(1-r^2-l^2)^2 - 4r^2(\zeta^2+l^2)]^2 + 16r^2[\zeta(1-r^2-l^2)]^2}}, \end{aligned} \tag{3.5.5}$$

and from (3.3.3), the phases are now

$$\begin{aligned} \arg(X) = \phi &= \arctan\left(\frac{2r(\zeta + lf)}{(1-r^2-l^2)X_s}\right) - \arctan\left(\frac{4\zeta r(1-r^2-l^2)}{(1-r^2-l^2)^2 - 4r^2(\zeta^2+l^2)}\right), \\ \arg(Y) = \varphi &= \arctan\left(\frac{2r(\zeta f - l)}{(1-r^2-l^2)f}\right) - \arctan\left(\frac{4\zeta r(1-r^2-l^2)}{(1-r^2-l^2)^2 - 4r^2(\zeta^2+l^2)}\right). \end{aligned} \tag{3.5.6}$$

The phase difference between X and Y is then

$$\Delta\phi = \varphi - \phi = \arctan\left(\frac{-2rl(1-r^2-l^2)(1+f^2)}{f(1-r^2-l^2)^2 + 4r^2(\zeta + lf)(\zeta f - l)}\right). \tag{3.5.7}$$

Consider the above mentioned amplitude and phase responses: if $f = 0$, only the x-direction is forced and the system functions as an amplitude-based measure

of angular velocity. On the other hand, if $f = 1$, both directions are equally forced and the system functions as a phase-based measure of angular velocity. To illustrate how the system reacts for forcing ratios between zero and unity, $\|X\|$, $\|Y\|$ and $\Delta\phi$ are plotted in Figures 3.13-3.17 for a range of values for f from 0.01 to 100.

If f is small, Y_s is negligible, making the y-amplitude an indication of rotation rate, as depicted in Figure 3.13. With a slightly larger f, the system y-amplitude and the phase difference is an indication of rotation rate. However, the amplitude shifts a little, and there are pronounced nonlinearities in the phase difference with respect to l, as depicted in Figure 3.14. With $f = 1$, the phase difference nonlinearities are at a minimum, but both amplitude responses don't seem that useful. With $f = 10$, the amplitude and phase difference is similar to that of $f = 0.1$, but with $\|X\|$ instead $\|Y\|$ being a useful function of rotation rate. Similarly, $f = 100$, as in Figure 3.17, is again mostly useful as an amplitude-based measurement system.

Another observation made from the phase differences depicted in Figures 3.14 and 3.16 ($f = 0.1$ and $f = 10$), is that the non-linearities for a specific value of r, have a higher gradient with respect to l at low l-values, than opposed to higher l-values. At higher values of l the gradient smooths out, making $\Delta\phi$ a weak indication of rotation rate. In truth, the phase difference $\Delta\phi$ has a distinct arctan shape with respect to l, as expected. Therefore, if different amplitudes for excitation forces are used, the gradient $\frac{\partial\Delta\phi}{l}$ is enlarged by an increased ratio between the forces, but at the cost of the linearity being decreased.

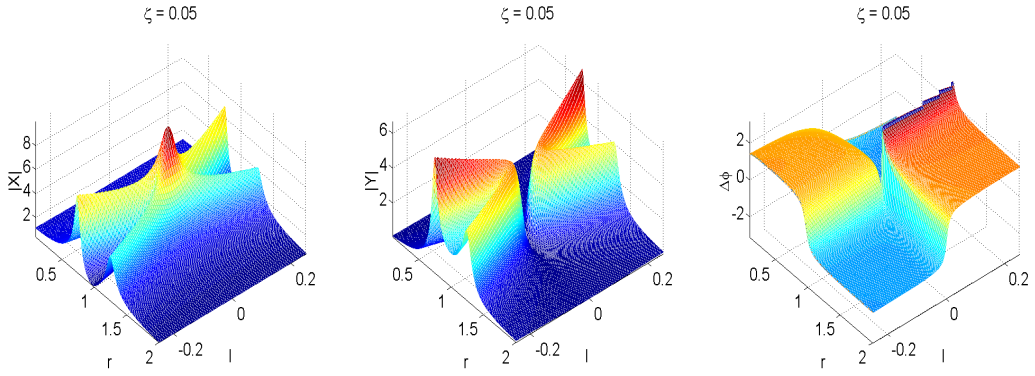

Figure 3.13. $f = 0.01$, amplitude-based

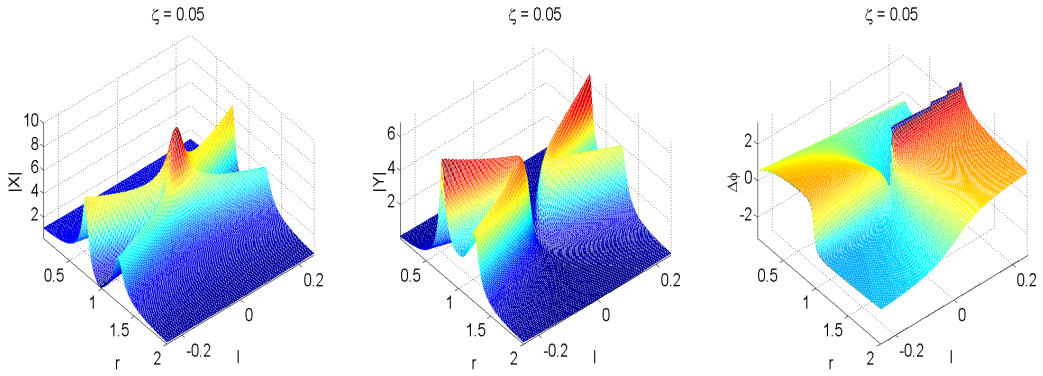

Figure 3.14. $f = 0.1$, amplitude and phase-based

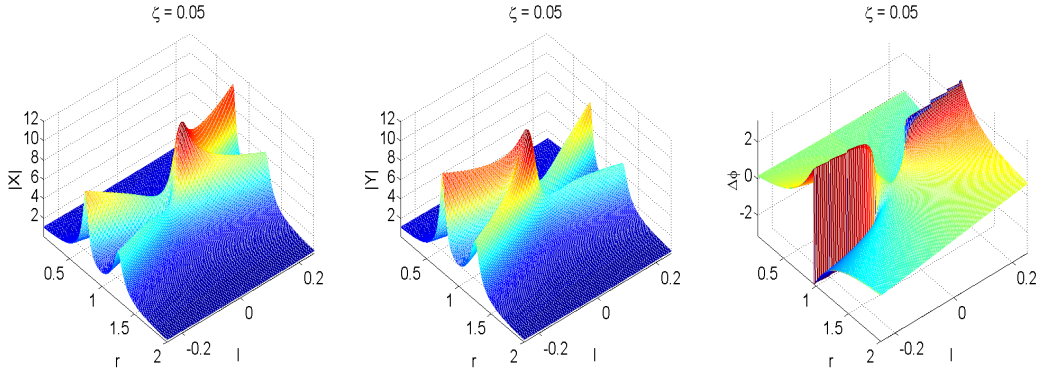

Figure 3.15. $f = 1$, phase-based

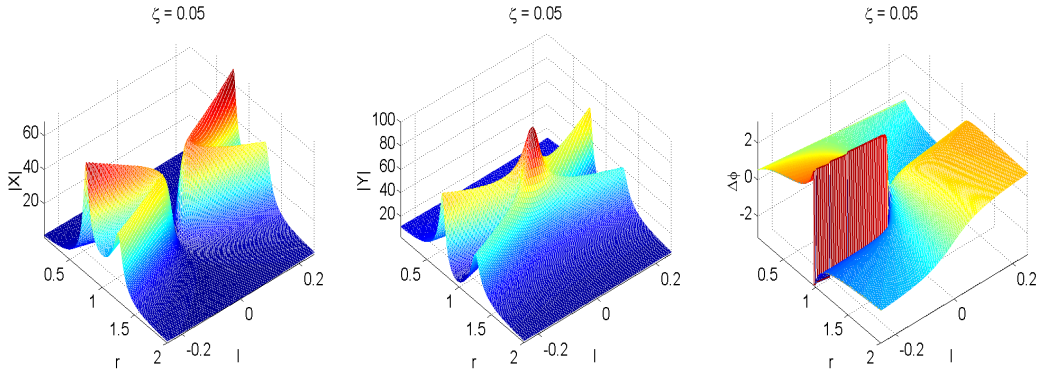

Figure 3.16. $f = 10$, amplitude and phase-based

3.6 Phase-based operation dependence on damping

The system response due to different damping ratios (ζ) is now also investigated for equal excitation forces ($f = 1$). This should give insight into the systems de-

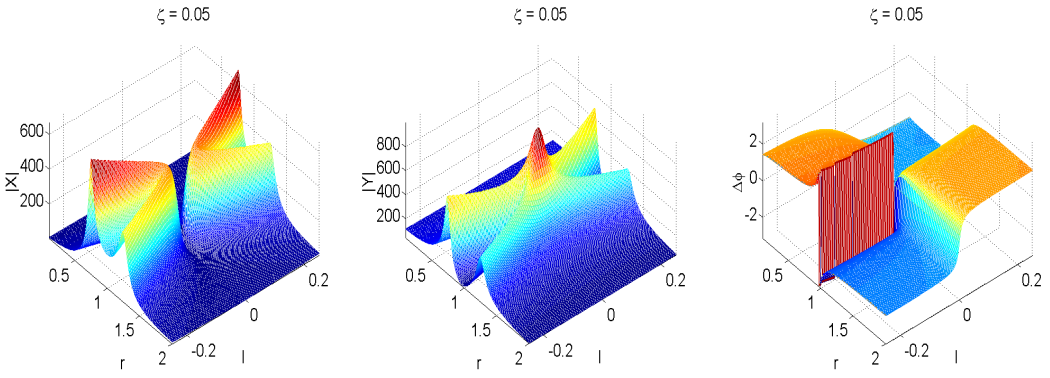

Figure 3.17. $f = 100$, amplitude-based

pendence on damping. A general range of damping values are considered, but special attention is given to the damping values expected in MEMS.

The order of magnitude of quality factors found in MEMS devices have a wide range and can be as low as five [59], or in excess of 10000 in a vacuum [115]. These values are usually obtained at resonance [101] and depend on various electromechanical and fluidic effects [116]. High quality factors correspond to low damping ratios[7], which may possibly imply an insensitivity of the phase difference to damping ratios in the range expected in MEMS gyroscopes. Figures 3.18 to 3.20 show a two-dimensional representation of the system response for a range of damping ratio values $0 < \zeta < 1$ (or $0.5 < Q < \infty$), to illustrate the effect of damping. The damping ratio ranges expected in MEMS devices, namely $0 < \zeta < 0.5$ (or $1 < Q < \infty$), are shown in another color and correspond to larger amplitudes. Each row of figures depict a different excitation frequency r.

For comparison, 3-D plots of different damping ratio values are also shown in Figures 3.21 to 3.27, with the amplitudes given in decibel (dB) for ease of visualization.

The minimum amplitudes of vibration $|X|$ and $|Y|$ are important in considering minimum measurable vibrations and are, for the most part, a welcome result. The amplitudes in Figures 3.18 to 3.20 are mostly larger than about a third of the value of the driving force amplitudes at r-values not close to unity. The minimum amplitudes of vibration, especially at the low MEMS damping ratios, have a non-zero lower limit at driving frequencies away from $r = 1$, even at small rotation rates.

This means that the minimum measurable amplitude will be dependant on the size of the driving forces, making operation at resonance unnecessary if damping is not too high, and if suitable driving frequencies are used. Signal to noise ratio problems due to small vibration amplitudes, which are especially problematic in the single excitation and amplitude detection mode at low rotation rates, are

[7] Since $Q = \frac{1}{2\zeta}$.

therefore effectively eliminated. However, at very high driving frequencies (high values of r), this advantage may be lost and the measurable phase difference by the electronics still has to be accounted for if only phase is used as an indication of rotation rate. Note that there are dead spots in $|X|$ and $|Y|$ close to the defined natural frequency ($r = 1$), when the damping ratio ζ is equal to the normalized rotation rates $-l$ and $+l$ respectively. These spots are actually present because of the "shifted" amplitude response due to the Coriolis coupling in the dual excitation mode. The dead spots may be eliminated if $X_s \neq Y_s$ or by choosing $r_1 \neq r_2$, but this implicates an asymmetrical system.

The phases $\arg(X)$ and $\arg(Y)$ are observed to be functions of normalized rotation rate l (shown only in the 2-D plots), illustrating the effect of angular velocity on the phase of the dual forced system for different damping ratios. Jump discontinuities are visible in the phase response. The phase difference $\Delta\phi$ shows a smooth response for r-values above unity, but it has discontinuities below $r = 1$. The phase difference response has approximate linear regions which shows that the phase difference between the vibrations in the dual forcing configuration can be used as a measurement of angular velocity. In implementing the concept, a play-off between linearity and range of measurement will have to made, as with most transducers.

Damping ratios in the ranges expected in MEMS devices do not affect the phase difference significantly, because of the relatively small corresponding ζ-values. The insensitivity to damping values in the mentioned ranges is a positive result in the drive to make a sensor that is insensitive to environmental effects. At r-values close to unity, damping is seen to have a larger effect on the phase difference than further away from $r = 1$.

The result is that, in the dual excitation and phase difference operation mode, driving frequencies close to $r = 1$ may have to be avoided at certain normalized rotation rates, since

1. the phase difference is not a smooth function of rotation rate at $r = 1$ and there are jump discontinuities present,
2. there are phase difference nonlinearities with respect to l at r-values close to unity,
3. the phases are more dependant on damping close to $r = 1$
4. there are dead spots in the amplitude response at $r = 1$ when $\zeta = |l|$.

Note that these observations are made over a wide range of rotation rates. In the operating ranges of specific devices, some of these effects may not be prominent. Excitation frequencies below $r = 1$ can be used over certain operating ranges, but then care should be taken to avoid the jump discontinuities that moves closer to $l = 0$ as the excitation frequency ratio gets closer to unity.

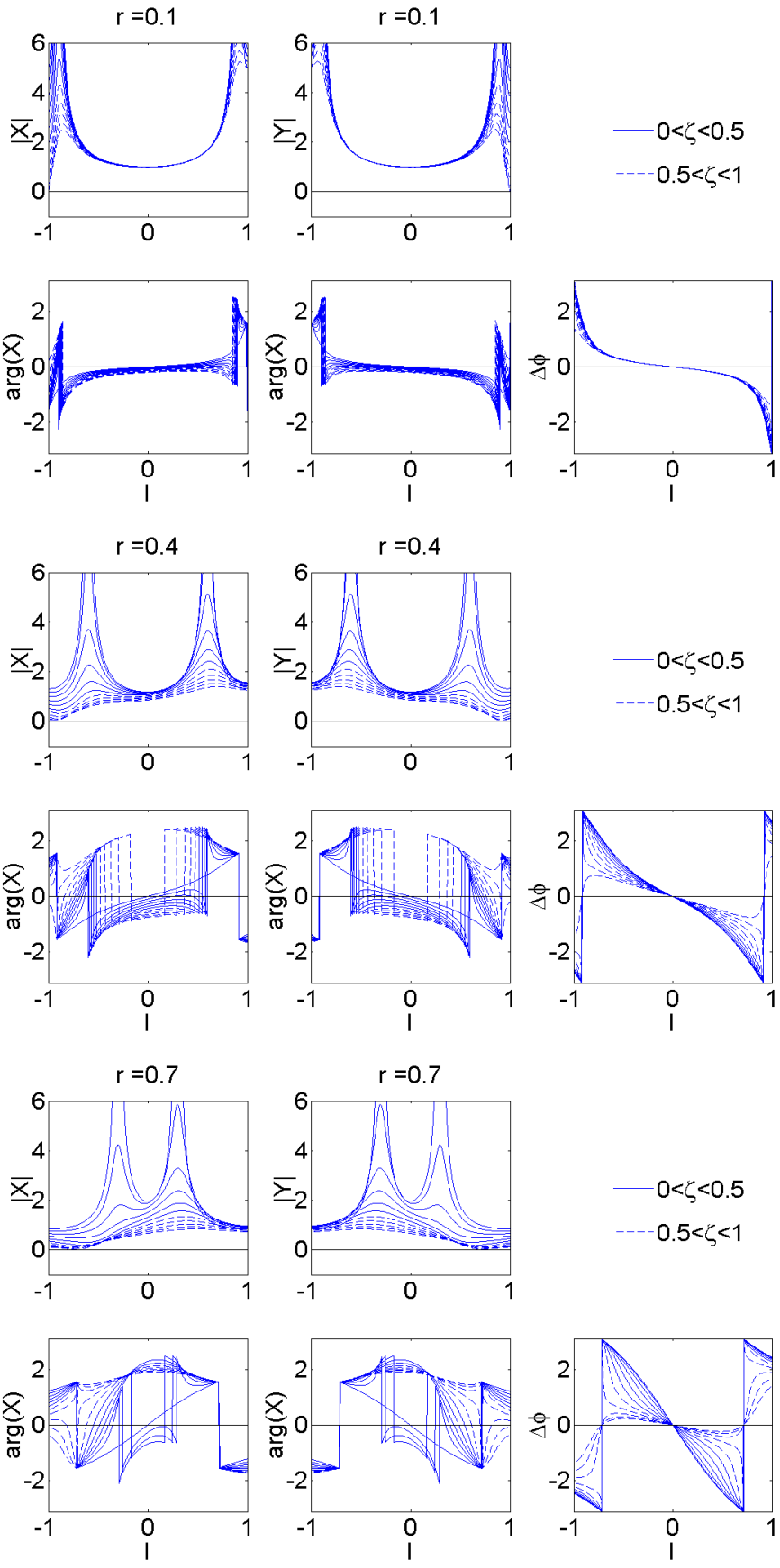

Figure 3.18. Responses for $\zeta = 0$ to 1, $r = 0.1, 0.4$ and 0.7, with $X_s = 1$, $Y_s = 1$

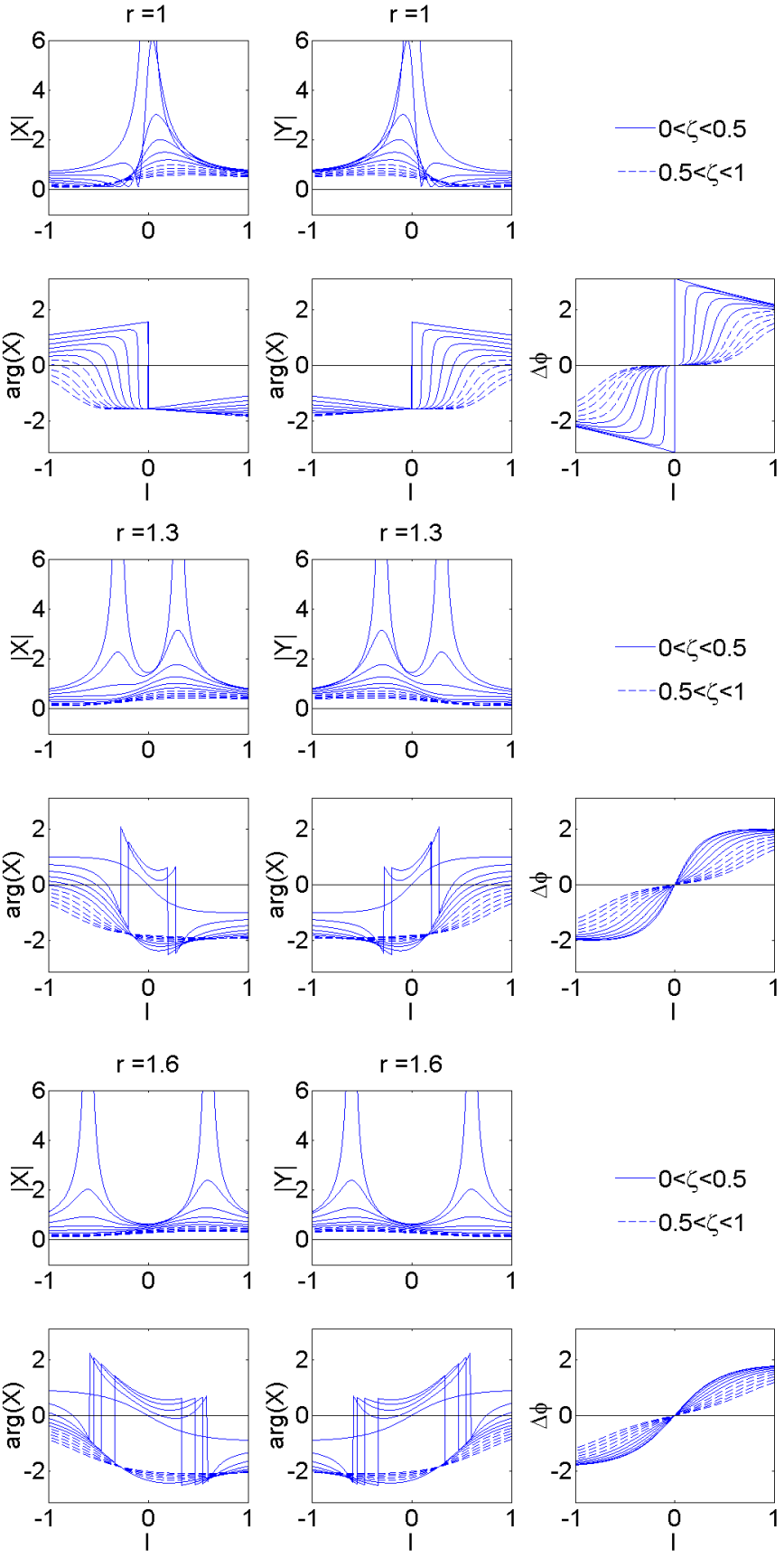

Figure 3.19. Responses for $\zeta = 0$ to 1, $r = 1, 1.3$ and 1.6, with $X_s = 1$, $Y_s = 1$

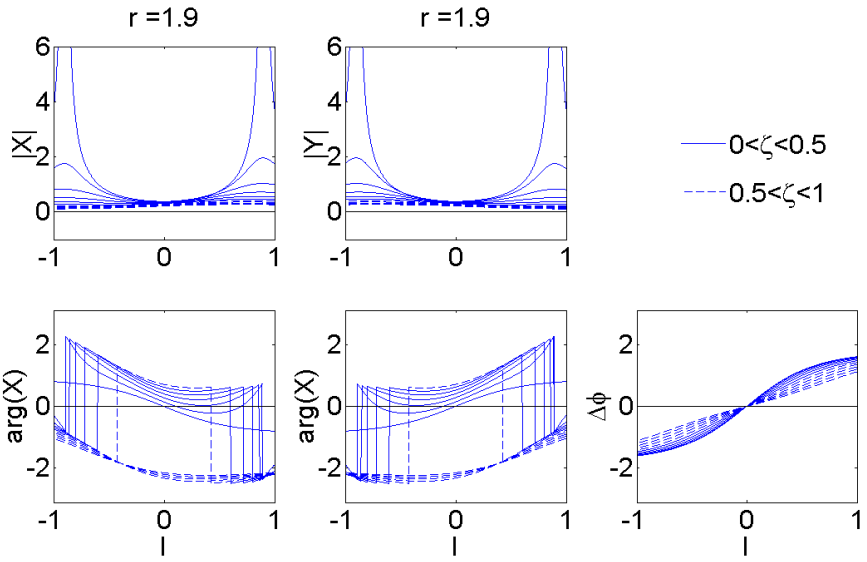

Figure 3.20. Response for $\zeta = 0$ to 1, $r = 1.9$, with $X_s = 1$, $Y_s = 1$

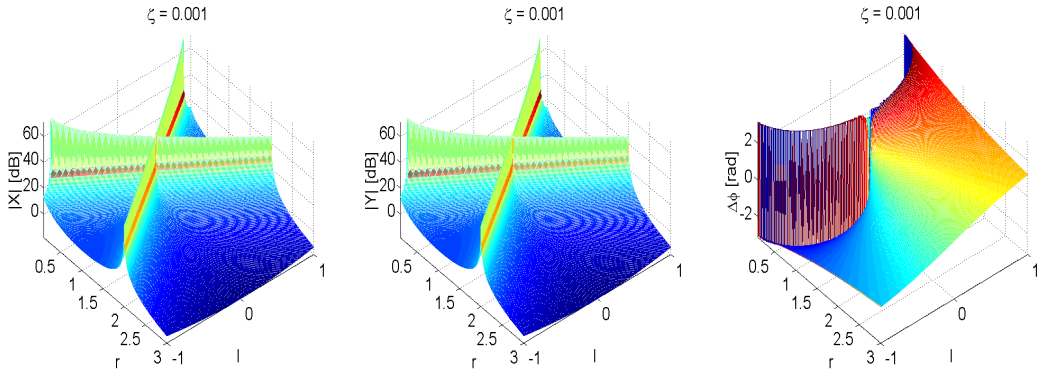

Figure 3.21. $\zeta = 0.001$

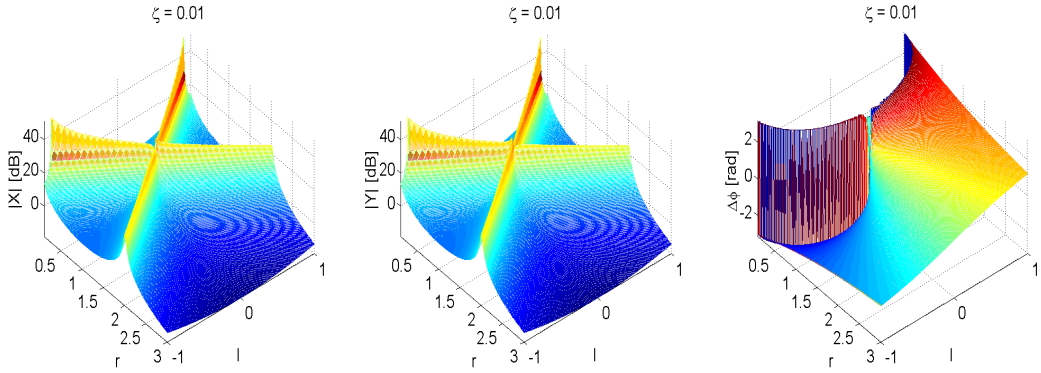

Figure 3.22. $\zeta = 0.01$

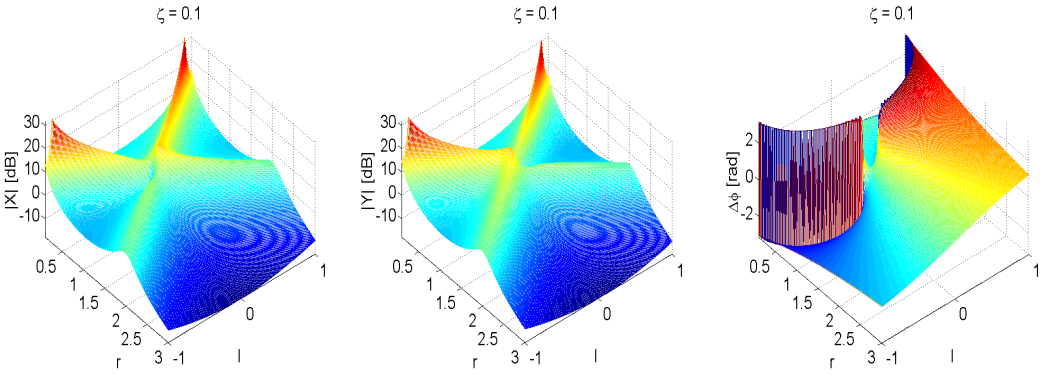

Figure 3.23. $\zeta = 0.1$

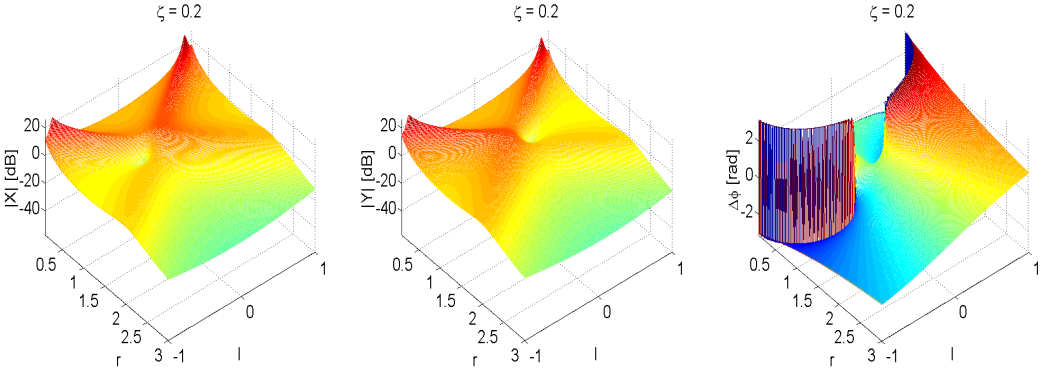

Figure 3.24. $\zeta = 0.2$

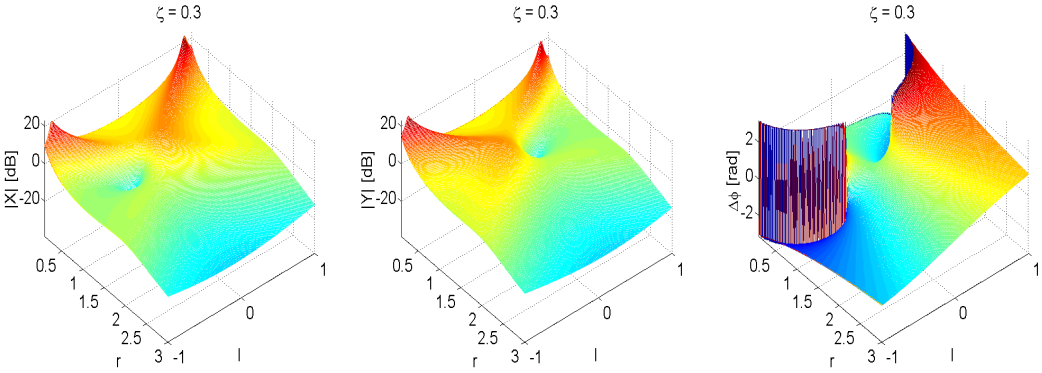

Figure 3.25. $\zeta = 0.3$

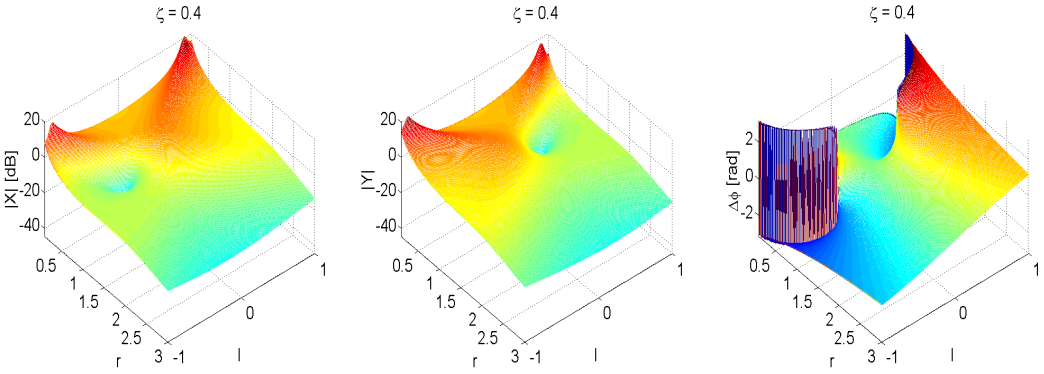

Figure 3.26. $\zeta = 0.4$

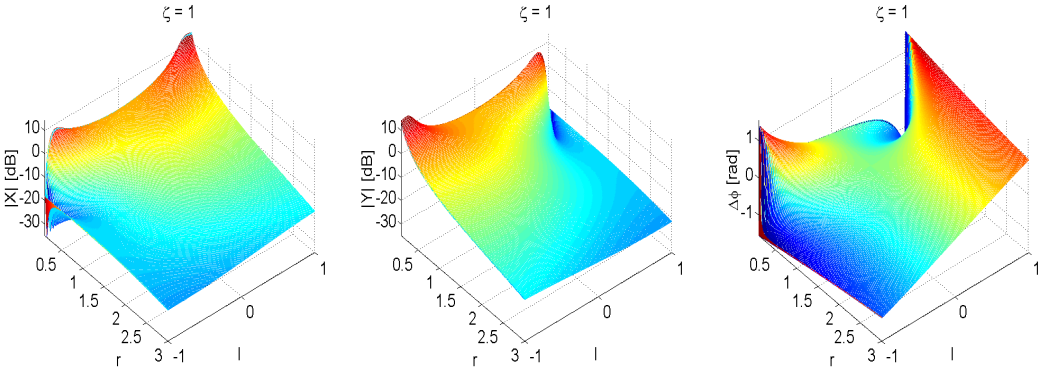

Figure 3.27. $\zeta = 1$

Chapter

4

Numerical Modelling

In the previous chapter, the analytical model of the 2-DOF spring-mass-damper system with an applied rotation rate has been established. In this chapter, the differential equations are now solved numerically in order to verify the analytical derivation. A time-variant solution is also implemented using Simulink and the displacement of the proof mass is analyzed. Only a limited investigation of the system transient response is made.

4.1 State space representation of the equations of motion

In order to solve the system response numerically, the equations of motion are transformed into the state space form. The system of differential equations describing the 2-DOF spring-mass-damper system is reduced to a first order system, which can be solved numerically with relative ease. More specifically, the original second order system of equations is rewritten into a first order system with twice as many variables. In order to facilitate the transformation, the system of equations of motion (3.1.7) are rearranged to isolate the second derivative of displacement $\ddot{x}$, giving

$$\begin{aligned} \ddot{x} &= \frac{F_1}{m} - 2\zeta_1\omega_{n1}\dot{x} - (\omega_{n1}^2 - \Omega^2)x + 2\Omega\dot{y}, \\ \ddot{y} &= \frac{F_2}{m} - 2\zeta_2\omega_{n2}\dot{y} - (\omega_{n2}^2 - \Omega^2)y - 2\Omega\dot{x}. \end{aligned} \tag{4.1.1}$$

The transformation into the state space is obtained by introducing the state vari-

ables $\vec{\mathrm{x}} = \{x_1, x_2, x_3, x_3\}^T$, where

$$\begin{aligned} x_1 &= x, \\ x_2 &= y, \\ x_3 = \dot{x_1} &= \dot{x}, \\ x_4 = \dot{x_2} &= \dot{y}. \end{aligned} \tag{4.1.2}$$

The state variables are then introduced into the state equations, which usually have the form [117]

$$\begin{aligned} \dot{\vec{\mathrm{x}}} &= [\mathrm{A}]\vec{\mathrm{x}} + [\mathrm{B}]\vec{\mathrm{u}}, \\ \vec{\mathrm{y}} &= [\mathrm{C}]\vec{\mathrm{x}}. \end{aligned} \tag{4.1.3}$$

Here, $\dot{\vec{\mathrm{x}}} = \{\dot{x_1}, \dot{x_2}, \dot{x_3}, \dot{x_3}\}^T$ and [A], [B] and [C] are the state, input and output matrices respectively. $\vec{\mathrm{u}}$ is a vector containing the system inputs and $\vec{\mathrm{y}}$ is the system output. Using the state space formulation, (4.1.1) is transformed into

$$\begin{Bmatrix} \dot{x_1} \\ \dot{x_2} \\ \dot{x_3} \\ \dot{x_4} \end{Bmatrix} = \begin{bmatrix} 0 & 0 & 1 & 0 \\ 0 & 0 & 0 & 1 \\ \Omega^2 - \omega_{n1}^2 & 0 & 2\zeta_1\omega_{n1} & -2\Omega \\ 0 & \Omega^2 - \omega_{n2}^2 & -2\Omega & 2\zeta_1\omega_{n1} \end{bmatrix} \begin{Bmatrix} x_1 \\ x_2 \\ x_3 \\ x_4 \end{Bmatrix} + \begin{bmatrix} 0 & 0 \\ 0 & 0 \\ \frac{1}{m} & 0 \\ 0 & \frac{1}{m} \end{bmatrix} \begin{Bmatrix} F_1 \\ F_2 \end{Bmatrix}. \tag{4.1.4}$$

The state, input and output matrices are then used as input parameters in the Matlab Control System Toolbox function `ss`, which assembles a state space model and selects the state variables automatically. The state space model is created with the Matlab code given in Appendix B.2, and can be used for a variety of numerical simulations in Matlab. The numerical simulation applicable here, is determination of the system amplitude and phase response as a function of the input frequency for a range of different rotation rates, i.e. the frequency response. The Matlab `bode` function is used to determine the frequency response at a specific rotation rate, and is invoked by the statement

```
[mag,phase]=bode(mdk,w);
```

with `mdk` being the state space system, `w` the user-defined input frequency range and `mag` and `phase` the frequency response magnitudes and phases corresponding to the given input frequencies. The response vectors of different rotation rates are inserted into a response matrix, with each row representing the frequency response at a specific rotation rate Ω. System parameters of unity are used and different plots are made to compare the analytical and numerical solution methods. Surface plots of the state space response are depicted in Figures 4.1 and 4.2.

The surface plots of the numerical response are observed to be the same as those of the analytical solution, depicted in Figures 3.9 and 3.12 in Section 3.5. Note

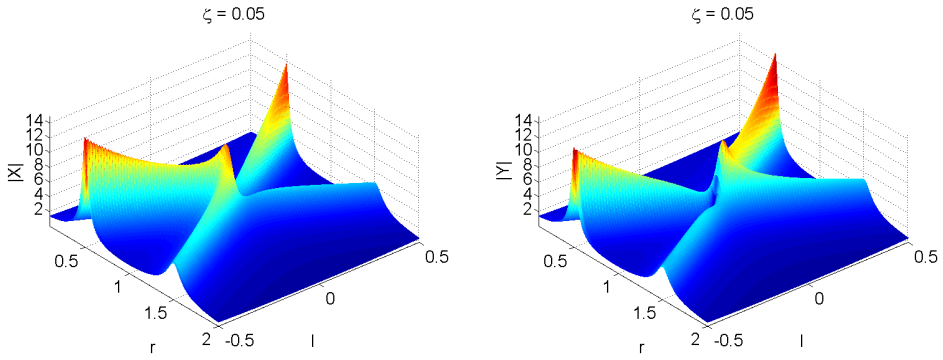

(a) $\|X\|$ (b) $\|Y\|$

Figure 4.1. State space amplitude response for $X_s = 1$, $Y_s = 1$ and $\zeta = 0.05$

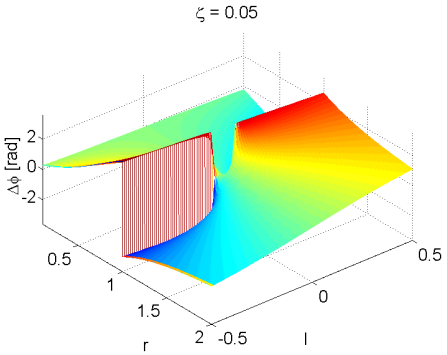

Figure 4.2. State space phase difference for $X_s = 1$, $Y_s = 1$ and $\zeta = 0.05$

however, that certain sections of the phase response are wrapped with full circle jumps to correspond with the analytical wrapped response. The phases can be wrapped or unwrapped in a variety of ways (not shown), but are all equivalent, due to full-circle phase jumps. Only the amplitudes and phase differences are depicted, since keeping track of individual phase jumps in both $\arg(X)$ and $\arg(Y)$ needlessly complicate the visual comparison.

To confirm the analytical model, the state space response is determined at discrete rotation rate values and compared to the continuous response of the analytical model. The comparison of the amplitudes and phase differences are depicted in Figures 4.3 and 4.4 for random damping values. The analytical model and the numerical solution are seen to predict exactly the same response, reasserting the analytical model.

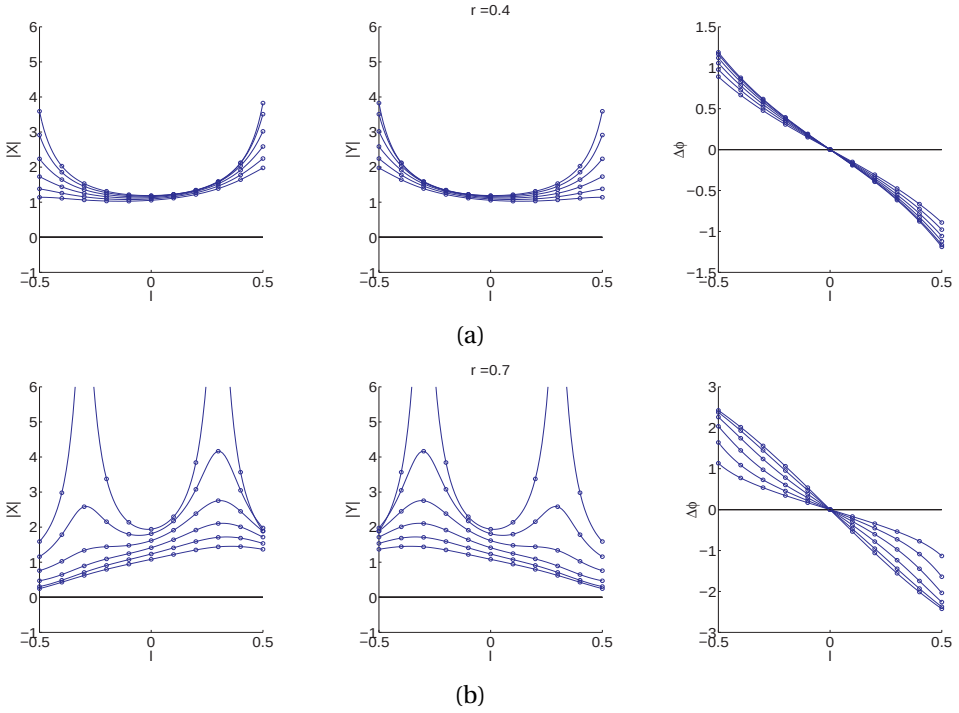

Figure 4.3. Selected responses from mathematical (-) and state space (o) models

4.2 Time-variant simulation using Simulink

The preceding sections show the steady state frequency and rotation velocity response, but a time-variant analysis is now implemented to study the system transient response. Due to time and scope constraints a complete analysis is not performed, but the infrastructure is developed for future use in follow-up studies. Matlab Simulink is used for the transient simulation.

By again using the equations of motion with the acceleration terms isolated, as in the previous section, the Simulink model is constructed by adding and connecting blocks corresponding to each of the terms in (4.1.1). The schematic of the model is depicted in Figure 4.5 and the descriptions of the elements are given next to each block. Starting with sinusoidal excitation forcing signals $\frac{F_x}{m}$ and $\frac{F_y}{m}$, the relevant signals are integrated with $\frac{1}{s}$, transmitted by the connecting lines, multiplied by gains K and added or subtracted. The two rows of blocks on the right-hand side of the figure are used for various types of outputs.

When all the transient effects have disappeared, the remaining steady state response should be the same as the response predicted by the steady state model, and is used as a rudimentary check to see if there are no major errors in the Simulink model. The steady state amplitude and phase are extracted with the modified averaged spectrum analyzer, which uses a Fourier transform based func-

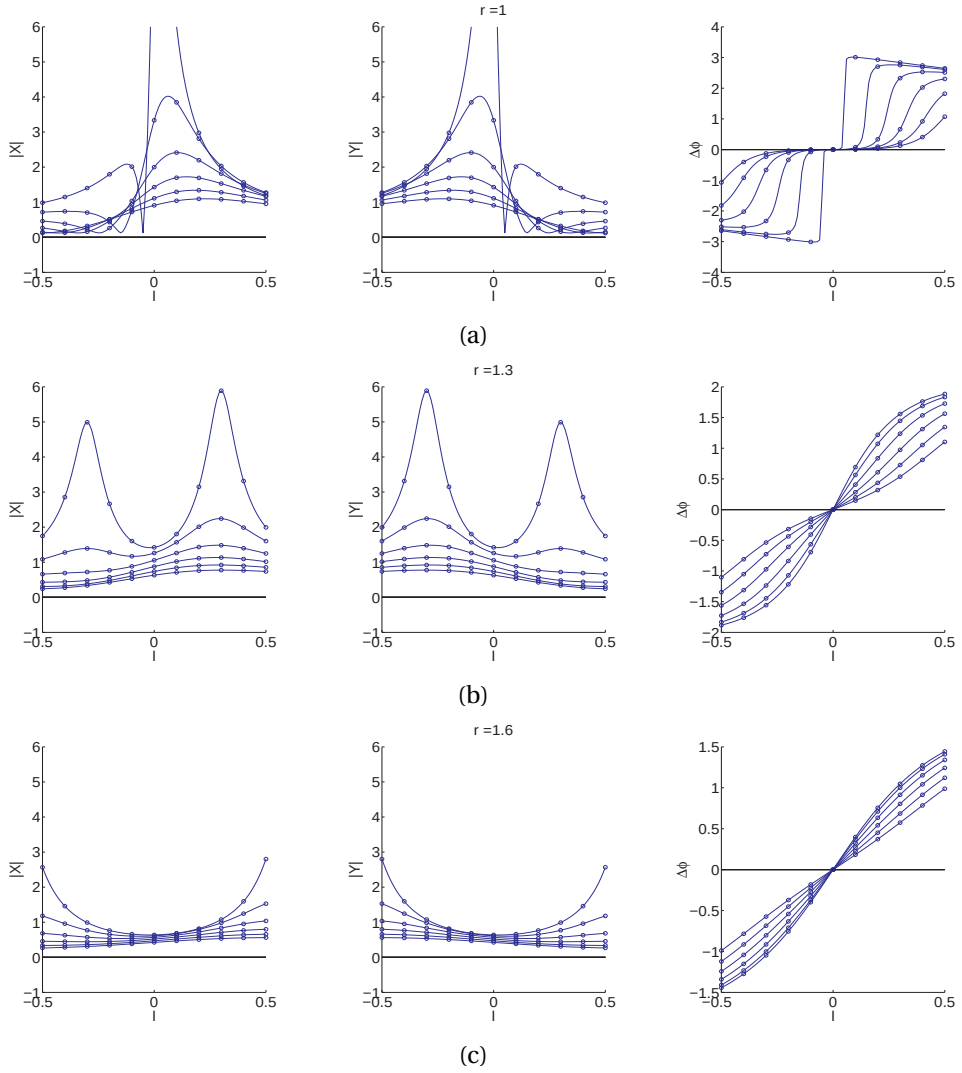

Figure 4.4. Selected responses from mathematical (-) and state space (o) models

tion [118] of the time-based signal. The analytical and Simulink responses are compared for a single value of $\zeta = 0.1$ and a range of r-values, and are depicted in Figures 4.6 and 4.7.

Most of the Simulink and analytical solution data points coincide, with the exception of a few. These outlier data points can possibly be attributed to one of two main reasons, being: a) not all the transient effects have disappeared or, b) the method of extracting the phases from the time-dependent steady state signals is not robust enough. However the case may be, studying this effect further is not a priority in this thesis.

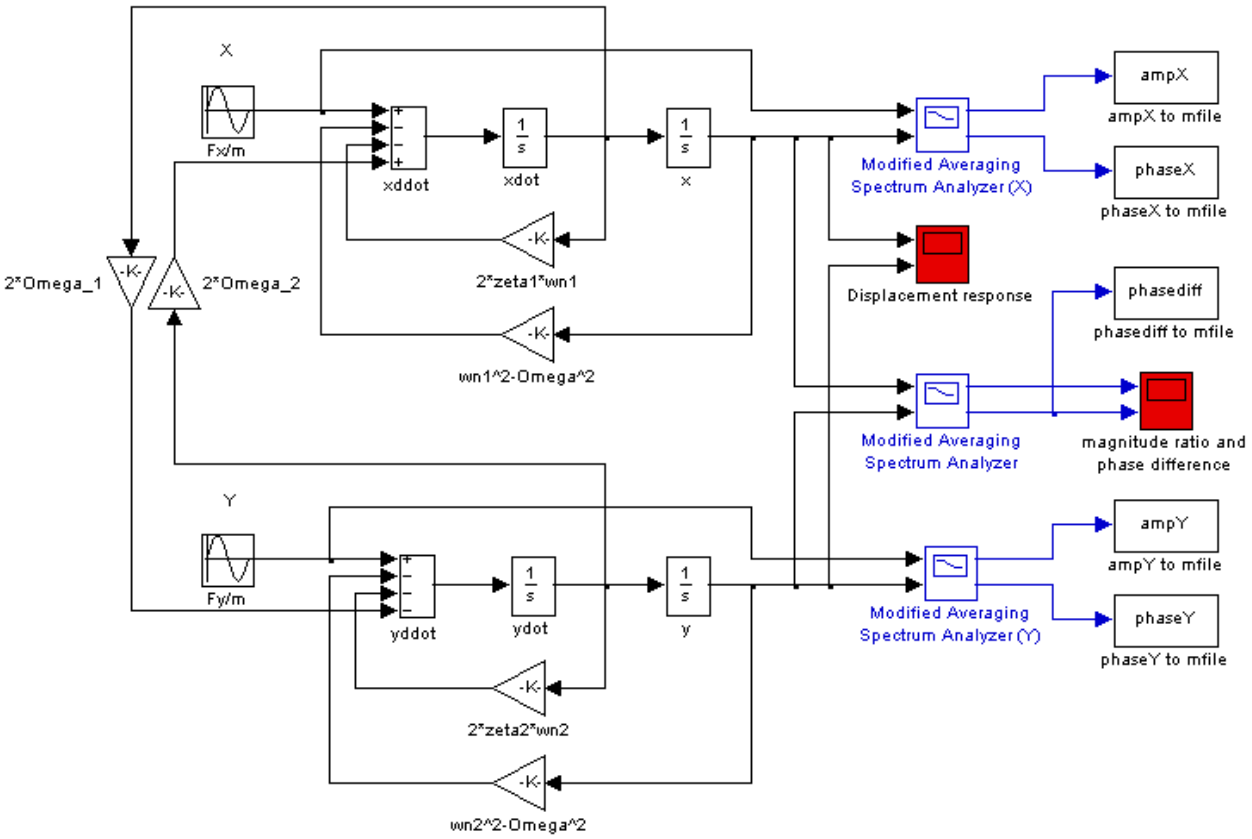

Figure 4.5. Simulink model of a 2-DOF spring-mass-damper system

4.3 Transient vibration amplitude and phase

With the system steady state response established, the system transient response for a single excitation frequency is now presented to illustrate the vibrational behaviour of the proof mass. Consider a harmonic oscillation in two-dimensional space. That is, if a point is displaced sinusoidally with equal frequencies in two dimensions, the point coordinates x and y at a time t are given by

$$\begin{aligned} x &= M_x \sin(\omega t + \theta_0), \\ y &= M_y \sin(\omega t + \theta_0 + \beta), \end{aligned} \tag{4.3.1}$$

where M_x and M_y are the magnitudes, ω the frequency and θ_0 the initial phase of the displacements. If the phase difference between the two vibrations is zero (i.e. $\beta = 0$), the vibrations occur in a straight line slanted at 45°. With a phase difference between the vibrations, the straight line becomes an ellipse, which becomes a circle for $\beta = \frac{\pi}{2}$. With β increased further, the vibration will again

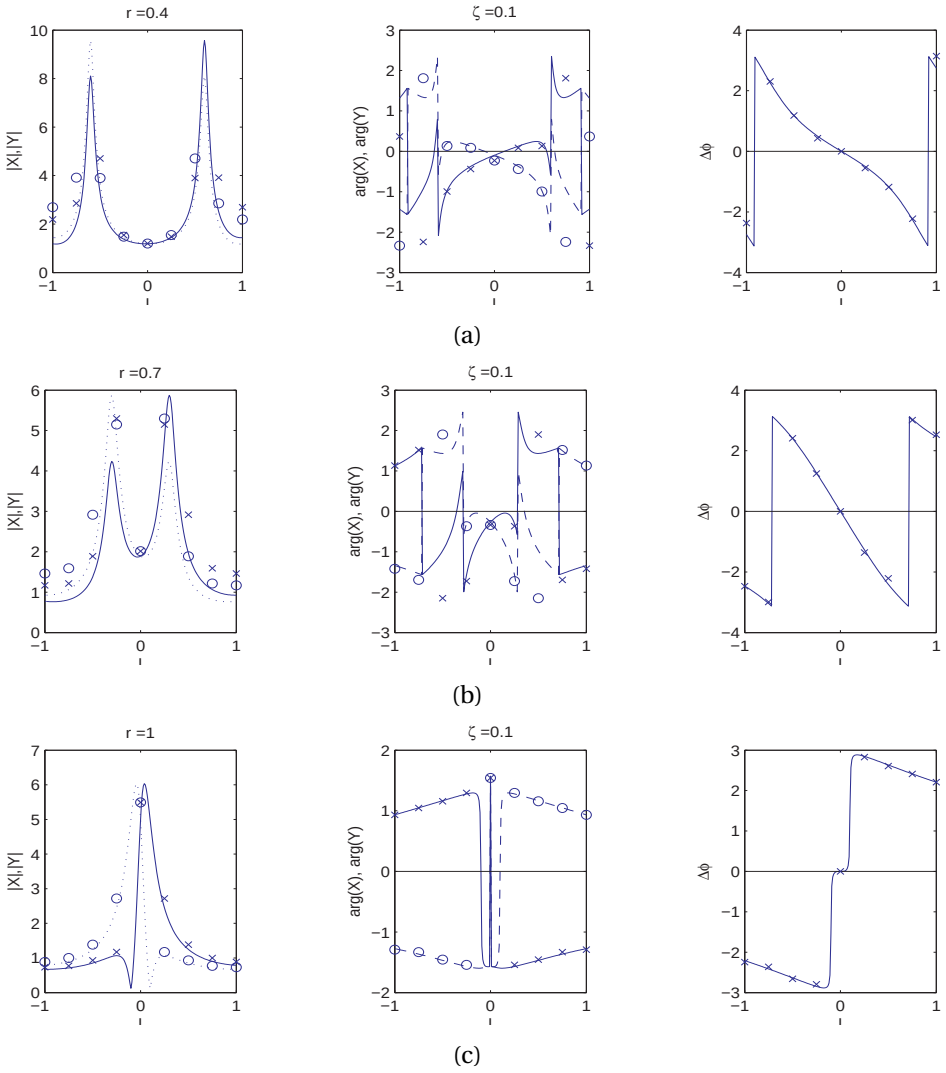

Figure 4.6. Mathematical (-) and Simulink (x,o) models

form an ellipse, which becomes a straight line slanted at 135° if $\beta = \pi$[1].

A similar effect is observed in the displacement of the two-dimensionally excited spring-mass-damper system and is depicted in Figures 4.8(a) and 4.8(d) for different damping ratios and $r = 0.5$. With in-phase two-dimensional harmonic excitation and zero angular velocity ($l = 0$), a straight line of vibration is obtained. With an applied rotation rate, the phase difference between the vibrations increases and the straight line of the proof mass displacement becomes more elliptical. Additionally, the ellipse increases in size as the amplitude of the vibration is also affected.

Figures 4.8(a) and 4.8(d) also illustrate the effect of damping on the transient response of the two-dimensionally excited system. With low damping (Fig. 4.8(a)),

[1] If different frequencies ω are used in x and y, Lissajous figures are obtained.

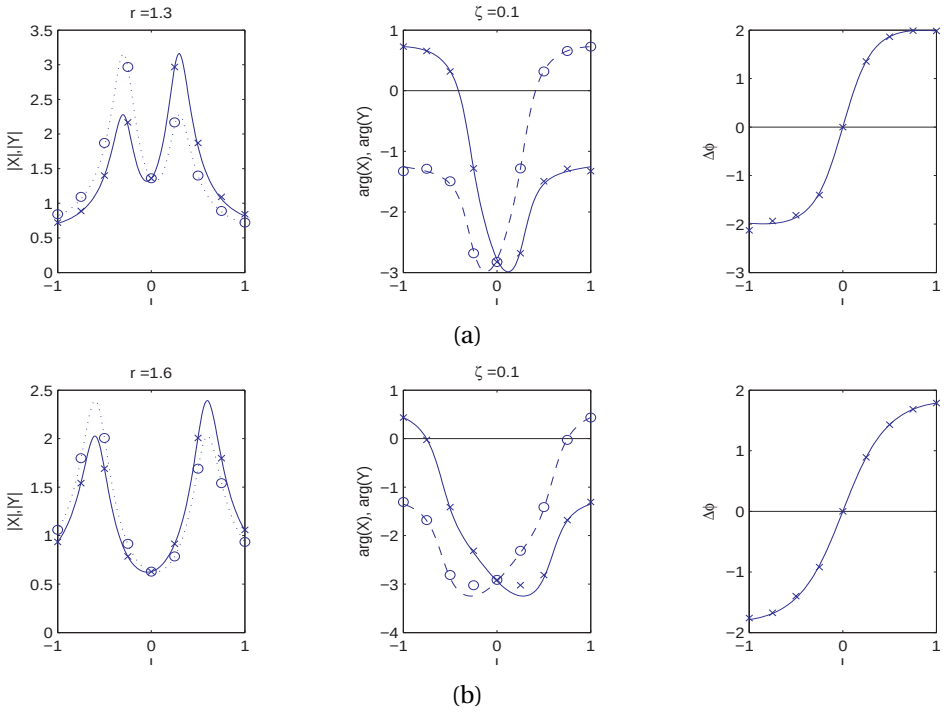

Figure 4.7. Mathematical (-) and Simulink (x,o) models

the vibrations tend to overshoot and more vibration cycles are needed for transient effects to disappear. With increased damping, the overshoots become less pronounced, but the ellipses are also smaller.

The transient analysis shows that dynamic effects play a definite role in the design of a phase-based gyroscope and will depend on r and the excitation forces. The dynamical effects should be considered when designing a physical device and bandwidth considerations need to be taken into account.

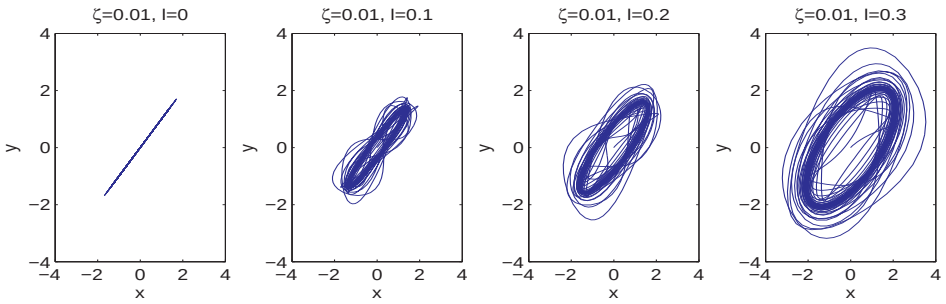

(a)

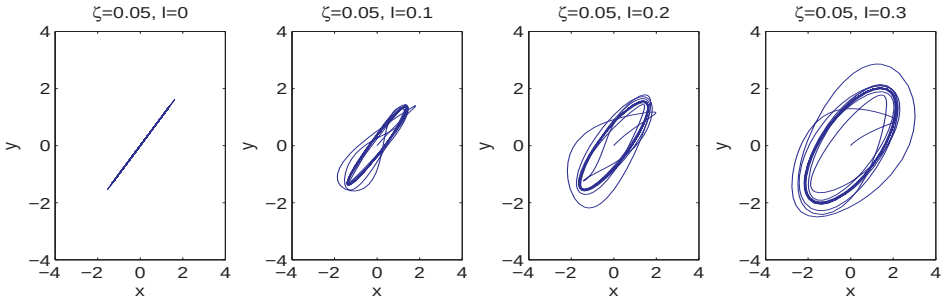

(b)

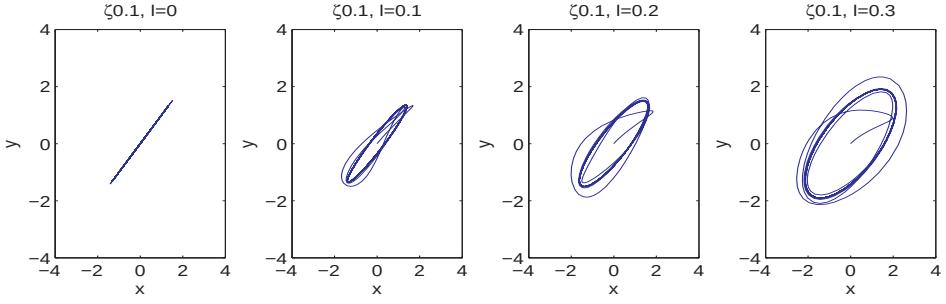

(c)

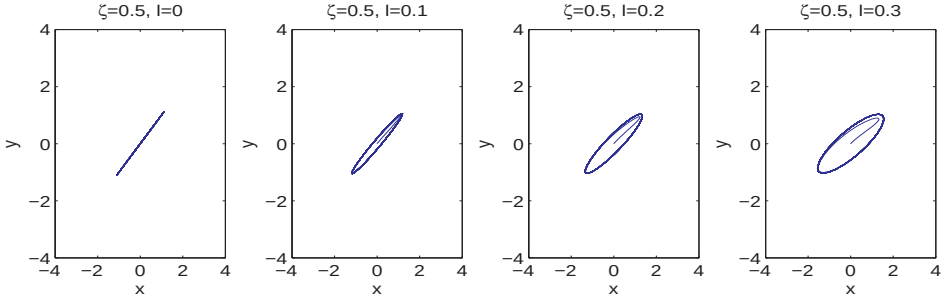

(d)

Figure 4.8. Proof mass vibration, $r = 0.5$

Chapter

5

Optimal design

In designing physical devices in general, certain design outputs need to be maximized, subject to various design and performance constraints. The same is true for a phase-based gyroscope. This chapter briefly deals with optimization of a non-dimensional model, to allow prediction of the performance limitations a phase-based operation mode would have in the presence of applied constraints. Using the non-dimensionalized form, general conclusions about the optimum design are made. An increased phase difference per rotation rate results in increased gyroscope sensitivity, making the scale factor the main design output at this stage. Physical design of the vibrating structure, measurement circuitry and noise considerations are not yet considered.

5.1 Scale factor optimization

In the previous chapters, the model was characterized and it was shown in Chapter 3 that the scale factor of a phase-based vibratory gyroscope is a function of the proof mass excitation frequency r, excitation force ratio f and damping ratio ζ. However, nonlinearities exist and forcing ratios notably affect the scale factor and the linearity of the phase difference. It was also found that the damping ratio significantly affects both the scale factor and the linearity of the phase difference.

With these factors in mind, the aim of the optimization is herein formulated as follows: Obtain the maximum scale factor, while adhering to certain linearity and design constraints. Figure 5.1 for example shows the scale factor of the phase difference $\Delta\phi$, as the tangent line at $l = 0$ for specific values of ζ, r and f. The figure also shows the differences between an ideal linear response and the actual response at the full scale range, respectively denoted δ_1 and δ_2. These occur at l_{min} and l_{max} (These nonlinearities are discussed in more detail in Section 5.2.1). Since the system has been characterized analytically, the scale factor is obtained

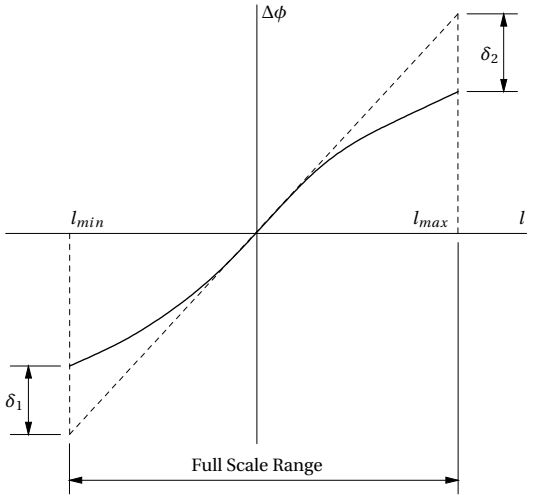

Figure 5.1. Scale Factor with nonlinearities

for general values of ζ, r and f by determining the partial derivative of the phase difference at $l = 0$, i.e.

$$\begin{aligned} \mathrm{SF} &= \left.\frac{\partial \Delta\phi}{\partial l}\right|_{l=0} \\ &= \frac{\partial}{\partial l}\left[\arctan\left(\frac{-2rl(1-r^2-l^2)(1+f^2)}{f(1-r^2-l^2)^2+4r^2(\zeta+lf)(\zeta f-l)}\right)\right]_{l=0}, \end{aligned} \tag{5.1.1}$$

where SF is the scale factor in radians per normalized rotation rate. To be more precise, the scale factor is actually a function of the variables, i.e. SF=SF(ζ, r, f). The unconstrained optimum scale factor is then defined by

$$\nabla \mathrm{SF}(\zeta, r, f) = 0, \tag{5.1.2}$$

where

$$\nabla \mathrm{SF}(\zeta, r, f) = \left\{\frac{\partial \mathrm{SF}}{\partial \zeta}, \frac{\partial \mathrm{SF}}{\partial r}, \frac{\partial \mathrm{SF}}{\partial f}\right\}, \tag{5.1.3}$$

with the additional requirement of the Hessian[1] being positive definite [119]. However, the above mentioned is difficult to determine analytically and is only true for the unconstrained optimization problem[2]. With the additional imminence of design constraints, which will invariably complicate the optimization, the analytical optimization of the scale factor is deferred to the route of simpler numerical optimization techniques.

[1] The Hessian is a matrix containing second order partial derivatives.

[2] For the constrained problem, the necessary and sufficient Karush-Kuhn-Tucker (KKT) conditions apply.

5.2 Constrained Numerical Optimization

Numerical optimization of multi-variable functions is a very active field and many algorithms exist. The Matlab constrained optimization function "fmincon" is used as a local solver (techniques to find the global optimum is discussed later on). Finding the optimum scale factor in the presence of constraints is now defined as a constrained optimization problem and is given as [120];

Find:

$$\min_{\vec{\vartheta}} F(\vec{\vartheta}) \tag{5.2.1}$$

subject to the nonlinear[3] design constraints

$$c_j(\vec{\vartheta}) \leq 0,\ j = 1,2,\ldots,m \tag{5.2.2}$$

with the variable bounds

$$lb_i \leq \vartheta_i \leq ub_i,\ \forall i. \tag{5.2.3}$$

The function to be minimized is the objective function $F(\vec{\vartheta})$, which is the negative of the scale factor, i.e. $F(\vec{\vartheta}) = -SF(\zeta, r, f)$[4]. The scale factor is computed numerically. The system variables $\vec{\vartheta}$ consist of the damping ratio ζ, the excitation frequency r and the forcing ratio f, i.e. $\vec{\vartheta} = \{\zeta, r, f\}$. The variables are bound by the lower and the upper bounds $\vec{\text{lb}}$ and $\vec{\text{ub}}$ respectively.

5.2.1 Non-linear constraints on scale factor linearity

To derive the constraints on the scale factor needed for the optimization algorithm, the scale factor nonlinearity is to be quantified. The maximum scale factor deviation from linearity occurs at the full scale range, is defined by δ_1 and δ_2, and is typically specified as a percentage error. The maximum allowable nonlinearity is defined as the largest of $|\delta_1|$ and $|\delta_2|$. The optimization is done for different values of prescribed allowable nonlinearity.

To obtain δ_1 and δ_2, the deviation from linearity is obtained by the difference between the analytical phase difference and the phase difference predicted by the scale factor at the full scale range, as depicted in Figure 5.1. The scale factor is calculated using the numerical derivative of the phase difference at the origin, where $l = 0$. Therefore, the nonlinearity at the full scale range is quantified as

$$\delta_1 = |\Delta\phi_{l_{min}} - l_{min} \times \text{SF}|, \tag{5.2.4}$$

[3]The term "nonlinear constraint" is used in optimization to indicate constraints that are not a linear combination of the system variables, and should not be confused with the constraint on the scale factor linearity. The fact that the nonlinear optimization constraint is also a constraint on linearity is merely a coincidence.

[4]A negative minimum gives a positive maximum.

$$\delta_2 = |\Delta\phi_{l_{max}} - l_{max} \times \text{SF}|, \tag{5.2.5}$$

or in percentages

$$\delta_{1_{perc}} = \left| \frac{\Delta\phi_{l_{min}}}{l_{min} \times \text{SF}} - 1 \right| \times 100, \tag{5.2.6}$$

$$\delta_{2_{perc}} = \left| \frac{\Delta\phi_{l_{max}}}{l_{max} \times \text{SF}} - 1 \right| \times 100, \tag{5.2.7}$$

with $\Delta\phi_{l_{min}}$ and $\Delta\phi_{l_{max}}$ being the analytical phase difference at the minimum and maximum full scale range. The maximum allowable nonlinearity is then obtained by $\max(\delta_{1_{perc}}, \delta_{2_{perc}})$. The constraint function implementation source code is listed in Appendix B.3.

5.2.2 Variable bounds

In every design there are bounds on the design variables due to physical restrictions, represented by the lower bound $\vec{\text{lb}}$ and the upper bound $\vec{\text{ub}}$. Since no detailed design of the physical system has yet been done, appropriate variable bounds are specified for the non-dimensionalized case. These bounds are not absolute, but at least aim to give an indication of which variable boundaries are of importance.

The variable bounds are taken as $0.001 \leqslant \zeta \leqslant 1$, to account for a wide range of damping ratios, $0.1 \leqslant r \leqslant 2$, since most interesting behaviour is around resonance and $0.01 \leqslant f \leqslant 100$ to allow for reasonable forcing ratios[5]. The boundaries are then given by

$$\vec{\text{lb}} = \begin{Bmatrix} 0.001 \\ 0.1 \\ 0.01 \end{Bmatrix}, \vec{\text{ub}} = \begin{Bmatrix} 1 \\ 2 \\ 100 \end{Bmatrix},$$

and are specified in the initialization of the optimization program before the optimization algorithm is invoked.

5.2.3 Optimization program

As mentioned, the Matlab constrained optimization function `fmincon` is used to obtain the optimum scale factor. The optimization algorithm is invoked by the following statement [120]:

```
[x,fvalue,exitflag]=fmincon(fun,x0,A,b,Aeq,beq,lb,ub,nonlcon,options)
```

The inputs of `fmincon` are:

[5] $0.01 \leqslant f \leqslant 1$ is equivalent, but does not allow for the inverse of the forcing ratio.

- `fun`: The function which evaluates the objective function $F(\boldsymbol{\vartheta})$ and calculates -SF.
- `x0`: The initial search values in vector form (to be discussed).
- `A,b,Aeq,beq`: The linear[6] equality and inequality constraints (not used).
- `lb,ub`: The variable lower and upper bounds.
- `nonlcon`: The function which calculates the nonlinear constraints $c_j(\boldsymbol{\vartheta})$.

The outputs of `fmincon` are:

- `x`: The optimum design variable values.
- `fvalue`: The optimum function value.
- `exitflag`: The convergence information flag.

The program subroutines are given in Appendix B.3, but a short summary of the code that invokes the optimization function is shown below:

1. Define variable lower bounds: `lb`
2. Define variable upper bounds: `ub`
3. Define initial variable values: `x0`
4. Set optimization options with `optimset`
5. Invoke optimization algorithm with `fmincon`
6. Do postprocessing

The function `optimset` is used to set the options used by the optimization algorithm, and is typically used by the statement

```
options = optimset('MaxFunEvals',1000,'TolFun',1e-9);
```

with `MaxFunEvals` being the maximum allowable function evaluations and `TolFun` the tolerance specifying the convergence criteria. A wide variety of other options are also available and discussed in the Matlab documentation. Options that gave satisfactory convergence results were chosen. With the optimization problem and implementation presented, the approach for selecting the initial values for the optimization algorithm is now discussed.

[6]The term "linear constraint" is again an optimization term, and is used to denote constraints which are formed by a linear combination of the design variables.

5.2.4 Optimization with random starting points

Before starting the optimization, initial values for the design variables need to be supplied by the user. In optimizing a complicated function, multiple local minima may be present, especially if constraints are also applied. The optimization algorithm may then converge to a local minimum, which is usually dependent on the initial values given to the algorithm. To circumvent the problem, the algorithm is re-run with random starting values. While this may be computationally expensive, the objective function used herein is relatively simple and is fortunately rapidly evaluated.

The random starting points used for the design variables are contained in the vector `x0`, and are generated between the lower and upper boundaries. This is easily done by generating a random number between zero and unity and mapping this to the range of variables between the lower and upper boundaries, and is implemented by the code:

```
range=ub-lb;            % Variable range
rndnum=rand(1,3);       % Generate random values between 0 and 1
x0 = range.*rndnum+lb;  % Map values of (0,1) -> (lb,ub)
```

5.3 Optimization results

Using multiple random initial search values, a range of optimum values are found for $F(\boldsymbol{\vartheta})$, together with the corresponding optimum design variables contained in $\boldsymbol{\vartheta}$. The values are tabulated, and plotted in a histogram to show the number of occurrences for each optimal function value. The values of l_{min} and l_{max} are chosen as ± 0.0015 for each optimization run[7], which is expected to be a typical maximum range value.

Consider the optimization results for a maximum allowable nonlinearity of $\delta_{max} = 5\%$, as given in Table 5.1 and Figure 5.2. The presented results are dimensionless and the scale factor SF is given in radians/normalized rotation rate [rad/l][8]. Table 5.1 shows the different local minima together with their corresponding optimal design variables. The global optimum of the scale factor is around 990, with additional local optima at about 276 and -0.388. These values correspond to the table entries of -990, -276 and 0.388. For the global minimum -990, $\zeta = 0.001$, $r = 1.0013$ and $f \approx 1$ with a convergence flag of 1. This means the damping ratio ζ is at the lower boundary, the excitation frequency r is almost at the system natural frequency and equal excitation forces are used. The convergence flag of

[7] $l_{max} = 0.0015$ corresponds to a full scale range of $\pm 500^{\circ}/s$ in a device with a natural frequency of 6000rad/s (about 1Khz).

[8] This may seem like an odd definition, but is used to conform with the dimensionless model; this will later be translated to more useful dimensions.

1 corresponds to the first order optimality measure being smaller than `TolFun`, which is used by the algorithm and specified in the optimization options.

The global optimum has a low number of occurrences in the histogram depicted in Figure 5.2, which means it is not easily found. The corresponding system response is shown in Figure 5.3(a), with the solid black line illustrating the the scale factor. The optimum is on the resonance spike, explaining its low occurrence.

The number of occurrences for the other local minima are more comparable (Fig. 5.2) and they are more easily found, although the function values are suboptimal. The second best optimal value is in the second row of Table 5.1, being -276, with $\zeta = 0.001$, again at the lower boundary, $r \approx 1.43$ and $f = 100$, with f at the upper boundary, as shown in Figure 5.3(b). The third row in the table is exactly the same, except for f being at its lower boundary, i.e. $f = 0.001$. The result for this case is depicted in Figure 5.4(a), again with the solid line indicating the scale factor. The exit flag of 4 corresponds to the magnitude of the linear search being less than the tolerance on the change in variables. This local optimum entails that the excitation frequency should be at $r = 1.43$, on the limit of the nonlinearity constraint. If $r < 1.43$, the constraint on linearity will be violated.

The fourth local minima is at 0.388 and is least optimal. The operating point corresponds to $\zeta = 1$, which is critical damping, $r = 0.1$, the lower excitation frequency boundary and $f = 1$; equal excitation forces. The corresponding response is depicted in Figure 5.4(b). Using a critical damping ratio is not a useful configuration in a physical device, since it minimizes the vibration amplitude and is only of academic interest.

δ_{max}	$-SF$	ζ	r	f	Flag
5%	-9.9033e+002	1.0000e-003	1.0012e+000	1.0045e+000	1
	-2.7637e+002	1.0000e-003	1.4253e+000	1.0000e+002	1&4
	-2.7637e+002	1.0000e-003	1.4253e+000	1.0000e-002	1&4
	3.8820e-001	1.0000e+000	1.0000e-001	1.0000e+000	1&4

Table 5.1. Optimization results: $\delta_{max} = 5\%$

The results of smaller allowable nonlinearities are also considered, namely allowable nonlinearity of $\delta_{max} = 2\%, 1\%, 0.5\%$ and 0.1%. These are too numerous to be presented here, and are given in Appendix C. In adding more stringent constraints on linearity, similar results are obtained as with $\delta_{max} = 5\%$. The global optimum is again at $r \approx 1$, except with $\delta_{max} = 1\%$. However, the absence of this optimum point for $\delta_{max} = 1\%$ is most likely due to general low occurrence of this point. The values of the scale factor at the global optimum are in the range 990 to 957 rad/l, which translates to around $0.16°/°/s$ for a device with $\omega_n = 6000 rad/s$ (or about 1kHz).

When less nonlinearity is allowed, the second local minimum increasingly moves away from $r = 1$ as δ_{max} is decreased, a conclusion which is expected, since

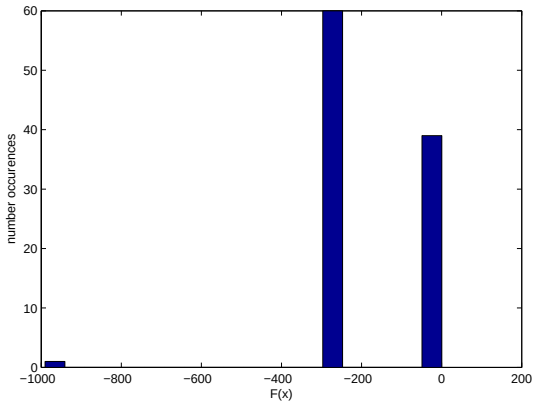

Figure 5.2. Histogram of optimal SF occurrences ($\delta_{max} = 5\%$)

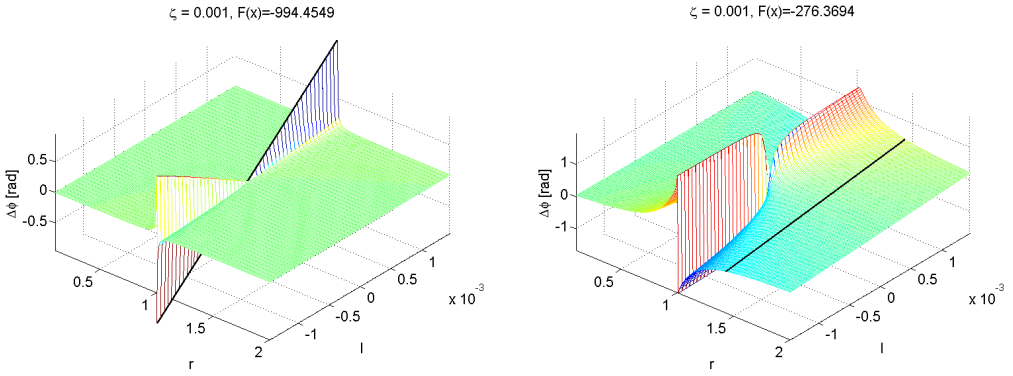

(a) (b)

Figure 5.3. Local minima for $F(\boldsymbol{\vartheta}) = -SF$, with $\delta_{max} = 5\%$

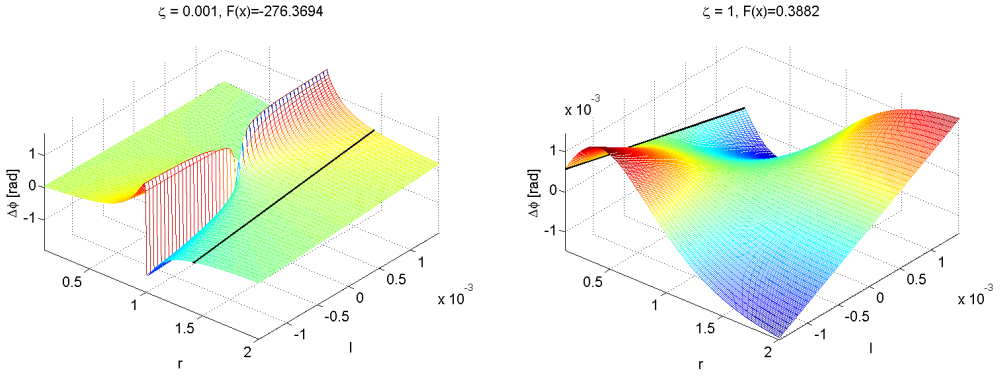

(a) (b)

Figure 5.4. Local minima for $F(\boldsymbol{\vartheta}) = -SF$, with $\delta_{max} = 5\%$

these local minima occur when the nonlinearity constraint becomes active. In fact, it moves so far away from $r = 1$ that it runs into the upper boundary for r.

The values of these local minima occur at scale factor ranges of 280 to 36 rad/l ($0.05 - 0.006°/°/s$) for values of δ_{max} ranging between 5% and 0.1%. Both the global optimum and second optimum scale factors again are at the lowest possible damping values.

The third local minimum, or critical damping ratio minimum, occurs at exactly the same position for every allowable δ_{max}. Each time the scale factor is 0.3882 ($6.5E-5°/°/s$), and the only variance is the convergence flag being 5 at $\delta_{max} =$ 0.1%, which corresponds to convergence due to the size of the directional derivative. The scale factor is much less than the first and second optima, and designing a phase-based gyroscope at this operating point not be sensible. With $\delta_{max} = 0.1\%$ and 0.5%, an apparent local optima is observed at $F(\boldsymbol{\vartheta}) = 0.404$, but is of no real interest, since it is attributed to premature convergence.

With the above mentioned in mind, the optimum scale factor of a phase based gyroscope occurs when the device is operated at resonance, with $r \approx 1$. A scale factor of about $0.16°/°/s$ is achievable for a device operating at about 1kHz and with a constraint on the damping ratio of 0.001, i.e. a quality factor of 500. The obtainable scale factor will be less for devices with larger natural frequencies. More specifically, a device with a resonant frequency of about 10kHz will have a scale factor of about $0.016°/°/s$. The sensitivity of the eventual sensor will be dependent on the accuracy of the circuitry used to measure the phase difference.

Using the resonance operating point, both directions should be excited into resonance. However, the frequency lock-in effect mentioned in Section 3.5.1 should then be well understood. Note that the resonance spike actually occurs at the damped natural frequency. At very low damping ratios the system will react similar to an undamped system, making the phase difference scale factor undefined, or infinite at resonance.

In the event that the frequency lock-in effect cannot be sufficiently studied or overcome, the phase detection scheme should not be used at resonance and simple harmonic excitation of proof mass may be used. The phase-based gyroscope should then be used at the second best optimum point, but a lower scale factor than at resonance is obtained, and linearity constraints need to be considered.

Chapter

6

Conclusions and Recommendations

6.1 Conclusions

In this thesis, the phase-based operation mode of a vibratory gyroscope has been explored for possible implementation as a MEMS vibratory gyroscope. Firstly, a broad study of existing gyroscope technology was performed to examine which existing gyroscope concepts can be implemented on the MEMS scale. The most promising concepts seem to be those that sense the frequency or phase of vibrations, as opposed to amplitude, to measure rotation rate. Using non-amplitude based methods may reduce the effect of noise, which is the major limiting factor in MEMS gyroscope performance.

Little research regarding frequency and phase-based gyroscopes has been reported, and some effects were inadequately explained by existing theoretical models. In an effort to better characterize the frequency and phase-based operation modes, a general mathematical model of a two-dimensionally excited two degree of freedom spring-mass-damper system with an applied rotation velocity has therefore been derived herein. A method similar as proposed by Linnett was used, who experimentally confirmed his formulation. Due to time constraints, experimental verification of the analytical model was not done. However, the analytical model was substantiated by additionally solving the system of equations using numerical methods. A brief investigation of the system transient response was also done using Simulink, which could be used in future follow-up research.

It was illustrated how the steady state response of the two-dimensionally excited 2-DOF spring-mass-damper system is affected by an applied rotation rate. Through simplifications on the general model, different cases in the literature were explained, including the frequently used amplitude detection method. It was observed that in using two-dimensional excitation, the vibration phase dif-

ference is an indication of rotation rate. The influences of the excitation frequency, damping ratio and excitation force ratio on the system response were also studied.

It was illustrated that a trade-off between the scale factor and the linearity of the phase difference needs to be made if the phase difference is used as a measure of rotation rate. Constrained numerical optimization was performed to find the optimum scale factor in the presence of constraints on the phase difference linearity.

During the optimization, it was observed that multiple local minima exist for the problem, and that the optimal design is at resonance. However, additional effects may inhibit the use at resonance, such as phase discontinuities, amplitude dead spots, low damping issues and a frequency lock-in effect. It was demonstrated that the next best option is to operate phase based gyroscopes away from resonance, when the phase difference scale factor is limited by nonlinearities.

6.2 Recommendations for future research

In this thesis, many types of gyroscopes have been investigated and a few were highlighted that may be of interest for future research, which include micro-optical and a gas jet gyroscopes. However, with most successful MEMS gyroscopes being of the vibratory kind, the frequency or phase-based concepts are recommended for further exploration. The presented theory may be useful if such studies are made.

A few issues specific to the phase-based measurement concept that are not addressed due to time or other constraints, include:

Dynamical Coupling and asymmetry effects: A general analytical model with coupling effects was developed, but only the symmetrical case was studied in detail. Exploring the coupling and asymmetric effects may yield interesting outcomes, which may or possibly imply increased phase differences due to stiffness, damping or inertial coupling, or increased phase differences due to asymmetries.

Electromechanical Coupling: It was shown that the optimal phase difference is at resonance, but electromechanical coupling effects may inhibit the use of a phase-based device at resonance. Better understanding of the electromechanical coupling effect is needed.

Transient effects: The transient response of the dual-excitation and phase detection method was only discussed in part, and should be explored in more detail to be able to make predictions on sensor dynamical characteristics like band-

width, overshoots, etc. Optimization of these transient effects can also be done in future research.

Actual design: Last but not least, is the design of an actual MEMS device. Although the theoretical analyses presented may be extremely useful, relating these to an actual design may well be more difficult than imagined herein. However, the methods provided in this thesis may prove valuable in first order approximations of the characteristics of a phase-based vibratory MEMS gyroscope. For example: a MEMS gyroscope can be designed and the damping, stiffness and mass parameters can be extracted by parameter estimation methods. These parameters can then be used in the analytical model presented in this thesis, or numerical optimization can be done. This may give valuable information regarding device performances, without the computationally expensive solution of large FEM models.

List of References

[1] Titterton, D. and Weston, J.: *Strapdown Inertial Navigation Technology*. Peter Peregrinus Ltd., 1997.

[2] Scarborough, J.: *The Gyroscope: Theory and applications*. Interscience Publishers, 1958.

[3] Laughlin, D., Sebesta, H. and Eckelkamp-Baker, D.: A dual function magnetohydrodynamic (MHD) device for angular motion measurement and control. In: *25th Annual AAS Guidance and Control Conference*. 2002.

[4] Merlo, S., Norgia, M. and Donati, S.: *Handbook of Fibre Optic Sensing Technology*, chap. 16, pp. 331–347. John Wiley and Sons Ltd., 2000.

[5] Stefatos, E., Arslan, T., Keymeulen, D. and Ferguson, I.: Towards the ingegration of drive control loop electronics of the JPL Boeing gyroscope within an autonomous robust custom-reconfigurable platform. In: *Proceedings of the First NASA/ESA Conference on Adaptive Hardware and Systems*. 2006.

[6] Gustavson, T., Bouyer, P. and Kasevich, M.: Precision rotation measurements with an atom interferometer gyroscope. *Physical Review Letters*, vol. 78, pp. 2046–2049, 1997.

[7] Development, Y.: Gyro markets. Tech. Rep., Yole Development, 2006.

[8] Xie, H. and Fedder, G.: Integrated microelectromechanical gyroscopes. *Journal of Aerospace Engineering*, vol. 16, pp. 65–75, 2003.

[9] John, J. and Vinay, T.: Novel concept of a single-mass adaptively controlled triaxial angular rate sensor. *IEEE Sensors Journal*, vol. 6, pp. 588–595, 2006.

[10] Piyabongkarn, D., Rajamani, R. and Greminger, M.: The development of a MEMS gyroscope for absolute angle measurement. *IEEE Transactions on control systems technology*, vol. 13, pp. 185–195, 2005.

[11] Shkel, A., Acar, C. and Painter, C.: Two types of micromachined vibratory gyroscopes. *IEEE Sensors*, pp. 531–536, 2005.

[12] Ayazi, F. and Najafi, K.: A HARPSS polysilicon vibrating ring gyroscope. *Journal of Microelectromechanical Systems*, vol. 10, pp. 169–179, 2001.

[13] Gretillat, F., Gretillat, M. and de Rooij, N.: Improved design of a silicon micromachined gyroscope with piezoresistive detection and electromagnetic excitation. *IEEE Journal of Microelectromechanical Systems*, vol. 8, pp. 243–250, 1999.

[14] Acar, C. and Shkel, A.: An approach for increasing drive-mode bandwidth of MEMS vibratory gyroscopes. *Journal of Microelectromechanical Systems*, vol. 14, pp. 520–528, 2005.

[15] Acar, C. and Shkel, A.: Inherently robust micromachined gyroscopes with 2-DOF sense-mode oscillator. *Journal of Microelectromechanical Systems*, vol. 15, pp. 380–387, 2006.

[16] Acar, C. and Shkel, A.: Structurally decoupled micromachined gyroscopes with post-release capacitance enhancement. *Journal of Micromechanics and Microengineering*, vol. 15, pp. 1092–1101, 2005.

[17] Lim, H., Song, J., Lee, J. and Kim, Y.: A few deg/hr resolvable low noise lateral microgyroscope. In: *The 15th IEEE International Conference on Micro Electro Mechanical Systems*. 2002.

[18] Barbour, N. and Schmidt, G.: Inertial sensor technology trends. *IEEE Sensors Journal*, vol. 1, pp. 332–339, 2001.

[19] King, A.: Inertial navigation - forty years of evolution. *GEC Review*, vol. 13, pp. 140–149, 1998.

[20] Lyon, D.: A military perspective on small unmanned aerial vehicles. *IEEE Instrumentation and Measurement Magazine*, pp. 27–31, September 2004.

[21] Kourepenis, A., Borenstein, J., Connely, J., Ward, P. and Weinberg, M.: Performance of small low-cost rate sensor for military and commercial applications. *Based on the paper published in The Proceedings of the AIAA Guidance Navigation and Control Conference*, 2006.

[22] Hughes, A.: BAE systems silicon vibrating structure gyroscope. Tech. Rep., BAE Systems, Inertial Systems Division, 2003.

[23] Weinberg, M. and Kourepenis, A.: Error sources in in-plane silicon tuning-fork MEMS gyroscopes. *Journal of Microelectromechanical Systems*, vol. 15, pp. 479–491, 2006.

[24] Barbour, N., Elwell, J. and Setterlund, R.: Inertial instruments: Where to now? In: *Proceedings AIAA Guidance Navigation and Control Conference*. 1992.

[25] Dixon, R. and Bouchard, J.: MEMS inertial sensors go consumer. *Think Small*, vol. 1, pp. 1–12, 2006.

[26] Brown, A.: MEMS across the valley of death. *Mechanical Engineering-CIME*, vol. 128, pp. 26–31, 2006.

[27] Lawrence, A.: *Modern Inertial Technology: Navigation, Guidance, and Control*. Springer, 1998.

[28] Yazdi, N., Ayazi, F. and Najafi, K.: Micromachined inertial sensors. *Proceedings of the IEEE*, vol. 86, pp. 1640–1659, 1998.

[29] Everett, H.: *Sensors for Mobile Robots: Theory and Application*. AK Peters Ltd., 1995.

[30] Gollomp, B.: Gyroscopes. *IEEE Instrumentation and Measurement Magazine*, pp. 49–52, September 2001.

[31] Bachan, M.: Gyroscopes. UCI EECS179 Lecture 10, 2005.

[32] Dauwalter, C. and Ha, J.: Magnetically suspended MEMS spinning wheel gyro. *IEEE A&E Systems Magazine*, pp. 21–26, 2005.

[33] Brittannica, E.: Ring laser gyroscope. *Encyclopedia Brittannica Online*, 2 Aug 2007. Online Article.
Available at: `http://www.brittannica.com/eb/art-74134`

[34] Taguchi, K., Fukushima, K., Ishitani, A. and Ikeda, M.: Experimental investigation of a semiconductor ring laser as an optical gyroscope. *IEEE Transactions on Instrumentation and Measurement*, vol. 48, pp. 1314–1318, 1999.

[35] Chow, W.W., Gea-Banacloche, J., Pedrotti, L.M., Sanders, V.E., Schleich, W. and Scully, M.O.: The ring laser gyro. *Rev. Mod. Phys.*, vol. 57, pp. 61–104, 1985.

[36] Lefevre, H.: The interferometric fiber-optic gyroscope. In: Udd, E. (ed.), *Fiber Optic Sensors*, vol. CR44. SPIE Optical Engineering Press, Bellingham, September 1992.

[37] Shkel, A.: Type I and type II micromachined vibratory gyroscopes. In: *IEEE/ION PLANS 2006 (invited)*, pp. 586–593. 2006.

[38] Painter, C.: Micromachined vibratory rate integrating gyroscope: Design, modeling, and experimental demonstration. Tech. Rep., University of California Irvine, 2002.

[39] Litty, E., Gresham, L., Toole, P. and Beisecker, D.: Hemispherical resonator gyro: an IRU for Cassini. In: *Proc. SPIE Vol. 2803, p. 299-310, Cassini/Huygens: A Mission to the Saturnian Systems, Linda Horn; Ed.* 1996.

[40] Loveday, P.: *Analysis and compensation of imperfection effects in piezoelectric vibratory gyroscopes*. Ph.D. thesis, Virginia Polytechnic Institute and State University, Mechanical Engineering, 1999.

[41] Agency, D.T.R.: *Militarily Critical Technologies List Section 16: Positioning, Navigation And Time Technology*. U.S.A. Department Of Defense, Ft. Belvoir, VA, August 2003.

[42] Desta, Y.: *Fabrication of high aspect ratio vibrating cylinder microgyroscope structures by use of the liga process*. Ph.D. thesis, Louisiana State University and Agricultural and Mechanical College Department of Mechanical Engineering, 2005.

[43] Watson, W. and Henke, T.: Coriolis gyro configuration effects on noise and drift performance. Tech. Rep., Watson Industries, 3041 Melby Road, Eau Claire, Wisconsin, USA, September 2002.

[44] Beitia, J., Gross, A. and Grosset, G.: New generation of inertial clusters for standby instruments based on vibrating sensors. *IEEE A&E Systems Magazine*, pp. 19–26, April 2006.

[45] Yang, J. and Fang, H.: Analysis of a rotating elastic beam with piezoelectric films as an angular rate sensor. *IEEE Transactions On Ultrasonics, Ferroelectrics, and Frequency Control*, vol. 49, pp. 798–804, 2002.

[46] Kagawa, Y., Wakatsuki, N., Tsuchiya, T. and Terada, Y.: A tubular piezoelectric vibrator gyroscope. *IEEE Sensors Journal*, vol. 6, pp. 325–330, 2006.

[47] Yang, J., Fang, H. and Jiang, Q.: Thickness vibrations of rotating piezoelectric plates. *Journal of the Acoustical Society of America*, vol. 104, pp. 1427–1435, 1998.

[48] Yang, J.: A review of analyses related to vibrations of rotating piezoelectric bodies and gyroscopes. *IEEE Transactions on Ultrasonics, Ferroelectrics, and Frequency Control*, vol. 52, pp. 698–706, 2005.

[49] Kurosawa, M., Fukuda, Y., Takasaki, M. and Higuchi, T.: A surface-acoustic-wave gyro sensor. *Sensors and Actuators A*, vol. 66, pp. 33–39, 1998.

[50] Zhou, Y. and Jiang, Q.: Effects of Coriolis force and centrifugal force on acoustic waves propagating along the surface of a piezoelectric half-space. *Zeitschrift faur angewandte Mathematik und Physik ZAMP*, vol. 52, pp. 950–965, 2001.

[51] Destrade, M.: Rayleigh waves in anisotropic crystals rotating about the normal to a symmetry plane. *Journal of Applied Mechanics: Transactions of the ASME*, vol. 71, pp. 516–520, 2004.

[52] Woods, R., Kalami, H. and Johnson, B.: Evaluation off a novel surface acoustic wave gyroscope. *IEEE Transactions on Ultrasonics, Ferroelectrics, and Frequency Control*, vol. 49, pp. 136–141, 2002.

[53] Ford, C., Ramberg, R., Johnson, K., Berglund, W., Ellerbusch, B., Schermer, R. and Gopinath, A.: Cavity element for resonant micro optical gyroscope. *IEEE AES Systems Magazine*, pp. 33–36, December 2000.

[54] Barbour, N. and Schmidt, G.: Inertial sensor technology trends. In: *Proceedings of the Workshop on Autonomous Underwater Vehicles*. 1998.

[55] USAF, J.S.L.: *The Air Force Institute of Technology (AFIT) MEMS Interferometric Gyroscope (MIG)*. Master's thesis, Air Force Institute of Technology, 2000.

[56] Burns, W. (ed.): *Optical Fiber Rotation Sensors*. Academic Press, 1994.

[57] Steinberg, B.: Rotating photonic crystals: A medium for compact optical gyroscopes. *Physical Review*, vol. 71, no. PACS numberssd: 41.20.2q, 42.70.Qs, 42.25.Bs, 31 May 2005 2005.

[58] Nayak, J. and Saraswat, V.: Studies on micro opto electro mechanical (MOEM) inertial sensors for future inertial navigation systems. In: *Proceedings of ISSS 2005, International Conference on Smart Materials Structures and Systems*. 2005.

[59] Senturia, S.: *Microsystem Design*. Springer, 2000.

[60] Dau, V., Dao, D., Shiozawa, T., Kumagai, H. and Sugiyama, S.: A single-axis thermal convective gas gyroscope. *Sensors and Materials*, vol. 17, pp. 453–463, 2005.

[61] Dau, V., Dao, D., Shiozawa, T., Kumagai, H. and Sugiyama, S.: Development of a dual-axis thermal convective gas gyroscope. *Journal of Micromechanics and Microengineering*, vol. 16, pp. 1301–1306, 2006.

[62] Zhou, J., Yan, G., Zhu, Y., Xiao, Z. and Fan, J.: Design and fabrication of a microfluid angular rate sensor. In: *The 18th IEEE International Conference on Micro Electro Mechanical Systems*. 2005.

[63] Piazza, G. and Stephanou, P.: Micromechanical thermo-fluidic single-axis yaw rate sensor, 2002. University of California, Berkeley.

[64] Barber, R. and Emerson, D.: A numerical investigation of low reynolds number gaseous slip flow at the entrance of circular and parallel plate micro-channels. In: *ECCOMAS Computational Fluid Dynamics Conference*. 2001.

[65] Eichholz, J., Quenzer, J., Schwarzelbach, O., Weiss, M. and Wenk, B.: Hdl-a-model of a micromachined tuning fork gyroscope. In: *Technical Proceedings of the 2000 International Conference on Modeling and Simulation of Microsystems*. 2000.

[66] Chen, Y., Jiao, J., Xiong, B., Che, L., Li, X. and Wang, Y.: A novel tuning fork gyroscope with high q-factors working at atmospheric pressure. *Microsystem Technologies*, vol. 11, pp. 111–116, 2005.

[67] Sassen, S., Voss, R., Schalk, J., Stenzel, E., Gleissner, T., Gruenberger, R., Neubauer, F., Ficker, W., Kupke, W., Bauer, K. and Rose, M.: Tuning fork silicon angular rate sensor with enhance performance for automotive applications. *Sensors and Actuators A*, vol. 83, pp. 80–84, 2000.

[68] Weinberg, M., Bernstein, J., Cho, S., King, A., Kourepenis, A., Ward, P. and Sohn, J.: A micromachined comb-drive tuning fork gyroscope for commercial applications. In: *Procceedings of the Sensor Expo, Cleveland, OH*, pp. 187–193. 1994.

[69] Li, X., Chen, X., Song, Z., Dong, P., Wang, Y., Jiao, J. and Yang, H.: A microgyroscope with piezoresistance for both high-performance Coriolis-effect detection and seesaw-like vibration control. *Journal of Microelectromechanical Systems*, vol. 15, pp. 1698–1707, 2006.

[70] Kim, J., Park, S., Kwak, D., Ko, H. and Cho, D.: An x-axis single-crystalline silicon microgyroscope fabricated by the extended smb process. *Journal of Microelectromechanical Systems*, vol. 14, pp. 444–455, 2005.

[71] Mochida, Y., Tamura, M. and Ohwada, K.: A micromachined vibrating rate gyroscope with independent beams for the drive and detection modes. *Sensors and Actuators A*, vol. 80, pp. 170–178, 2000.

[72] Fujita, T., Maenaka, K., Mizumo, T., Matsuoka, T., Kojima, T., Oshima, T. and Maeda, M.: Disk-shaped bulk micromachined gyroscope with vacuum sealing. *Sensors and Actuators A*, vol. 82, pp. 198–204, 2000.

[73] Sparks, D., Massoud-Ansari, S. and Najafi, N.: Long-term evaluation of hermetically glass frit sealed silicon to pyrex wafers with feedthroughs. *Journal of Micromechanics and Microengineering*, vol. 15, pp. 1560–1564, 2005.

[74] Choa, S.: Reliability of MEMS packaging: vacuum maintenance and packaging induced stress. *Microsystem Techonology*, vol. 11, pp. 1187–1196, 2005.

[75] Alper, S. and Akin, T.: A single-crystal silicon symmetrical and decoupled MEMS gyroscope on an insulating substrate. *Journal of Microelectromechanical Systems*, vol. 14, pp. 707–717, 2005.

[76] Geiger, W., Folkmer, B., Merz, J., Sandmaier, H. and Lang, W.: A new silicon rate gyroscope. *Sensors and Actuators A*, vol. 73, pp. 45–51, 1999.

[77] Maenaka, K., Ioku, S., Sawai, N., Fujita, T. and Takayama, Y.: Design, fabrication and operation of MEMS gimbal gyroscope. *Sensors and Actuators A*, vol. 121, pp. 6–15, 2005.

[78] Rajendran, S. and Liew, K.: Design and simulation of an angular-rate vibrating microgyroscope. *Sensors and Actuators A*, vol. 116, pp. 241–256, 2004.

[79] Acar, C.: *Four Degrees-of-Freedom Micromachined Gyroscope*. Master's thesis, University of California, Irvine, 2001.

[80] Acar, C. and Shkel, A.: Nonresonant micromachined gyroscopes with structural mode-decoupling. *IEEE Sensors Journal*, vol. 3, pp. 497–506, 2003.

[81] Acar, C. and Shkel, A.: Non-resonant surface-micromachined z-axis gyroscopes utilizing torsional out-of-plane detection. In: *Sensors, 2004. Proceedings of IEEE*. 2004.

[82] Acar, C. and Shkel, A.: Design concept and preliminary experimental demonstration of MEMS gyroscopes with 4-dof master-slave architecture. In: *SPIE Conference on Smart Electronics and MEMS*. 2002.

[83] Esmaeili, M., Durali, M. and Jalili, N.: Ring microgyroscope modeling and performance evaluation. *Journal of Vibration and Control*, vol. 12, pp. 537–553, 2006.

[84] Gallacher, B., Hedley, J., Burdess, J., Harris, A., Rickard, A. and King, D.: Electrostatic correction of structural imperfections present in a microring gyroscope. *Journal of Microelectromechanical Systems*, vol. 14, pp. 221–234, 2005.

[85] Painter, C. and Shkel, A.: Detection of orientation and predicted performance of a MEMS absolute angle measuring gyroscope. In: *Proceedings of the 4th International Workshop on Structural Health Monitoring (SHM 2003)*. 2003.

[86] Gallacher, B., Burdess, J., Harris, A. and Mcnie, M.: Principles of a three-axis vibrating gyroscope. *IEEE Transactions on Aerospace and Electronic systems*, vol. 37, pp. 1333–1343, 2001.

[87] Chang, C., Chou, C. and Lai, W.: Vibration analysis of a three-dimensional ring gyroscope. *Bulletin of the College of Engineering, N.T.U.*, vol. 91, pp. 65–73, 2004.

[88] Moussa, H. and Bourquin, R.: Theory of direct frequency output vibrating gyroscopes. *IEEE Sensors Journal*, vol. 6, pp. 310–315, 2006.

[89] Abe, M., Shinohara, E., Hasegawa, K., Murata, S. and Esashi, M.: Trident-type tuning fork silicon gyroscope by the phase difference detection. In: *Proceedings of the 13th IEEE International Conference on Microelectromechanical Systems*, pp. 508–513. 2000.

[90] John, J., Jakob, C., Vinay, T. and Qin, L.: Phase differential angular rate sensor-concept and analysis. *IEEE Sensors Journal*, vol. 4, pp. 471–478, 2004.

[91] Yang, H., Bao, M., Yin, H. and Shen, S.: Two-dimensional excitation operation mode and phase detection scheme for vibratory gyroscopes. *Journal of Micromechanics and Microengineering*, vol. 12, pp. 193–197, 2002.

[92] Yang, H., Bao, M., Yin, H. and Shen, S.: A novel bulk micromachined gyroscope based on a rectangular beam-mass structure. *Sensors and Actuators A*, vol. 96, pp. 145–151, 2002.

[93] Linnet, J.: Methods of using a vibratory system to measure small rates of turn. *Journal of Mechanical Engineering Science*, vol. 11, pp. 526–533, 1969.

[94] Madou, M.: *Fundamentals of Microfabrication: The Science of Miniaturization, Second Edition*. CRC Press, 2002.

[95] Erismis, M.: *MEMS Accelerometers And Gyroscopes For Inertial Measurement Units*. Master's thesis, The graduate school of natural and applied sciences, Middle East Technical University, 2004.

[96] Degani, O., Seter, D., Socher, E., Kaldor, S. and Nemirovsky, Y.: Optimal design and noise consideration of micromachined vibrating rate gyroscope with modulated integrative differential optical sensing. *Journal of Microelectromechanical Systems*, vol. 7, pp. 329–338, 1998.

[97] Degani, O., Seter, D., Socher, E. and Nemirovsky, Y.: A novel micromachined vibrating rate gyroscope with optical sensing and electrostatic actuation. *Sensors and Actuators A*, vol. 83, pp. 54–60, 2000.

[98] Yazicioglu, R.: *Surface Micromachined Capacitive Accelerometers Using MEMS Technology*. Master's thesis, Middle East Technical University, 2003.

[99] Kenny, T., Waltman, S., Reynolds, J. and Kaiser, W.: A micromachined silicon electron tunneling sensor. In: *Micro Electro Mechanical Systems, Proceedings, An Investigation of Micro Structures, Sensors, Actuators, Machines and Robots , IEEE*. 1990.

[100] Kubena, R., Vickers-Kirby, D. and Joyce, R.: A new tunneling-based sensor for inertial rotation rate measurements. *Journal of Microelectromechanical Systems*, vol. 8, pp. 439–447, 1999.

[101] Beeby, S., Ensell, G., Kraft, M. and White, N.: *MEMS Mechanical Sensors*. Boston: Artech House, 2004.

[102] Apostolyuk, V.: *MEMS/NEMS Handbook Techniques and Applications*. Springer, 2006.

[103] Meriam, J. and Kraige, L.: *Engineering Mechanics: Dynamics*. John Wiley and Sons Inc., 1998.

[104] Davis, W.: *Mechanical Analysis and Design of Vibratory Micromachined Gyroscopes*. Ph.D. thesis, University of California, Berkeley, 2001.

[105] Rao, S.: *Mechanical Vibrations*. Pearson Prentice Hall, 2004.

[106] Linnet, J.: The effect of rotation on the steady state response of a spring-mass system under harmonic excitation. *Journal of Sound and Vibration*, vol. 35, pp. 1–11, 1974.

[107] Stewart, J.: *Calculus Early Transcendentals*. Brooks/Cole, 1999.

[108] Abramowitz, M. and Stegun, I.: *Handbook of Mathematical Functions with Formulas, Graphs, and Mathematical Tables*. Dover Publications, Inc. New York, 1970.

[109] Hong, Y., Lee, J. and Kim, S.: A laterally driven symmetric micro-resonator for gyroscopic applications. *Journal of Micromechanics and Microengineering*, vol. 10, pp. 452–458, 2000.

[110] Alper, S. and Akin, T.: Symmetrical and decoupled nickel microgyroscope on insulating substrate. *Sensors and Actuators A*, vol. 115, pp. 336–350, 2004.

[111] Alper, S., Silay, K. and Akin, T.: A low-cost rate-grade nickel microgyroscope. *Sensors and Actuators A*, vol. 132, pp. 171–181, 2006.

[112] Smith, J.: *Introduction to Digital Filters*. W3K Publishing, May 2006.

[113] Leland, R.: Adaptive mode tuning for vibrational gyroscopes. *IEEE Transactions on Control Systems Technology*, vol. 11, pp. 242–247, 2003.

[114] Leland, R.: Adaptive control of a MEMS gyroscope using lyapunov methods. *IEEE Transactions on Control Systems Technology*, vol. 14, pp. 278–283, 2006.

[115] Alper, S. and Akin, T.: A symmetric surface micromachined gyroscope with decoupled oscillation modes. *Sensors and Actuators A*, vol. 97-98, pp. 347–358, 2002.

[116] Duwel, A., Gorman, J., Weinstein, M., Borenstein, J. and Ward, P.: Quality factors of MEMS gyros and the role of thermoelastic damping. In: *Proceedings of the 15th IEEE International Conference on Microelectromechanical Systems*, pp. 214–219. 2002.

[117] Patek, S. and Athans, M.: *The Control Handbook*. CRC Press, 1996.

[118] Compere, M.: Modified averaged spectrum analyzer. Matlab Central File exchange, February 2003.

[119] Vanderplaats, G.: *Numerical Optimization Techniques for Engineering Design*. Vanderplaats Research and Development, 2005.

[120] *Matlab Documentation*, 2007.

[121] Weisstein, E.: Inverse tangent. From MathWorld A Wolfram Web Resource, February 2006.
Available at: `http://mathworld.wolfram.com/InverseTangent.html`

[122] Kitagawa, G. and Gersch, W.: *Smoothness Priors Analysis of Time Series*. Springer, 1996.

[123] Ghiglia, D. and Pritt, M.: *Two-Dimensional Phase Unwrapping: Theory, Algorithms, and Software*. Wiley-Interscience, 2001.

[124] Chilton, E. and Hassanain, E.: Phase estimation of minimum phase systems using the hartley phase cepstrum. In: *Proceedings of the 24th IASTED International Multi-Conference, Signal Processing, Pattern Recognition and Applications*. 2006.

Appendices

Appendix

A

Quirks of arctan

Using **arctan** to determine the phase angle of a phasor is standard practice and mathematically sound, but it can have certain complications in the way it is applied. Artificial discontinuities can arise purely from the way arctan is defined, and although some of the following statements may seem trivial, they are deemed necessary to mention. Consider a complex number $z = a + bi$, which defines a rotating vector in the complex plane, depicted in Figure A.2. The vector defines a phasor, which is used to contain a sinusoid's amplitude and phase.

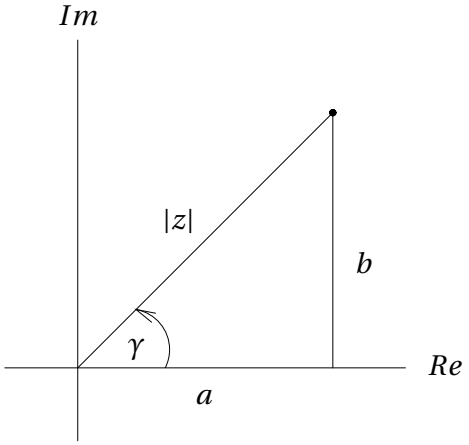

Figure A.1. The complex plane

The argument or angle γ is changed continuously as the point is rotated about the origin and is obtained by using the arctan function. However, arctan is only defined in a range of $-\frac{\pi}{2} < \gamma < \frac{\pi}{2}$ [107], which can be clearly seen by examining it's graph of principle values (Figure A.2).

It should be kept in mind that arctan is the inverse of tan, a periodic function with a period of π. Therefore, arctan is actually a multivalued function [121], and for

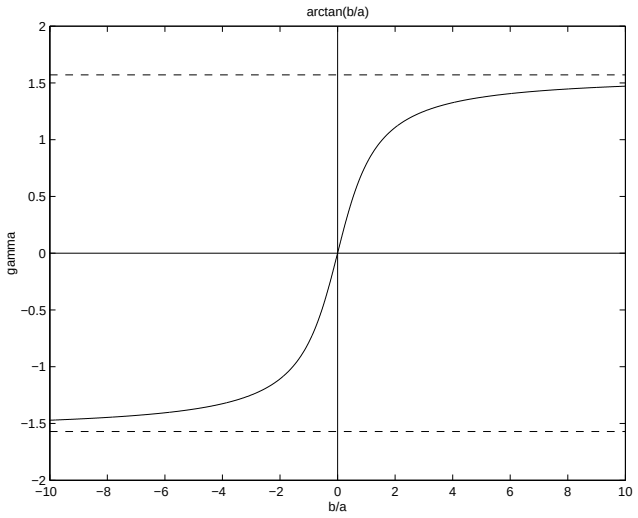

Figure A.2. The arctan function

a single independant variable value there are infinite function values of integer multiples of π added to the principle value.

Note that jump discontinuities occur when crossing the asymptotes of angles at $\pm\frac{n\pi}{2}$ (with $n = 1,3,5\ldots$), which happens when a changes its sign. This implies that $\frac{b}{a}$ is infinite ($a \to 0, \frac{b}{a} \to \infty$) or more specifically,

$$\lim_{\frac{b}{a}\to\infty} \arctan\left(\frac{b}{a}\right) = \frac{\pi}{2}$$

and

$$\lim_{\frac{b}{a}\to-\infty} \arctan\left(\frac{b}{a}\right) = -\frac{\pi}{2}$$

Although the rotating vector only rotates between the first and second or third and fourth quadrants, jumps of $\pm\pi$ occurs in the phase values. It is necessary to have additional information about the quadrant of z when determining the angle γ, and the asymptotes also need to be accounted for. These factors are usually overcome in programming languages by a function `atan2`, which take the horizontal and vertical arguments a and b instead of only $\frac{b}{a}$, and usually has the range of $-\pi < \gamma < \pi$ or $0 < \gamma < 2\pi$.

Arctan2 is therefore also multivalued, but with integer multiples of 2π, instead of π. Its discontinuities are encountered in full circle jumps, or when it is "wrapped around". It is usually dealt with by adding or subtracting an integer multiple of 2π to the piece of the phase that is affected. This process is called phase unwrapping [112].

Phase unwrapping is simple when working with smooth phase responses, but can become very involved when the phase information has jumps and spikes that

in the order of 2π. The problem of phase-discontinuities is widespread and occurs in most applications where phase responses are used. This includes speech analysis, geophysics, underwater acoustics spectrum analysis[122] and image processing [123]. Phase unwrapping is a well-researched subject, using various algorithms and can also be done in two dimensions [123].

A more recent approach to the phase discontinuity problem has also been reported, since phase response analysis is getting more important. The Hartley Transform (similar to the Fourier Transform) can be used to circumvent the use of arctan and the need for phase unwrapping [124]. The approach is only mentioned for reference.

Appendix

B

Matlab code

B.1 Analytical response calculation

The script given below was developed to calculate system response values according to the analytical model derived in Chapter 3.

```
function [modX,modY,argX,argY,verskil] = simmetries3D(zet,r,l,Xs,Ys)

% Assume symmetry
zet1 = zet; zet2 = zet; r1 = r; r2 = r; l1 = l; l2 = l;

%========= complex number = (a+bi)/(c+di) ==========
%--------------X-direction-------------------------
ax = (1-r2.*r2-l2.*l2).*Xs;

bx = 2.*zet2.*r2.*Xs + 2*r1.*l1.*Ys;

cx = (1-r1.*r1-l1.*l1).*(1-r2.*r2-l2.*l2)...
    - 4*zet1.*zet2.*r1.*r2 - 4*r1.*r2.*l1.*l2;

dx = 2*zet1.*r1.*(1-r2.*r2-l2.*l2)...
    +2*zet2.*r2.*(1-r1.*r1-l1.*l1);

modX = sqrt((ax.*ax+bx.*bx)./(cx.*cx+dx.*dx));

argX = atan(bx./ax)-atan(dx./cx) ;

%---------------Y-direction-------------------------
ay = (1-r1.*r1-l1.*l1).*Ys;
```

```
by = 2*zet1.*r1.*Ys-2*r2.*l2.*Xs;

cy = (1-r1.*r1-l1.*l1).*(1-r2.*r2-l2.*l2)...
    - 4*zet1.*zet2.*r1.*r2-4*r1.*r2.*l1.*l2;

dy = 2*zet1.*r1.*(1-r2.*r2-l2.*l2)...
    +2*zet2.*r2.*(1-r1.*r1-l1.*l1);

modY = sqrt((ay.*ay + by.*by)./(cy.*cy + dy.*dy));

argY = atan(by./ay) - atan(dy./cy) ;

verskil = argY - argX;
```

B.2 State space validation of Analytical response

The script shown below was developed to validate the analytical model with a numerically solved state space model and to plot the corresponding figures.

```
% This file plots the analytical and state models on the same graphs

%-------------Dimensionless Constants-------------------------
Xs = 1; %X amplitude ( x = Xs*e^jwt)
Ys = 1; %Y amplitude ( y = Ys*e^jwt)

t = 0;

rb = 0.1; re = 1.9; hr = 0.3; rlen = rb:hr:re;

lb = -0.5; le = 0.5; hl = 0.01;

%assestelsels
yminmod = -1; ymaxmod = 6;

fntsz = 24; fntsztx = 24;

%-----------------------------------------------------------
%introduce illustration variables- use different zet values
zet = 0.05; rss = 0.1:0.05:2; lss = -0.5:0.05:0.5;
```

```
%---------------------state space model----------------------
wn = 1; m=1; w=rss*wn; omgaarr=lss*wn; szeomga = max(size(lss));
smagx=zeros(szeomga,length(w));

for i = 1:szeomga

    omga=omgaarr(i);
    omgaplt(i)=omga;
    wn1=wn;
    wn2=wn;
    zet1 = zet;
    zet2 = zet;

    A =  [ 0            0               1             0;...
           0             0               0             1;...
           omga^2-wn1^2 0              -2*zet1*wn1    2*omga;...
           0             omga^2-wn2^2   -2*omga       -2*zet2*wn2];

    B = [0   0;...
           0   0;...
           1/m 0;...
           0   1/m];

    C = [1 1 0 0;...
           1 1 0 0];
    D = 0;

    mdk = ss(A,B,C,D);

    [mag,phase]=bode(mdk,w);

    sze=max(size(mag));

    xmag=reshape(mag(1,1,:),1,sze);
    xphase=reshape(phase(1,1,:),1,sze);
    ymag=reshape(mag(2,2,:),1,sze);
    yphase=reshape(phase(2,2,:),1,sze);


    smagx(i,:) = xmag(1,:);
    smagy(i,:) = ymag(1,:);
    sphasex(i,:) = pi/180*xphase(1,:);
    sphasey(i,:) = pi/180*yphase(1,:);
```

```
end;

% Unwrapping
phasediff=unwrap(sphasey-sphasex);
phasediff(:,91:max(size(rss)))=phasediff(:,91:max(size(rss)))+2*pi;

%-------------------------------------------------------------
% Do Plotting

hOmega =0.1;

for r = rb:hr:re            %Plots for different r

    t = t+1;
    l = lb:hl:le;
    indxr=findindx(rss,r);  %Find indexes of corresponding r values

    % Do plotting
    for zet = zet%:0.15:0.45

        [modX,modY,argX,argY,verskil] = simmetries3D(zet,r,l,Xs,Ys);

        figure(t);
        subplot(1,3,1)
        hold on
        plot(l,modX,'-')
        hold on
        plot([lb le],[0 0],'k')
        for lomga = lb:hOmega:le
            indxl=findindx(lss,lomga) ;
            plot(lomga,smagy(indxl,indxr),'o');
        end
        axis([lb le yminmod ymaxmod])
        ylabel('|X|','interpreter','tex')
        xlabel('l')

        subplot(1,3,2)
        hold on
        plot(l,modY,'-')
        hold on
        plot([lb le],[0 0],'k')
        for lomga = lb:hOmega:le
            indxl=findindx(lss,lomga);
            plot(lomga,smagx(indxl,indxr),'o');
```

```
        end
        axis([lb le yminmod ymaxmod])
        ylabel('|Y|','interpreter','tex')
        xlabel('l')
        title(['r =',num2str(rlen(t))],'interpreter','tex')

        subplot(1,3,3)
        hold on
        plot(l,verskil);
        hold on
        plot([lb le],[0 0],'k')
        cntl=0;
        for lomga = lb:hOmega:le    %plot statespace points
            indxl=findindx(lss,lomga);

            if (-phasediff(indxl,indxr)>pi)   %unwrapping
                plot(lomga,-phasediff(indxl,indxr)-2*pi,'o');
            else
                plot(lomga,-phasediff(indxl,indxr),'o');
            end

        end
        ylabel('\Delta\phi','interpreter','tex')
        xlabel('l')
        %title(['r =',num2str(rlen(t))],'interpreter','tex')

    end;
end;

% This function is used to find indexes of corresponding
% r-values in the 3-D analytical representation and the 2-D
% state space representation. Only the corresponding r values
% are searched in order to do plot the corresponding line.
    function [indx] = findindx(matr,val)

flag = 0; rndnum =1000;

[szer,szec] = size(matr);

for r = 1:szer
    for c = 1:szec
        if (round(rndnum*matr(r,c))==round(rndnum*val))
            i=r;
            j=c;
```

```
            flag=1;
        end
    end
end

indx=max([i j]);

if (~flag)
    disp('No value found!!')
end
```

B.3 Optimization code

This section contains the code developed for optimization.

```
%-----------------------------------------------------------
% Run optimization with random starting points
%-----------------------------------------------------------
clear all, close all    %clear workspace
clc

nrit=100;    %number of iterations for random starting points

% Define optimization variable bounds  (lb<=x<=ub)
% Variable lower bounds (lb)
lb(1) = 0.001;    % zet
lb(2) = 0.1;      % r
lb(3) = 0.01;     % forcing ratio Frat=Ys/Xs
% Variable upper bounds (ub)
ub(1) = 1;        % zet
ub(2) = 2;        % r
ub(3) = 100;      % forcing ratio Frat=Ys/Xs

% Set optimization options
options =
optimset('Display','off','MaxFunEvals',5000,'TolFun',1e-10,'TolX',1e-8);

% Define variable ranges (vectors)
rnge=ub-lb;

% Do optimization for different starting points
for i =1:nrit
```

```
    %generate random starting point
    rndnum=rand(1,3);
    x0= rnge.*rndnum+lb;

    %do optimization
    [x,fvalue,exitflag]=fmincon(@testscalepdiff, x0,...
    [],[],[],[],lb,ub,@testconfunpdiff,options);

    %Store values in structure
    optimstruct(i).x0(1)=x0(1);
    optimstruct(i).x0(2)=x0(2);
    optimstruct(i).x0(3)=x0(3);
    optimstruct(i).x(1) =x(1);
    optimstruct(i).x(2) =x(2);
    optimstruct(i).x(3) =x(3);
    optimstruct(i).fx   =fvalue;
    optimstruct(i).flag =exitflag;
    f(i)=fvalue;
    clear x0
end

% Draw histogram of function values
hist(f,20) xlabel('F(x)') ylabel('number occurences')

% Display table of results
[fsrt,indxsrt]=sort(f);     % Sort table of results


disp(sprintf('---(-SF)---|----zeta-----|------r------|----Frat----...
-|flag|----zeta0----|------r0-----|----Frat-----'));
% Display table entries
for i = 1:nrit
    t=indxsrt(i);
    x0(1)=optimstruct(t).x0(1);
    x0(2)=optimstruct(t).x0(2);
    x0(3)=optimstruct(t).x0(3);
    x(1) =optimstruct(t).x(1);
    x(2) =optimstruct(t).x(2);
    x(3) =optimstruct(t).x(3);
    fvalue=optimstruct(t).fx;
    flag=optimstruct(t).flag;
    disp(sprintf('%.4e | %.4e | %.4e | %.4e | %d  | %.4e , %.4e , %.4e ',...
    fvalue,x(1),x(2),x(3),flag,x0(1),x0(2),x0(3)));
end
```

Code to numerically calculate the scale factor.

```
    % Function to calculate scale factor of phase difference
% for use in fmincon optimization routine

function scalef = testscalepdiff(x)

% Input variables
zet = x(1); r   = x(2); rat = x(3);

% Specify l for full scale range (lmax)
lmax=pi/180*500/6000;   % Typical lmax value
%lmax=(pi/180*deg/s)/(rad/s)=[(rad/s)/(rad/s)]

%Determine scale factor at origin numerically
%Note: testfunpdiff is the same as simmetries3D

% Scalefactor estimation point 2 in [rad/s]
l= lmax/20; lbo=l; verskil2 = testfunpdiff(zet,r,lbo,rat);

 % Scalefactor estimation point 1 in [rad/s]
l= -lmax/20; lon=l; verskil1 = testfunpdiff(zet,r,lon,rat);

scalef = (verskil2-verskil1)/(lbo-lon); %[rad]/normalized rotation rate

scalef=-scalef;         % Calculate negative minimum, i.e. maximum
% ll=linspace(-lmax,lmax,50);
% plot(l,scalef*ll)
```

Code for the constraint function.

```
%-----------------------------------------------------------------
% Function to calculate constraints at maximum rotation rate lmax
% for use in fmincon

function [c,ceq]=testconfunpdiff(x)

% Input variables
zet = x(1); r   = x(2); rat = x(3);

nonlin = 5;     %percentage nonlinearity allowed 0.1,0.5,1,2 or 5

lmax=pi/180*500/6000;   % Typical lmax value
```

```
scalef = testscalepdiff(x);  %determine scalefactor

diff1max = testfunpdiff(zet,r,-lmax,rat);   %phasediff at -lmax
diff2max = testfunpdiff(zet,r,lmax,rat);    %phasediff at lmax


diff_sf1 = scalef*(-lmax); diff_sf2 = scalef*lmax; c1 =
abs((abs(diff_sf1)-abs(diff1max))/diff_sf1)*100-nonlin; c2 =
abs((abs(diff_sf2)-abs(diff2max))/diff_sf2)*100-nonlin;
c = max([ c1 c2 ]);     % Compute nonlinear inequalities at x.
ceq = [];               % Compute nonlinear equalities at x.
```

B.4 Plotting code

Selected Matlab scripts used for 3-D plotting are given below.

```
% This script draws the 3D analytical system response for different
% ranges of values, and exports the figures to the relevant directories.
% Uncomment parts to be used, i.e. exports
%
% exportfig.m from the Matlab central file exchange is used.

clear all, close all;
%-------------dimensionless constants-------------------------
Xs = 1;                 % Forcing amplitude ( Xs*e^jwt)
Ys = 1;                 % Forcing amplitude ( Ys*e^jwt)

zet = 0.05;             % Damping ratio
r = 0.1:0.005:2;        % Excitation frequency range
% l = -0.0075:0.00005:0.0075;   %small rotation rates
l = -0.25:0.005:0.25;   % Rotation rate range
[R,L] = meshgrid(r,l);

% For controlled primary vibration
% Ys = 0;
% axs = K*[(1-R.^2-L.^2).^2-4*(R.^2).*(zet.^2+L.^2)];
% bxs = 4*zet*R.*(1-R.^2-L.^2)*K-2*R.*L*Ys;
% cxs = 1-R.^2-L.^2;
% dxs = 2*zet*R; Xs = (axs + i*bxs)./(cxs + i*dxs);

% Call calculating function
[modX,modY,argX,argY,verskil] = simmetries3D(zet,R,L,Xs,Ys);
```

```
% Plot figures
figure(1) mesh(R,L,modX) xlabel('r','interpreter','tex')
ylabel('l','interpreter','tex') zlabel('|X|','interpreter','tex')
title(['\zeta = ',num2str(zet)],'interpreter','tex') axis tight
view(50,50)

figure(2) mesh(R,L,modY) xlabel('r','interpreter','tex')
ylabel('l','interpreter','tex') zlabel('|Y|','interpreter','tex')
title(['\zeta = ',num2str(zet)],'interpreter','tex') axis tight
view(50,50)

figure(3) mesh(R,L,argX) xlabel('r','interpreter','tex')
ylabel('l','interpreter','tex') zlabel('arg(X)
[rad]','interpreter','tex') title(['\zeta =
',num2str(zet)],'interpreter','tex') axis tight view(50,50)

figure(4) mesh(R,L,argY) xlabel('r','interpreter','tex')
ylabel('l','interpreter','tex') zlabel('arg(Y)
[rad]','interpreter','tex') title(['\zeta =
',num2str(zet)],'interpreter','tex') axis tight view(50,50)

figure(5) mesh(R,L,verskil) hold on xlabel('r','interpreter','tex')
ylabel('l','interpreter','tex') zlabel('\Delta\phi
[rad]','interpreter','tex') title(['\zeta =
',num2str(zet)],'interpreter','tex') axis tight view(50,50)

fntsz = 20; fntsztx = 20;
% % Xs=1 Ys=0
% exportfig(1,'..\wiskunde\mlabexp\Ys0modX0p1.png',...
'Format', 'png','Color','cmyk','FontMode','fixed','fontsize',fntsz);
% exportfig(2,'..\wiskunde\mlabexp\Ys0modY0p1.png',...
'Format','png','Color','cmyk','FontMode','fixed','fontsize',fntsz);
% exportfig(3,'..\wiskunde\mlabexp\Ys0argX0p1.png',...
'Format','png','Color','cmyk','FontMode','fixed','fontsize',fntsz);
% exportfig(4,'..\wiskunde\mlabexp\Ys0argY0p1.png',...
'Format', 'png','Color','cmyk','FontMode','fixed','fontsize',fntsz);
% exportfig(5,'..\wiskunde\mlabexp\Ys0dphi0p1.png',...
'Format','png','Color','cmyk','FontMode','fixed','fontsize',fntsz);
```

Appendix

C

Additional optimization results

This section contains additional tables and figures of the optimization results.

δ_{max}	$-SF$	ζ	r	f	Flag
2%	-9.7602e+002	1.0000e-003	1.0013e+000	1.0000e+000	4
	-1.6998e+002	1.0000e-003	1.7486e+000	1.0000e+002	1&4
	-1.6998e+002	1.0000e-003	1.7486e+000	1.0000e-002	1&4
	3.8820e-001	1.0000e+000	1.0000e-001	1.0000e+000	1&4

Table C.1. Optimization results: $\delta_{max} = 2\%$

δ_{max}	$-SF$	ζ	r	f	Flag
1%	-1.1896e+002	1.0000e-003	2.0000e+000	1.1209e-002	1&4
	-1.1896e+002	1.0000e-003	2.0000e+000	8.9212e+001	1
	3.8820e-001	1.0000e+000	1.0000e-001	1.0000e+000	1&4

Table C.2. Optimization results: $\delta_{max} = 1\%$

δ_{max}	$-SF$	ζ	r	f	Flag
0.5%	-9.6232e+002	1.0000e-003	1.0013e+000	1.0000e+000	4
	-8.3349e+001	1.0000e-003	2.0000e+000	6.2497e+001	1
	-8.3349e+001	1.0000e-003	2.0000e+000	1.6001e-002	1
	3.8820e-001	1.0000e+000	1.0000e-001	1.0000e+000	1&4
	4.0404e-001	1.0169e-003	1.0000e-001	1.0000e+000	5

Table C.3. Optimization results: $\delta_{max} = 0.5\%$

δ_{max}	$-SF$	ζ	r	f	Flag
0.1%	-9.5772e+002	1.0000e-003	1.0013e+000	1.0000e+000	4
	-3.6447e+001	1.0000e-003	2.0000e+000	2.7298e+001	1&4
	-3.6447e+001	1.0000e-003	2.0000e+000	3.6632e-002	1&4
	3.8820e-001	1.0000e+000	1.0000e-001	1.0000e+000	1&5
	4.0404e-001	1.0209e-003	1.0000e-001	1.0000e+000	5

Table C.4. Optimization results: $\delta_{max} = 0.1\%$

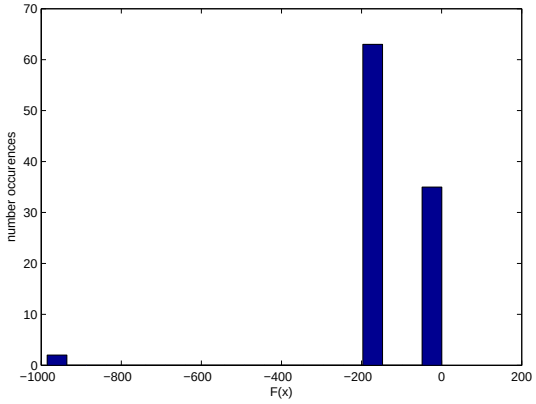

Figure C.1. Histogram of optimal SF occurrences ($\delta_{max} = 2\%$)

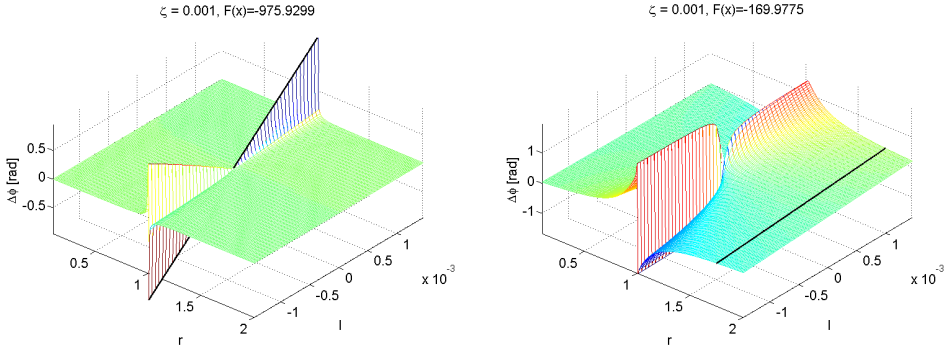

(a) (b)

Figure C.2. Local minima for $F(x) = -SF$, with $\delta_{max} = 2\%$

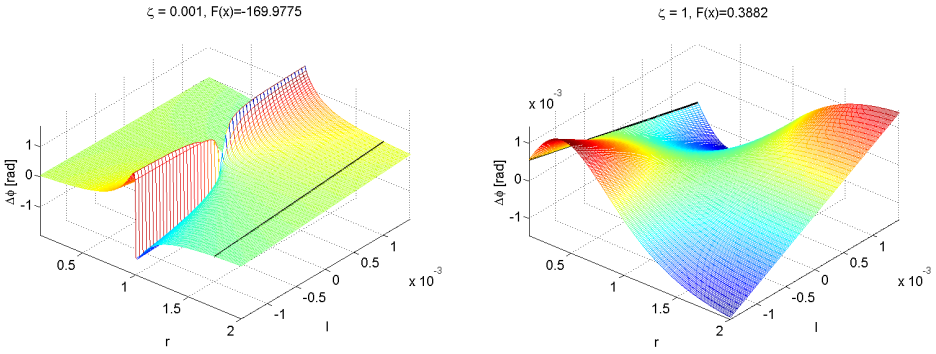

(a) (b)

Figure C.3. Local minima for $F(x) = -SF$, with $\delta_{max} = 2\%$

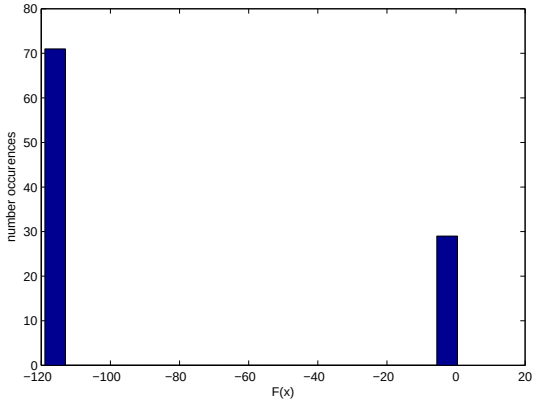

Figure C.4. Histogram of optimal SF occurrences ($\delta_{max} = 1\%$)

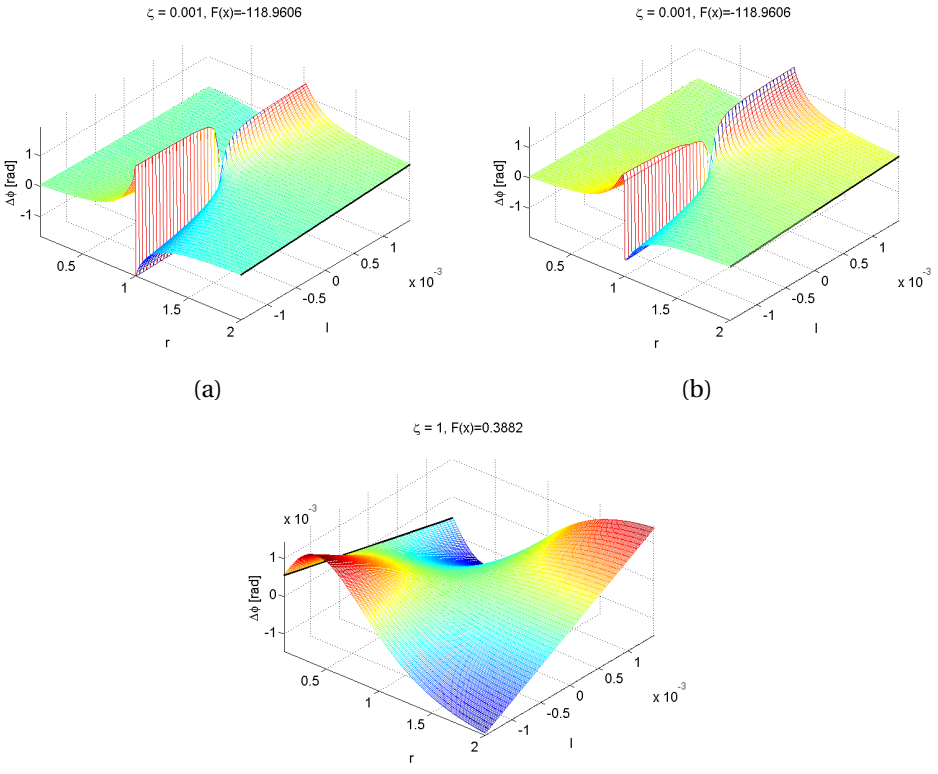

Figure C.5. Local minima for $F(x) = -SF$, with $\delta_{max} = 1\%$

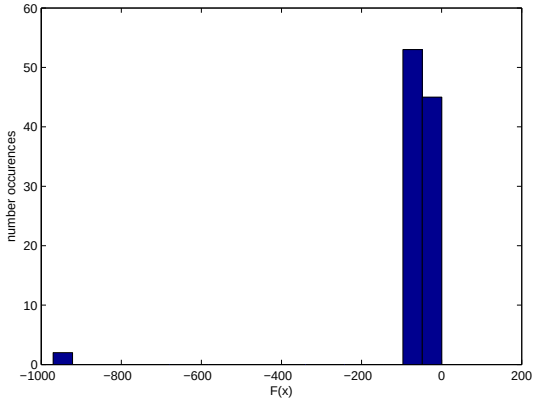

Figure C.6. Histogram of optimal SF occurrences ($\delta_{max} = 0.5\%$)

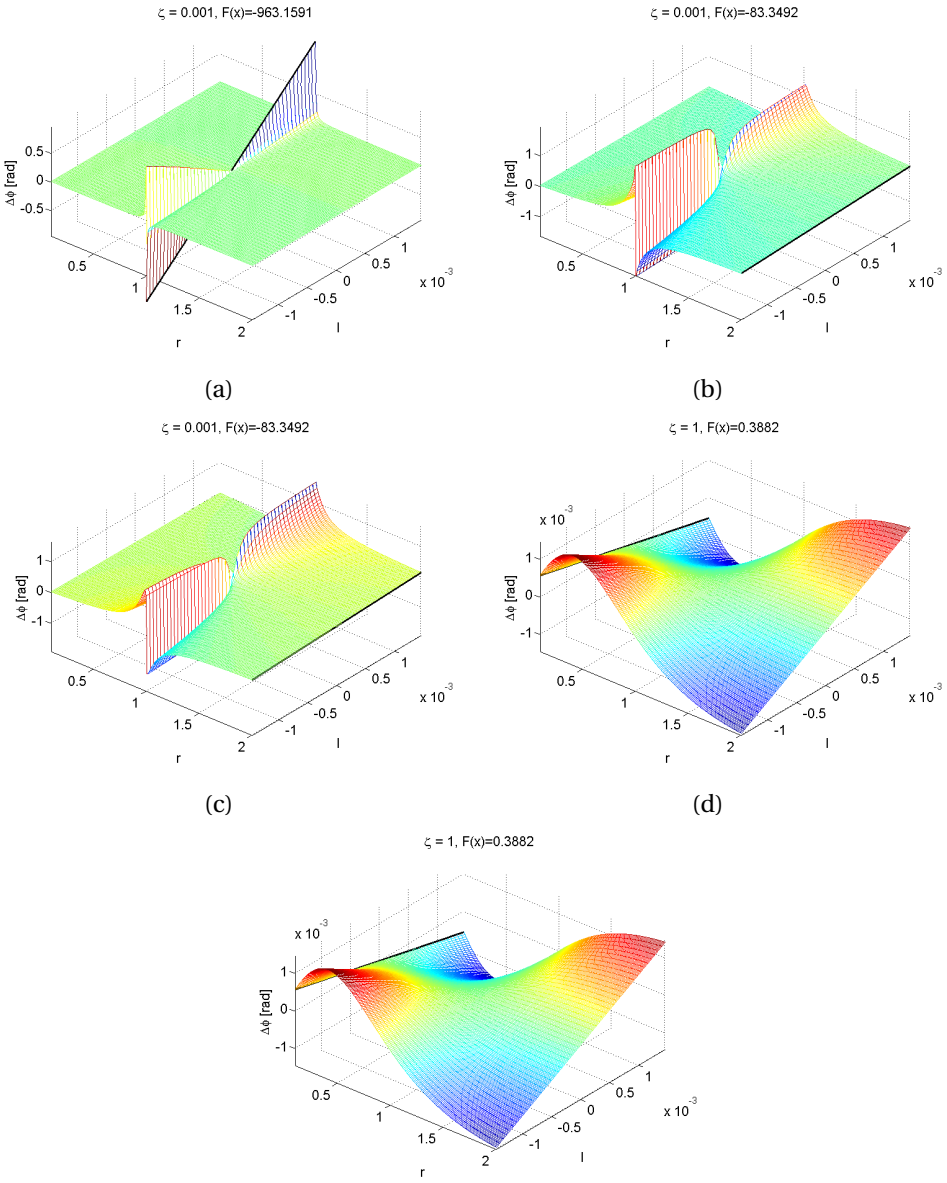

(a) (b) (c) (d) (e)

Figure C.7. Local minima for $F(x) = -SF$, with $\delta_{max} = 0.5\%$

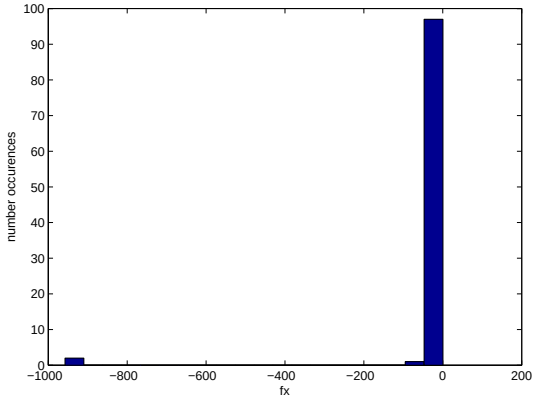

Figure C.8. Histogram of optimal SF occurrences ($\delta_{max} = 0.1\%$)

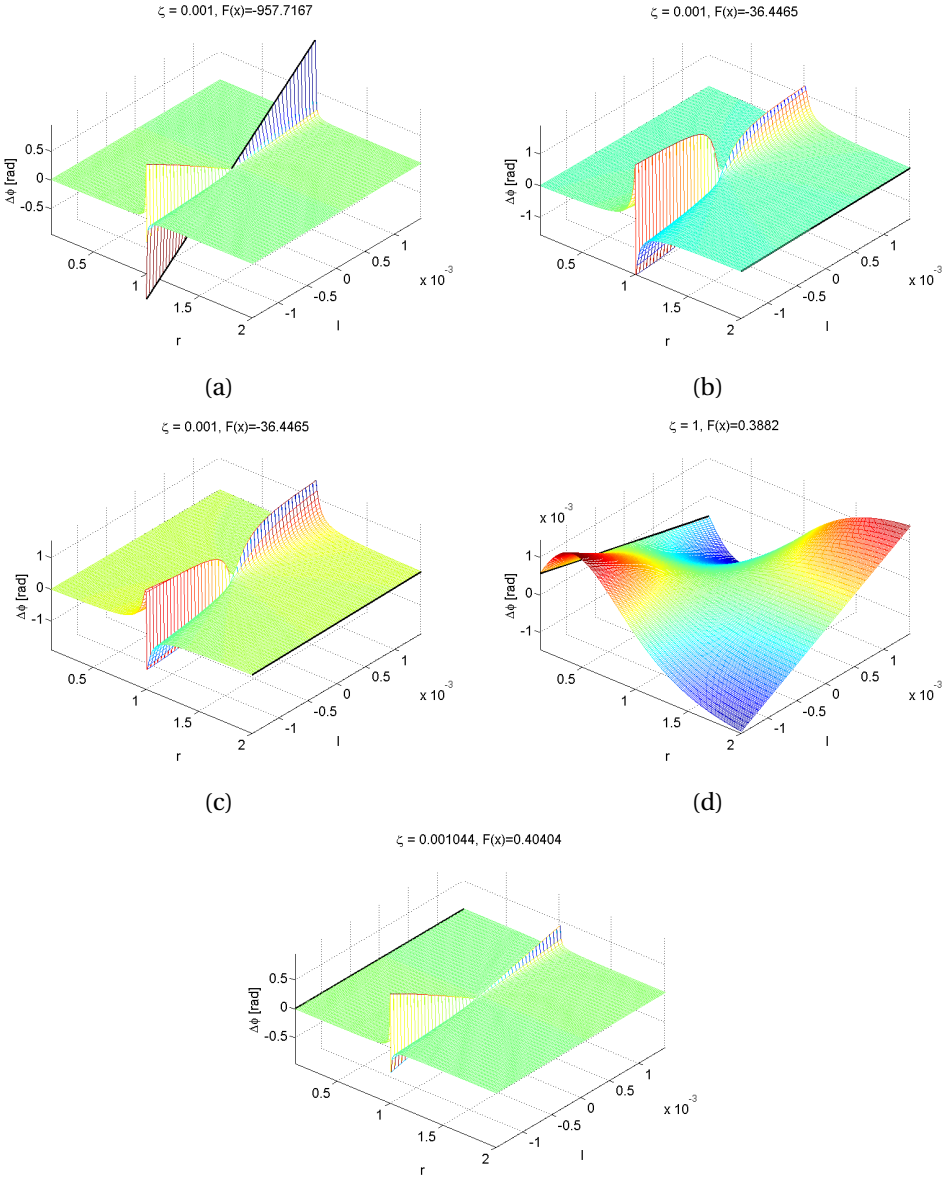

Figure C.9. Local minima for $F(x) = -SF$, with $\delta_{max} = 0.1\%$